理學博士 學位論文

Plasmonic Effects on Dye-Sensitized Solar Cells

염료감응 태양전지에 미치는 플라즈모닉 효과

2016 年 8 月

서울大學校 大學院

化學部

金 賢 英

Abstract

Dye-sensitized solar cells (DSSCs) have received much attention on account of their low cost-to-performance ratio, easy scale-up, light weight, ability to work at wide angles, low intensities of incident light, and modifiable aesthetic features such as color and transparency. However, the energy conversion efficiency of DSSCs needs to be further improved to become an economically profitable alternative. To improve energy conversion efficiency of the DSSCs, many efforts were performed in various aspects, such as increasing light harvesting by using panchromatic dye or enlarging amount of dye adsorbed on TiO_2 nanoparticles (NPs), and reducing charge transfer resistance of I_3^- reduction by using alternative counter electrode. In this thesis, as a part of the ongoing study, two types of approaches have been made to improve energy conversion efficiency of the DSSCs; 1) developing new photoanode based on silver (Ag) NPs which has localized surface plasmon resonances (LSPRs) and 2) developing alternative counter electrode based on graphene with gold (Au) NPs which has high catalytic activity and low charge-transfer resistance.

In the first part, we fabricated plasmonic DSSCs based on composite films consisting of TiO_2 NPs and Ag NPs. The energy conversion efficiency of the plasmonic DSSCs was affected by the degree of the spectral overlap between the extinction bands of Ag NPs and two visible absorption bands of N719 dye, centered at 393 and 533 nm. Also, it was affected by the weight percent of Ag NPs to TiO_2 NPs. The energy conversion efficiency was enhanced as increasing to a certain weight percent of Ag NPs but then decreased when the weight percent was further increased, which was due to aggregation of metal NPs. As a result of aggregation of metal NPs, the LSPRs were red-shifted and mismatched to the two visible absorption bands of N719 dye. Accordingly, in this case, the energy conversion efficiency was decreased. Therefore, the aggregation of metal NPs should be avoided in the fabrication of the composite films of TiO_2 NPs and metal NPs to achieve a high energy conversion efficiency of surface plasmon-enhanced DSSCs.

Next, to prevent aggregation of Ag NPs, a quasi-monolayer film based on Ag NPs was developed. Three kinds of Ag NPs with different size and extinction maximum wavelength were prepared and immobilized on a photoactive layer coated with

poly(4-vinyl pyridine)(P4VP). As a result, developed quasi-monolayer film based on Ag NPs showed panchromatic behavior which absorbed in all of the visible range. By constructing a panchromatic quasi-monolayer between the photoactive and scattering layers, the efficiency of the plasmonic DSSCs was enhanced from 8.9 ± 0.3% to 11.0 ± 0.4%, mainly by increase the photocurrent density. Absorption of dye molecules might be enhanced at around the surface of Ag NPs by the LSPRs, because the quasi-monolayer of Ag NPs scattered light strongly. Owing to the enhanced absorption by LSPRs effect, we could greatly reduce the thickness of the photoactive layer, about one-half the optimum length.

As a second approach to achieve enhanced energy conversion efficiency, we fabricated a nanostructure-based graphene flake counter electrode by immobilization of gold nanoparticles (NPs) on fluorine-doped tin oxide (FTO) glass and the deposition of a thin layer of graphene flakes. The graphene flakes, fabricated using a thermal plasma jet system, were very thin and pure and had good crystallinity. Although their average size was larger than 100 nm, they were well dispersed in some solvents by sonication. Relatively large size and good crystallinity lead good conductivity, and their good dispersibility allow to fabricate

uniform films. The efficiency of the DSSC with a graphene flake/Au NP/FTO counter electrode was as much as 9.71%, which is higher than that with a conventional Pt/FTO (9.02%) or graphene flake/FTO (8.91%) counter electrode. By measuring the power conversion and incident photo-conversion efficiency, we discovered that the high efficiency was due to the LSPRs effect of the Au NPs included between the graphene flakes and FTO. We also proved that the catalytic activity of a graphene flake/Au NP/FTO counter electrode was improved and the charge-transfer resistance at the electrode/electrolyte interface was decreased using cyclic voltammograms and electrochemical impedance spectroscopy.

Key words: Dye-sensitized solar cells (DSSCs), Localized surface plasmon resonances (LSPRs), Silver nanoparticles (Ag NPs), Gold nanoparticles (Au NPs), Graphene counter electrode.

Student Number: 2013-30091

Contents

List of Tables

List of Figures

Chapter 1

Introduction

1. 1. Dye-sensitized solar cells

Dye sensitized solar cells (DSSCs) is consist of an inorganic semiconducting photoanode adsorbed with dye and a platinized counter electrode as shown Figure 1. 1.[1] In 1991, Oregan and Grätzel built the first DSSCs which showed 7.1% energy conversion efficiency.[2] DSSCs have been the subject of intense study due to several advantages, such as low cost of fabrication, modifiable aesthetic features such as color and transparency, functionality at wide angles and low intensities of incident light, and mechanical robustness.[1-11]

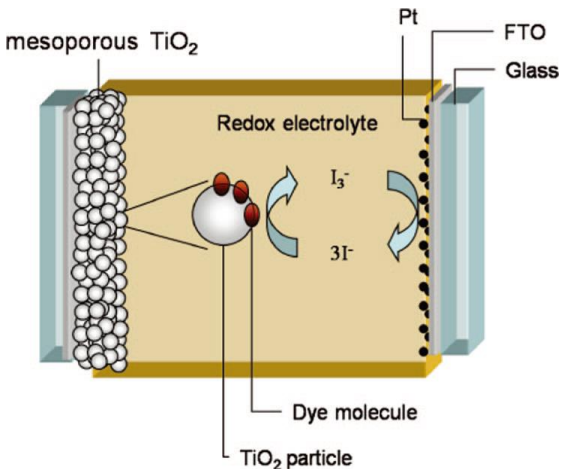

Figure 1. 1. Schematic image of a dye-sensitized solar cells.[1]

1. 1. 1. Components of DSSCs

DSSCs consist of four components: (1) a semiconductor, (2) a sensitizer, (3) an electrolyte, and (4) a counter electrode such as platine.[12-16]

1. 1. 1. 1. Semiconductor

The semiconductor as a photoanode in DSSCs provides multiple functions as supporter of sensitizer to load, and transporter of excited electrons from sensitizer to external circuit. Therefore, a large surface area and fast charge transport rate are required to ensure high dye loading and electron collection efficiency.[9] TiO_2 NPs are referred to the most adaptable materials for electron acceptor in DSSCs due to their outstanding chemical properties. For example, it is stable, non-toxic, absorbs ultra-violet light, and has a large surface area.[16,17] Generally, TiO_2 NPs have several crystal phase, such as rutile, anatase, and brookite. Anatase is preferred in DSSCs, because of their large bandgap (3.2 vs 3.0 eV for rutile) and high conduction band edge, which leads to a higher Fermi level and V_{oc} in DSSCs.[16,17]

1. 1. 1. 2. Dye

In DSSCs, the dye serves a vital role as sensitizer, which absorbs light and transfers electrons to the conduction band of the semiconductor. The dye molecules commonly used in DSSCs are polypyridyl-type ruthenium (Ru) complexes such as N719 and N3.[3,9,18,19] In the case of Ru based sensitizer, it is consist of a central metal ion with ancillary ligands, such as bipyridines and terpyridines, and anchoring groups (-COOH, -H_2PO_3, etc.).[1] Photophysical and electrochemical properties of the dye can be controlled by tuning ancillary ligands to improve the photovoltaic performance. Anchoring group, which is chemically bonded to the surface of semiconductor, is responsible for charge injection and dye orientation.[1,14] It is well-kwon that the Ru complexes absorb the visible light due to a metal to ligand charge transfer (MLCT) process. Furthermore, it has a proper excited and ground state energy levels, relatively long excited-state lifetime, and high chemical stability.[14]

1. 1. 1. 3. Electrolyte

The electrolyte is responsible for regeneration of the oxidized dye, which injected electrons into the conduction band of the semiconductor.[13] The iodide/triiodide electrolyte system is commonly used in DSSCs, because of its important features, such as easy preparation, high conductivity, good permeability, and fast oxidation of I^- at the photoanode/electrolyte interface.[20-22] Moreover, incorporation of 4-tertbutyl pyridine and guanidine in the iodide/triiodide electrolyte system increases the open-circuit voltage and fill factor by decreasing recombination rate.[23-25] Due to the small atomic radius of the Li^+ of LiI, it can penetrate deeply into the TiO_2 NPs. As a results, additive LiI can enhance electron transport ability and increase photocurrent density.[26]

1. 1. 1. 4. Counter electrode

The counter electrode in DSSCs has a multiple role as a catalyst to regenerate the electrolyte and electron collector from the external circuit.[27] The counter electrode should have advantages of high catalytic activity and electrical conductivity.[28] Generally, platinum coated FTO glass substrate is used to as a conventional counter electrode in DSSCs. Pt counter electrode exhibits high catalytic activity for tri-iodide reduction and good electric conductivity, and has a high resistance against iodine corrosion.[29]

1. 1. 2. Operational principle of DSSCs

DSSCs directly convert solar radiation energy into electric energy. The operational principle of DSSCs is shown in Figure 1. 2.[14]

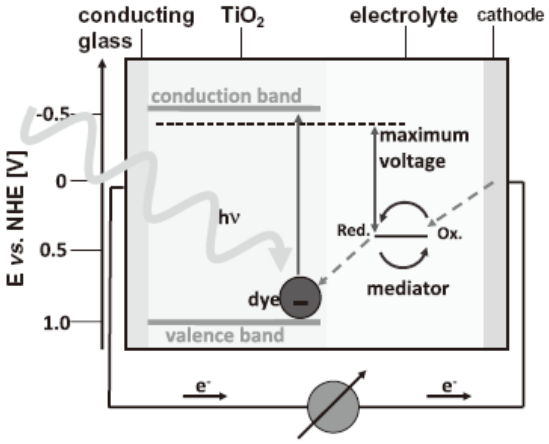

Figure 1. 2. Operating scheme and energy level diagram of conventional DSSCs.[14]

$$E/TiO_2\text{–}Dye \xrightarrow{h\nu} E/TiO_2\text{–}Dye^* \quad \text{Eq.1}$$

$$E/TiO_2\text{–}Dye^* \longrightarrow E/TiO_2(e^-)\text{–}Dye^+ \quad \text{Eq.2}$$

$$E/TiO_2(e^-)\text{–}Dye^+ \longrightarrow E^-/TiO_2\text{–}Dye^+ \quad \text{Eq.3}$$

$$E/TiO_2(e^-)\text{–}Dye^+ + 2I^- \longrightarrow E/TiO_2(e^-)\text{–}Dye + I_2^- \quad \text{Eq.4}$$

$$2I_2^- \longrightarrow I_3^- + I^- \quad \text{Eq.5}$$

(1) The dye, which is typically a metal organic Ru complex, is excited from ground state to the excited state by absorption of a photon. (Eq.1)

(2) The dye injects an electron into the conduction band of the semiconductor, leaving itself in the oxidized state. (Eq.2)

(3) The injected electrons flow through the external load to transparent conductive substrate by diffusion. (Eq.3)

(4) The electrolyte donates electrons to the oxidized dye and regenerates to the initial state. (Eq.4)

(5) The oxidized species of the electrolyte, such as triiodide in iodide-triiodide complex, reduce to iodide at the catalytic electrode. (Eq.5)

1. 1. 3. Terminologies of DSSCs

1. 1. 3. 1. Short-circuit current

Short-circuit current is defined as the current when the voltage across the solar cell is zero. It is obtained from the cell when the current is short-circuited or when the load resistance is zero.[16]

$$J_{sc} = \frac{I_{sc}}{A} \ (mA/cm^2) \qquad Eq.6$$

where, A is the effective area of the solar cell.

1. 1. 3. 2. Open-circuit Voltage

Open-circuit voltage is determined by the energy difference of electrical potential between two terminals of a device when a load with infinite resistance is attached to its terminals.[30,31]

$$V_{oc} = \frac{E_{CB}}{q} + \frac{kT}{q} \ln \frac{n}{N_{CB}} - \frac{E_{redox}}{q} \quad (volts) \qquad Eq.7$$

where, n is the number of electron in TiO_2 conduction band and N_{CB} is the effective density of states. The first two terms define the quasi-fermi level of TiO_2 and E_{redox}, which is the Nernst potential of the redox mediator.

1. 1. 3. 3. Series resistance

The series resistance (R_s) may be result from the flowing of electrons through mesoporous semiconductor and the diffusion of the electrolyte. It could be affected by the contact resistance at the interface between the semiconductor and the transparent conductive substrate.[32] When series resistance is high, it reduces the fill factor, and the short-circuit current, while it does not affect the solar cell at open-circuit voltage.[33,34]

1. 1. 3. 4. Shunt resistance

The shunt resistance (R_{sh}) is typically due to the manufacturing defects such as current leakage, which occur in the p-n junction or at the edge of the cell, or the impurities in the cell. The shunt resistance allows power of DSSCs to loss by providing an alternate current path for light-generated current. Low shunt resistance reduces fill factor and open-circuit voltage affecting the maximum power output.[30]

1. 1. 3. 5. Fill factor

The fill factor (FF) is defined as the ratio of maximum obtainable power to product of the open-circuit voltage and short-circuit current.[35] The fill factor can assume values between 0 and less than 1, and represents the squareness of $J-V$ curve as shown Figure 1. 3.

$$FF = \frac{J_m \times V_m}{J_{sc} \times V_{oc}} \qquad \text{Eq.8}$$

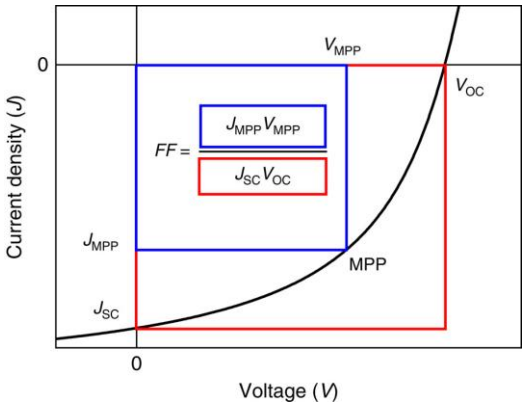

Figure 1. 3. The ration of maximum power to product of the V_{oc} and J_{sc} in $J-V$ curve.[35]

1. 1. 3. 6. Efficiency

The photo-conversion efficiency (energy conversion efficiency, η) is determined by the short-circuit current (J_{sc}), the open-circuit potential (V_{oc}), the fill factor (ff) of the device and the intensity of the incident light (P_{in}).[36]

$$\eta = \frac{J_{sc} \times V_{oc} \times ff}{P_{in}} \qquad \text{Eq.9}$$

1. 1. 3. 7. Quantum efficiency

Quantum efficiency (QE) or external quantum efficiency (EQE) can be expressed by incident photon-to-current efficiency (IPCE). It means that how the DSSCs efficiently produce photo-generated charge at a given frequency. It is defined as the photocurrent density produced in the external circuit under illumination condition, divided by the photon flux of excitation wavelength.[14]

$$\begin{aligned} IPCE(\lambda) &= \frac{\text{Photocurrent density}}{\text{Wavelength x Photon flux}} \\ &= LHE(\lambda) \times \phi_{inj} \times \eta_{coll} \end{aligned} \qquad \text{Eq.10}$$

where, LHE(λ) is the light-harvesting efficiency at excitation wavelength, ϕ_{inj} is the quantum yield for electron injection from the excited state of dye to conduction band of TiO_2, and η_{coll} is the efficiency for the collection of electrons.

1. 2. Plasmonic DSSCs

1. 2. 1. Surface plasmon resonances

Surface plasmon resonances (SPRs) are coherent delocalized oscillations of conduction electrons excited by electromagnetic radiation. SPRs are generally consist of two types: (1) propagating surface plasmons (PSPs), which generate at the metal film and (2) localized surface plasmons (LSPs), which generate at the metal NPs.[37-40]

In the case of PSPs, surface electromagnetic field propagates along the dielectric interface of metal in the x-/y-directions, but decays exponentially in the z-direction (Figure 1. 4a).[38-42] For the case of LSPs, metallic NPs interact with light when they are much smaller than the incident wavelength, leading to a polarization at the surface of metal NPs. Consequently, induced polarization make oscillate electrons locally at the surface of metal NPs, therefore, light absorption can be enhanced strongly, as depicted in Figure 1. 4b.[43-45]

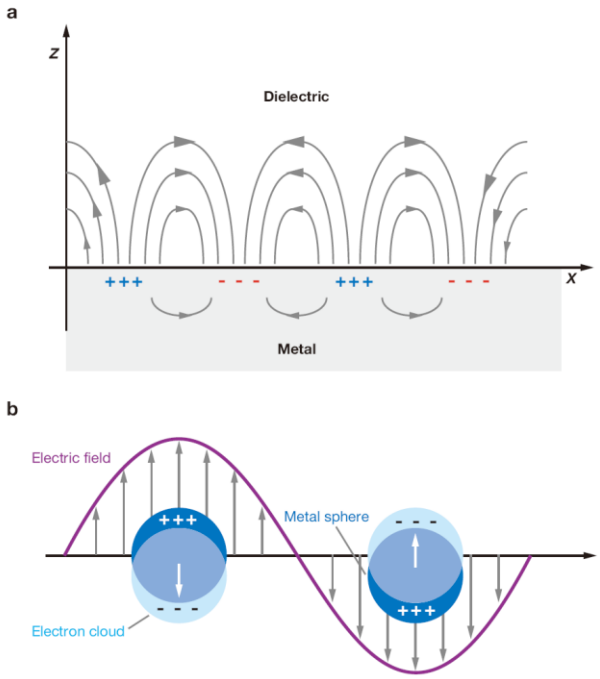

Figure 1. 4. Schematic diagrams of (a) propagating surface plasmons (PSPs) and (b) localized surface plasmons (LSPs).[42]

1. 2. 2. Localized surface plasmon resonances

Localized surface plasmon resonances (LSPRs) are an optical phenomenon when the electrons in conduction band of metal NPs are coupled with the electromagnetic field. The LSPRs frequency is basically controlled through the free electron density (N) of the material modulated by its high frequency dielectric constant, although it could be tuned by the size, geometry, composition, local medium, and particle−particle separation distance of metal NPs.[46,47] The dipole polarizability (P) of spherical NPs is expressed as:[48]

$$P = 4\pi a^3 \frac{\varepsilon - \varepsilon_m}{\varepsilon + 2\varepsilon_m} \qquad \text{Eq.11}$$

where, a is the diameter of the NPs and ε and ε_m are the dielectric constants of the surrounding dielectric medium and of the metal NPs itself, respectively.

1. 2. 3. Metal nanoparticles

Optical properties of metal NPs are affected by the shape and the size due to the changes in surface polarization. To tailor LSPRs absorption from visible to infrared regions, metal NPs can be synthesized as various shapes such as spheres, triangles, cubes, prisms, bipyramids, octahedrons, nanorods, nanoshells, and nanostars as well as structured array films.[49]

In general, increment of edges and/or sharpness of a metal NPs induce the charge separation character which results a bathochromic shift of extinction spectra. On the other hand, intensity of LSPRs is depending on the symmetry of metal NPs.[50] The number of resonance absorption peak(s) is determined by the number of mode(s) in which a given metal NPs can be polarized.[47,51]

Figure 1. 5 shows the extinction, absorption, and scattering spectra of Ag NPs depending on different shapes. Non-spherical NPs tend to exhibit multiple and red-shifted peaks compared to spherical particles. The extinction spectra of 1D nanobars with different aspect ratios are shown in Figure 1. 5f. By controlling the aspect ratio of the nanobar, the resonance peak positions of such 1D nanoparticles can be tuned from the

visible into the near infrared.

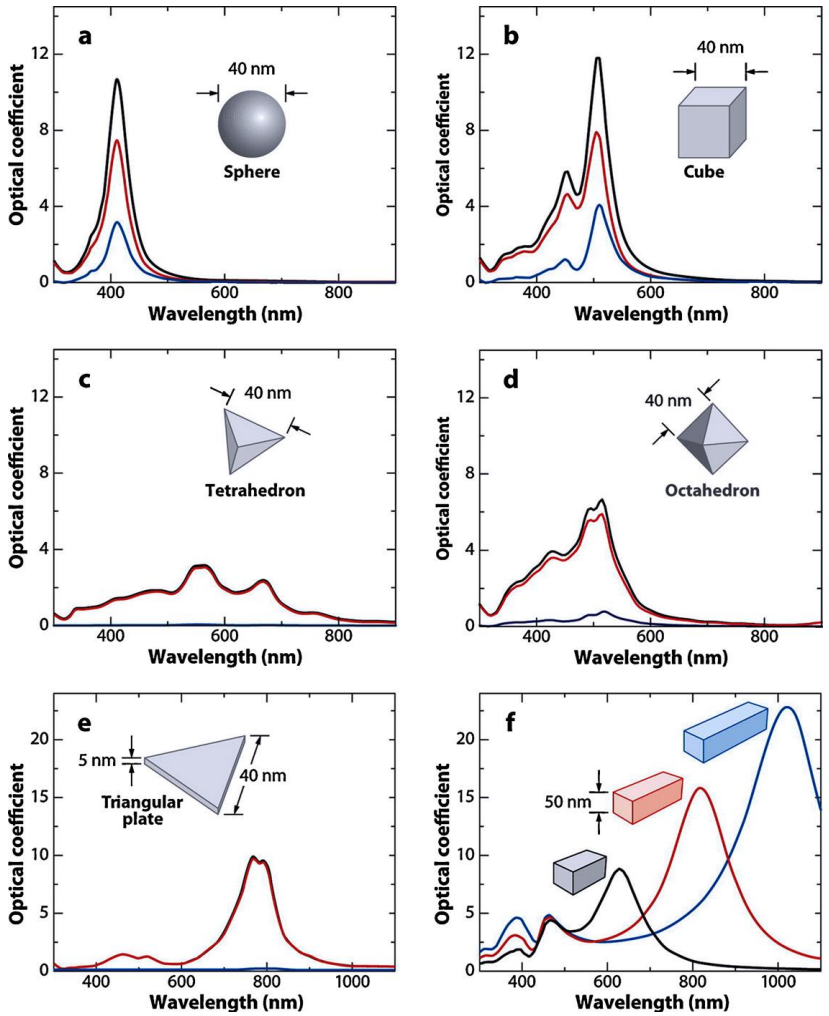

Figure 1. 5. Extinction (black), absorption (red), and scattering (blue) spectra of Ag NPs depending on different shapes: (a) a sphere (b) a cube, (c) a tetrahedron, (d) an octahedron, and (e) a triangular plate. (f) Extinction spectra of rectangular bars with aspect ratios of 2 (black), 3 (red), and 4 (blue).[50]

1. 2. 4. Fabrication of metal NPs for LSPRs

Fabrication of metal NPs is widely categorized by two types; top-down and bottom-up methods.[52-54] Top-down method produce the nanostructures by using macroscopic initial structures followed by external controlled in the process. In top-down method, it is usually classified into two approaches including physical and chemical approaches. The physical top-down approaches use photons (optical lithography),[55-57] electrons (electron beam lithography),[53,56] and ions (ion beam lithography)[58] to deconstruct larger materials while the chemical top-down approaches employ chemical reactions to construct nanomaterials.[59-62]

In contrast, bottom-up method construct nanostructures from atomic or molecular precursors by reacting, growing in size, and self-assembly. [53] It include deposition techniques (atomic layer or chemical vapor deposition),[63-79] molecular self-assembly processes,[70,71] and colloidal-based technique.[50,72-75]

In case of colloidal-based technique, it produces metal NPs through rapid nucleation followed by controlled growth with coordinating ligands or surfactants.

1. 2. 5. Solution-phase synthesis for metal NPs

Generally, solution-phase synthesis of bottom-up method have a two-step process: nucleation and growth.[49] First, formation of metal atom is rapidly produced by reduction or decomposition of a precursor to form seed with a size range of 1-5 nm. These metal atoms lead to assemble small clusters and further grow relatively stable crystal nuclei. The second step is the growth of the metal NPs. Metal nuclei grows slowly to nanostructured-materials with addition of more metal ions and different reductants.[76]

One of the most commonly used procedures to make Au NPs is the citrate reduction of $HAuCl_4$ in an aqueous solution.[77] Choosing an appropriate stabilizer for the reduction of metal salts in a solution is important to control the growth and reduce the aggregation of the NPs in synthetic procedure.[78] When thiol-stabilizing agents are used, the reduction of $AuCl_4^-$ in aqueous solution should be performed with borohydride or similar reducing agent, because the complexes prepared from $AuCl_4^-$and thiols are too stable to reduce by citrate or other weak reducing agents.[79]

1. 2. 6. Plasmonic effect in DSSCs

Light harvesting or carrier collection is important factor to increase the efficiency of the DSSCs. On the basis of the LSPRs effect, plasmonic nanostructures have been applied as a promising alternative to increase the optical absorption and/or photocurrent in DSSCs.[80-112]

1. 2. 6. 1. Plasmonic light trapping in DSSCs

There are three kinds of plasmonic light trapping structures to enhance the photovoltaics efficiencies.[105-108]

Firstly, metal NPs act as subwavelength scattering centers to couple and trap freely propagating plane waves. Thus, induced multiple scattered light will effectively increase the optical pathway, as shown in Figure 1. 6a. Secondly, relatively small metal NPs (5-20 nm) embedded in photoactive layer are used as subwavelength antennas. Therefore, as shown in figure 1. 6b, the local-field absorption can be enhanced by LSPRs excitation. Third, periodic corrugated nanostructures on the surface of the absorption layer can sustain propagating SPP modes. Excitation of SPPs ensures the coupling of incident light to photonic modes propagating in the semiconductor layer (Figure 1. 6c).

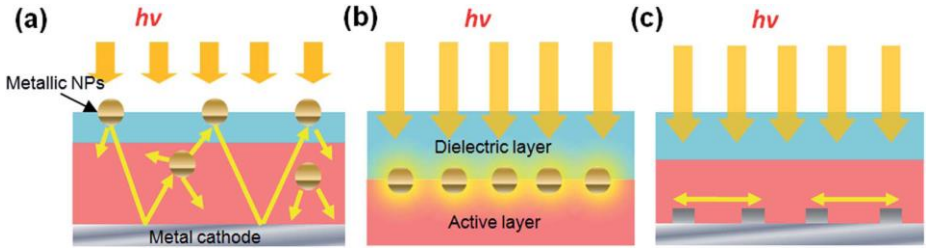

Figure 1. 6. Schematic images of plasmonic-enhanced photovoltaics. (a) Scattering from metal NPs inside the photoactive layer (b) LSPRs induced by small diameter (5–20 nm) of metal NPs embedded in the semiconductor. (c) Excitation of SPPs at the NPs/photoactive layer interfaces.[106]

1. 2. 6. 2. Trend of plasmonic DSSCs

Several attempts have performed to apply noble metal NPs to increase the efficiency in DSSCs. By LSPRs effect of metal NPs, it is possible to reduce the thickness of photoactive layer without hindering absorption.[108]

Schaadt *et al*. developed the silicon (Si) solar cells, which is enhanced about 80% for absorption by Au NP depositions.[109] Derkaces *et al*. reported an increase in efficiency via the excitation of LSPRs on amorphous Si solar cells by deposition of Au NPs.[110]

Typically, metal NPs have been cooperated with TiO_2 NPs paste for photoactive layer of DSSCs. However, when the bare metal NPs expose to the electrolyte, it leads to serious problems such as recombination or back reaction of the charge carriers as well as thermal and chemical decomposition. Therefore, plasmonic metal NPs should be protected by insulating shell.[89,92,100,101,111]

For instance, Choi *et al*. applied core shell NPs such as $Au@TiO_2$ and $Au@SiO_2$ into the DSSCs to avoid dissolution of the metal. Moreover, they have identified the mechanism with which the performance of DSSCs is influenced by the

neighboring metal nanoparticles by employing SiO_2– and TiO_2–capped Au NPs.[100]

Jeong *et al*. reported 25% of the photocurrent improvement due to the increased dye's effective absorption cross section and increased surface area. Deployment of Ag NPs as photoactive layer in DSSCs led to photo conversion efficiency with overall of 8.9 %.[89]

Dang *et al*. reported a novel approach to broadband and panchromatic solar energy conversion using multiple–core–shell structured TiO_2–Au–TiO_2 (TAuT) NPs plasmonic nanoparticles. These nanoparticles feature tunable LSPRs frequencies and can be used photoactive materials as the broadband light harvesting elements. They demonstrated that performance of panchromatic DSSCs was significantly enhanced from 8.3% to 10.8%, by simply blending the plasmonic nanoparticles with available photoactive materials.[101]

Furthermore, Lim *et al*. reported the first successful application of a nitrogen (N)–doped–TiO_2 with Ag nanoparticles as a photoactive layer for highly efficient DSSCs. The N–TiO_2–Ag nanocomposites with different Ag contents were prepared using a simple chemical reduction method and characterized using various suitable techniques. The improved photovoltaic

performance of DSSCs assembled with the N−TiO_2–Ag− nanocomposite was due to the reduced band gap energy and retarded charge recombination that resulted from the introduction of plasmonic Ag nanoparticles on the surface of N−TiO_2.[112]

Recently, Zarick *et al.* reported 34% improvement in the energy conversion efficiency of DSSCs with gold nanocubes of controlled shape.[98] They have also found that there is a monotonic decrease in efficiency at very high nanocube concentration. Photocurrent behavior and incident photon to current efficiency spectra revealed that device performance is controlled by the particle density of Au@SiO_2 nanocubes and monotonically decrease at very high nanocube concentration.

1. 3. Graphene

Graphene is a planar monolayer sheet of sp^2–bonded carbon atoms densely packed into a honeycomb crystal lattice. The name ‘graphene’ comes from ‘graphite’ and ‘–ene’. It can be wrapped up into 0D fullerenes, rolled into 1D nanotubes or stacked into 3D graphite.[113–115]

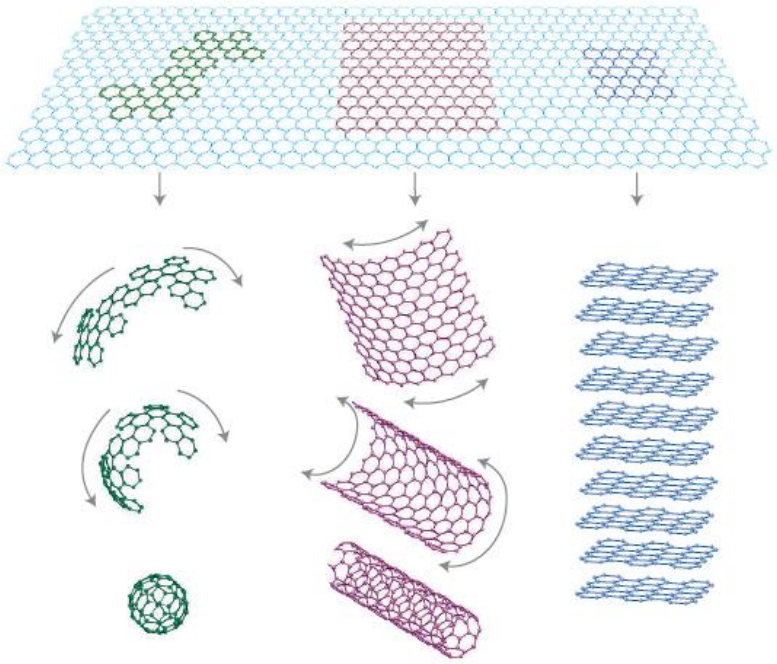

Figure 1. 7. Schematic images of all graphitic forms. Graphene is a 2D building material and it can be wrapped up into 0D buckyballs, rolled into 1D nanotubes or stacked into 3D graphite.[113]

1. 3. 1. Synthesis of graphene

Graphene can be synthesized in various ways and on different substrates. There are four primary synthesis methods for pristine graphene.

1. 3. 1. 1. Micromechanical exfoliation

Graphene was firstly separated by mechanical exfoliation from bulk graphite.[114] Through repeating stick–process by using common adhesive tape, graphene was peeled from the bulk graphite layer by layer.[116] It was required to exfoliate graphite about the order of magnitude of the 300 $nN/\mu m^2$, because an inter–layer van der Waals interaction energy is extremely weak force about 2 eV/nm^2.[117]

Typically, mechanical routes to exfoliate graphite can be categorized by two types as shown Figure 1. 8. One is the normal force to overcome the van der Waals attraction when peeling two graphite layers apart, such as micromechanical cleavage by Scotch tape. Another is exerting lateral force to promote the relative motion between two graphite layers through graphite self–lubricating ability in the lateral direction.

These techniques are neither scalable nor capable of mass production, even though the graphene obtained could be useful for basis studies.

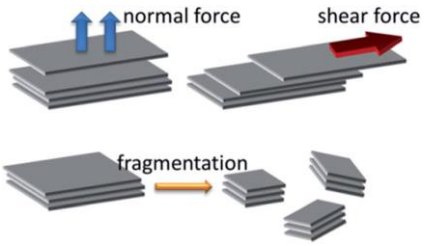

Figure 1. 8. Two types of mechanical routes for exfoliating graphite to synthesize graphene flakes.[116]

1. 3. 1. 2. Epitaxial graphene

Epitaxial graphene can be produced on silicon carbide (SiC) wafer substrates through thermal decomposition at ~1300°C under vacuum condition as shown Figure 1. 9.[118] In 1965, Badami demonstrated the phenomenon of graphitization on the surface of a SiC single crystal. They found that the c−axis of graphite is along the c−axis of the hexagonal SiC crystal.[119] In 2004, Berger *et al.* showed the presence of Shubnikov-de Haas oscillations, which formed the pioneering work revealing a new quantum Hall system in epitaxial graphene on SiC.[120] Emtsev *et al.* revealed that homogeneous graphene growth was possible by annealing in an argon atmosphere, which suppressed the decomposition rate and improved the quality of the graphene.[121]

Epitaxial graphene has several merits, especially, it can be patterned using standard lithography methods, a useful property for nanoelectronics. Moreover, the physical properties of graphene vary significantly from growing epitaxially to exfoliating mechanically, due to the influence of interfacial effects in epitaxial graphene. However, it is hard to control the thickness of graphene in the routine production and unusual

rotational graphene stacking is observed in multilayer graphene, because of the different epitaxial growth patterns. Furthermore, it need to investigate the relationship between the structure and electric properties of the interface layer.

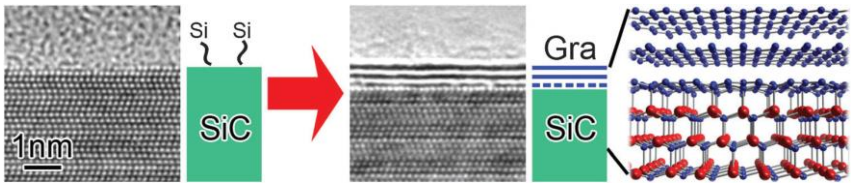

Figure 1. 9. Schematic images of graphene growth by thermal decomposition of SiC, together with the structural model of bilayer graphene on SiC.[118]

1. 3. 1. 3. Chemical vapor deposition

Chemical vapor deposition (CVD) is one of the most promising, inexpensive and accessible approach to synthesize high quality graphene.[122] Graphene can be grown by CVD method from carbon sources on catalytic metal surfaces. If carbon sources flow into the reactor and pass through the hot zone, hydrocarbon precursors can be decomposed to carbon radicals on the metal substrate surface and then, form single-layer and few-layers graphene.

Due to the metal substrate not only works as a catalyst, but also determines the graphene deposition mechanism, choosing proper metal substrates is important step. Generally, Ni or Cu films are used as the substrate with methane as the precursor gas.[123]

One of the main advantages of the CVD method is high compatibility with the current complementary metal-oxide-semiconductor (CMOS) technology. However, it is difficult to control the film thickness and need expensive substrate to graphene growth.

1. 3. 1. 4. Chemical method

Several methods were explored to extract graphene monolayers in solution phase by means of chemical routes. Horiuchi *et al.* produced carbon nano films (CNF) from natural graphite.[124] Stankovich *et al.* produced a number of functionalized graphite oxides, which were prepared by treatment of graphite oxide (GO) with organic isocyanates.[125] As another chemical method, Li *et al.* reported that the exfoliation-reintercalation-expansion of graphite produced high quality single-layer graphene sheets stably suspended in organic solvents.[126]

Chemical method to fabricate graphene is low-cost process and possible to produce scalable and capable of mass production. It enables chemical modification/functionalization, purification, and transferring graphene from the solution phase to adaptable substrate by spin-, spray-, drop- or dipcasting process. The Langmuir-Blodgett technique[127] is one of the useful transferring method, implemented for low-cost ITO substitution in flexible transparent conductive photostable thin films.

1. 3. 2. Properties of graphene

Graphene is composed of sp^2-bonded carbon atoms in a 2D-honeycomb lattice.[128] As shown in Figure 1. 10a, two carbon atoms are contained in an unit cell and the graphene lattice is formed by two triangular sub-lattices, which is A and B. Each atom has one s-orbital and two in-plane p-orbitals taking care of the mechanical stability of the carbon sheet. The valence band is formed by bonding π states, while the conduction band is formed by the anti-bonding π* states. The three-dimensional Brillouin zone is shown in Figure1. 10a as a red color for π* (conduction) and a blue color for π (valence) bands. These states are perpendicularly oriented to the molecular plane; there is no avoided crossing, and valence and conduction bands touch at six points, the so-called Dirac points.

Graphene has theoretically a large surface area (2,630 m^2g^{-1}), high electronic mobility (200,000 $cm^2v^{-1}s^{-1}$), high Young's modulus (~1.0 TPa), lower resistivity (~10^{-6} Ωcm) and high thermal conductivity (~5000 $Wm^{-1}K^{-1}$). It also has outstanding optical transmittance (~97.7%), good electrical conductivity and strong chemical durability.[128,129] These unusual properties of graphene have facilitated the extensive application in

electronics and photonics, especially in DSSCs. For more wide application of graphene, the quality and technique of synthesis should be continually improved.

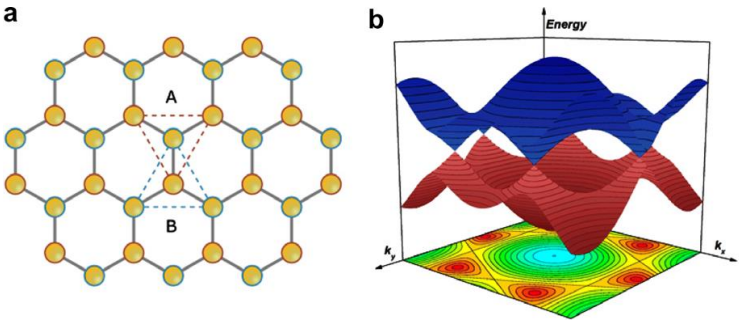

Figure 1. 10. Representation of atomic and electronic structures of graphene. (a) Two graphene triangular sub-lattices, which is A, and B and unit cell. (b) $\pi-\pi^*$ band structure of graphene.[128]

1. 4. Graphene counter electrode in DSSCs

There are several important factors to be a good counter electrode in DSSCs.[130] The counter electrode should have (i) a minimum resistance to collect electrons in an external circuit/redox electrolyte, (ii) a good catalytic activity and stability for the reduction of triiodide to iodide ions, and (iii) high exchange current densities for effective reduction of the oxidized species. Noble metal Pt is the most conventional counter electrode material in DSSCs, because of their excellent electro-catalytic activity and good stability toward the electrolyte.[131-133] However, several alternative materials should be explored to replace noble Pt counter electrode because of their problems related to high-cost and limited resource.

Graphene is an attractive material as an alternative counter electrode in DSSCs, due to its main peculiarities such as cost-effectiveness, environmental friendliness, corrosion resistance and excellent catalytic activity, which decrease charge transfer resistance (R_{ct}). It allows us to achieve smaller, more flexible, and more efficient nano-devices. Kaniyoor and Ramaprabhu reported that the R_{ct} of thermally exfoliated graphene (TEG)

films was 11.7 Ωcm^2, which was very close to that of Pt electrodes (6.5 Ωcm^2).[134] The photo-conversion efficiency of the DSSCs fabricated with TEG as a counter electrode was about 2.8%, comparable to that (about 3.4%) of Pt-based DSSCs. Zhang *et al.* also fabricated graphene nanosheets (GN)-based counter electrode for DSSCs by the oxidative exfoliation of graphite; the maximum obtained efficiency for this process was 6.8%.[135] They found that the annealing temperature for GNs was an important factor, which resulted in a high efficiency and the optimized temperature was about 400 °C. The photovoltaic performance of a DSSC based with a graphene counter electrode is dependent on the structure of graphene. Perfect graphene has an extremely high conductivity, but it may possess a limited number of active sites for I_3^-/I^- electrocatalysis.[29] Kavan *et al.* investigated that the electrocatalytic activity of GNs was considerably associated with its defects and oxygen containing functional groups.[136] It is well known that lattice surface defects of graphene sheets are considered as electrocatalytic active sites.[130] Roy-Mayhew *et al.* proved that increasing the number of oxygen-containing functional groups in GNs improved its electrocatalytic activity.[137]

1. 4. 1. Graphene/polymer composites

Graphene-based composite materials have attracted much attention since Stankovich *et al.* reported the composite materials of graphene with conducting polymer.[138] Hong *et al.* also employed graphene/conductive polymer composite films as counter electrodes in DSSCs.[139] As shown in Figure 1. 11a, the graphene sheets could be dispersed in the (3,4-ethylenedioxythiophene)poly(styrenesulfonate) (PEDOT-PSS) because of strong static interactions between 1-pyrenebutyrate (PB)-functionalized graphene sheets and the PEDOT chains. In this system, graphene sheets enhanced catalytic activity for I_3^-/I^- electrocatalysis, while PEDOT-PSS arranged a highly conductive matrix around the graphene sheets.

Otherwise, Wang *et al.* fabricated a nanocomposite material with polyaniline (PANI) on graphene sheets by an in situ polymerization to disperse a conductive polymer on graphene sheets.[140] The graphene sheets were coated with polyaniline nanoparticles homogeneously as shown Figure 1. 11b. The DSSC based on the PANI/graphene counter electrode achieved a high conversion efficiency of 6.09%, which was close to that

(6.88%) of the conventional cell based on Pt counter electrode. Lee *et al.* developed dispersed PEDOT on a graphene layer as a counter electrode for DSSCs, which gave an efficiency of 6.26%, because of the high loading of graphene into the PEDOT, higher electronic charge transfer and electrochemical activity.[141]

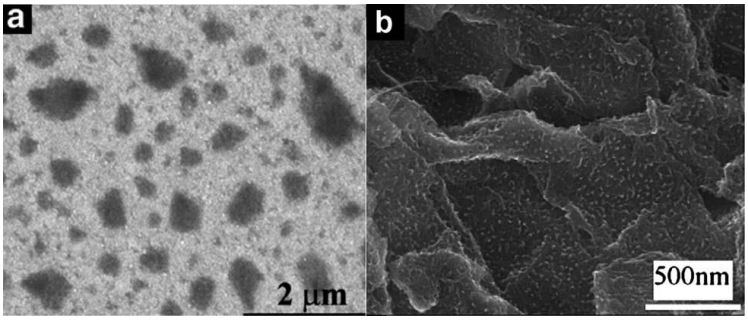

Figure 1. 11. SEM images of (a) the graphene/PEDOT-PSS composite and (b) the graphene/PANI composite.[130]

1. 4. 2. Graphene/metal composites

Graphene/metal composites as counter electrode for DSSCs have developed in various approaches. Gong *et al.* fabricated a Pt/graphene composite material (Figure 1. 12a) through the self-assembly of polyelectrolyte.[142] The DSSC with the Pt/graphene composite as a counter electrode achieved a power conversion efficiency of 7.66%, comparable to that (8.16%) of the DSSC with a sputtered-Pt counter electrode. Moreover, Bajai *et al.* revealed that photovoltaic performance of the DSSCs improved depending on Pt loading on graphene by a pulsed laser ablation method (Figure 1. 12b-c).[143] The amount of Pt loading had a remarkable influence on the efficiency of the resulting DSSCs.

Dou *et al.* synthesized $Ni_{12}P_5$/graphene composites in which $Ni_{12}P_5$ nanoparticles were embedded into the graphene sheets by a hydrothermal reaction to form counter electrodes (Figure 1. 12d).[144] They demonstrated that the $Ni_{12}P_5$/graphene showed high electrocatalytic activity for I_3^- reduction, resulting in a high efficiency (5.7%) for the DSSC based with the $Ni_{12}P_5$/graphene as counter electrode. Tungsten carbide (WC)

was also applied to form a composite material with graphene (GN) which is another alternative composite material for the counter electrode. Tungsten carbide (WC) had a Pt-like catalytic characteristics, high stability and low resistance.[145, 146] A WC–GN composite material led to a high efficiency of 5.88% in DSSCs, with a high current density and fill factor.

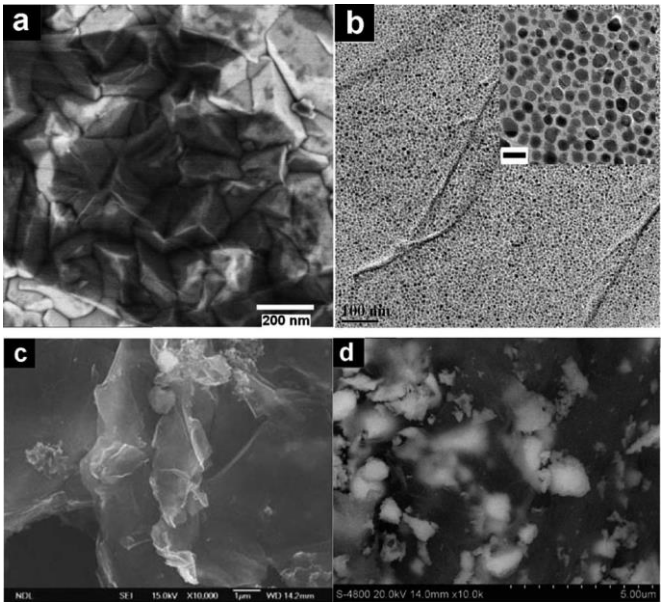

Figure 1. 12. SEM images of (a) the FTO/graphene/Pt counter electrode, (b) the graphene/Pt composite, (c) the graphene/Pt composite and (d) the graphene/$Ni_{12}P_5$ composite.[130]

1. 4. 3. Graphene/carbon nanotube composites

Graphene with carbon materials has been investigated considerably for catalytic materials for DSCCs. Choi *et al.* reported an energy conversion efficiency of 3.0% for the DSSCs based with graphene/multi wall carbon nanotube (MWCNT) composite material as counter electrode.[147] By growing MWCNT on graphene layers via chemical vapor deposition (CVD), graphene/MWCNT counter electrode was fabricated as shown Figure 1. 13a. The *J*–*V* curves of the DSSCs with the graphene/MWCNT counter electrode are shown in Figure 1. 13b.

The composite material includes a graphene–CNT network structure exhibited an excellent contact between the graphene layers and the CNTs. The DSSCs with the graphene/CNT composite counter electrodes showed the increased efficiency of the DSSC (reaching a maximum value of 6.17% at 60% CNTs) with an increasing of CNTs to graphene and then dereased. Battumur *et al.* proved the optimized content (60%) of CNTs in the graphene/CNT composite counter electrode.[148] The initial increase in the efficiency of the DSSC came from the formation of a graphene–CNTs network structure, whereas the

lateral decrease may be result from a lower specific surface area of CNTs in comparison to graphene sheets.

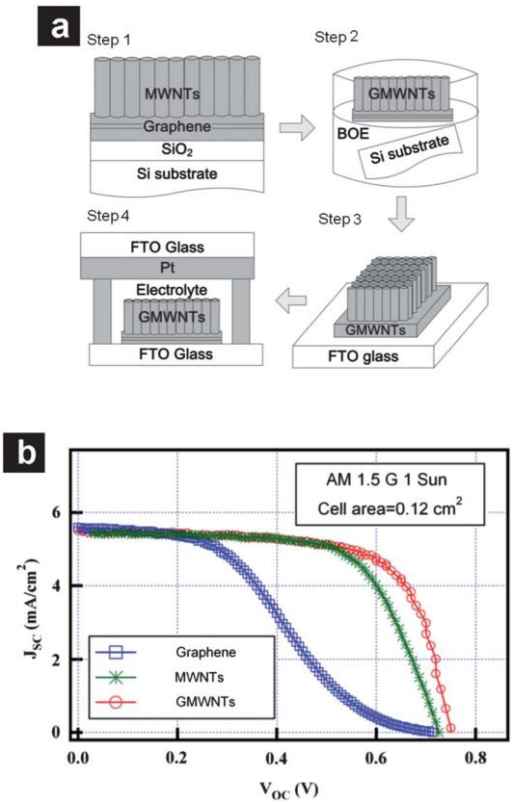

Figure 1. 13 (a) A schematic images of fabrication of DSSCs based on graphene/MWCNT (1) synthesis of graphene/ MWCNTs on SiO_2/Si, (2) the lift−off process of graphene/ MWCNTs, (3) the transplant to FTO glass, (4) half the cell without TiO_2 and dye and (b) the *J*–*V* curves of DSSCs with different counter electrodes: graphene, MWCNTs and graphene/MWCNTs.[130]

Chapter 2

Experimental Section

2. 1. Preparation of Ag nanoplates

2. 1. 1. Preparation of Ag seeds

0.30 mL of 10 mM silver nitrate solution and 20 mL of 1 mM trisodium citrate solution were mixed together. To this solution, 1.8 mL of ice-cold 10 mM sodium borohydride is rapidly injected and mixture is stirred vigorously. The whole solution is aged for 3 h at room temperature.[103]

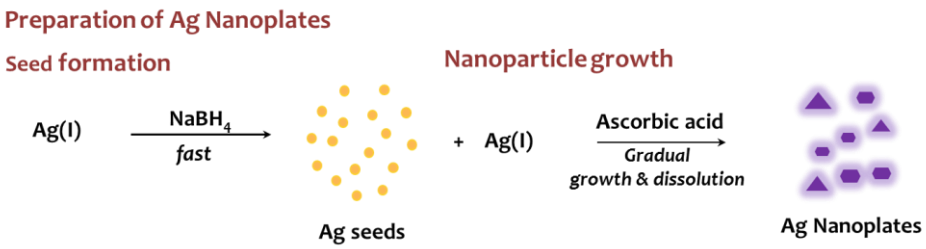

Figure 2. 1. Schematic image of preparation of Ag nanoplates.

2. 1. 2. Preparation of colloidal Ag nanoplates

Ag nanoplates are prepared by a one or two-step seed-mediated process as shown Figure 2. 1. The size of Ag nanoplates is controlled by varying the volume of the Ag seed solution relative to the volume of the trisodium citrate solution. X (1, 2, 4, or 8) mL of the Ag seed solution, (20 – X) mL of 1 mM trisodium citrate solution and 0.2 mL of 20 mM ascorbic acid solution were mixed together. To this solution, 0.80 mL of 10 mM silver nitrate solution is rapidly injected and mixture is stirred for 30 min. For the second process, 10 mL of the final mixture solution, 10 mL of 1 mM trisodium citrate solution and 0.60 mL of 20 mM ascorbic acid solution were mixed. To this solution, 0.80 mL of 10 mM silver nitrate solution is rapidly injected and mixture is stirred for 30min.

2. 2. Preparation of panchromatic Ag nanoplates

Panchromatic Ag nanoplates are synthesized by rapid thermal process (Figure 2. 2.). 25 mL of 0.1 mM silver nitrate, 1.5 mL of 30 mM trisodium citrate, 1.5 mL of 0.7 mM poly(vinylpyrolidone) (weight average molecular weight; ~29000 g/mol) and 60 μL of 30 wt% hydrogen peroxide were mixed together. To this solution, 60 μL of X (60, 80, 100) mM sodium borohydride is rapidly injected and then stirred vigorously for 45 min. Color of colloid solutions become pale yellow after injection, and then slowly changes to orange or purple or blue, indicating the growing of Ag nanoplates. The size of Ag nanoplates is controlled by varying the concentration of the sodium borohydride solution injected.[104]

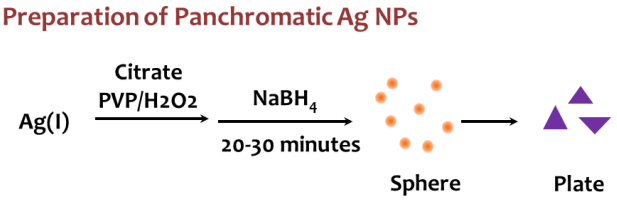

Figure 2. 2. Schematic image of preparation of panchromatic Ag nanoplates.

2. 3. Preparation of Au nanoparticles

Au spheres are prepared following a previously reported method.[102] 0.5 mM of $HAuCl_4$ (50 mL) is heated at 90 ℃ for 1 h. 1.5 mL of a 1% sodium citrate solution is injected into the heated solution, and stirred for 30 min at 90 ℃. The size of the fabricated Au NPs is 17 ± 4 nm.

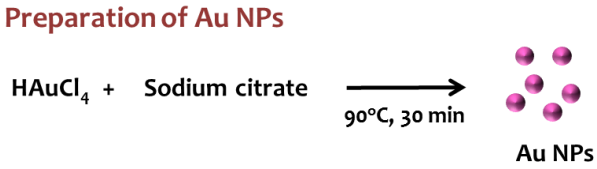

Figure 2. 3. Schematic image of preparation of Au NPs.

2. 4. Preparation of graphene flakes

Dispersible graphene flakes are produced using a thermal plasma jet system following the method that we had developed (see Figure 2. 4.).[149] A carbon tube (20 cm in length; 1 cm in inner diameter) is attached to the anode, and a polished graphite plate is placed, perpendicular to and, 10 cm away from the end of the attached carbon tube. Ethylene gas (0.5 L/min) as a carbon source is continuously injected into the plasma torch. The suspension of graphene flakes is prepared by adding 45 mg graphene flakes to 30 mL of dimethylformamide (DMF) and then dispersing the flakes by sonication for 1 h.[150]

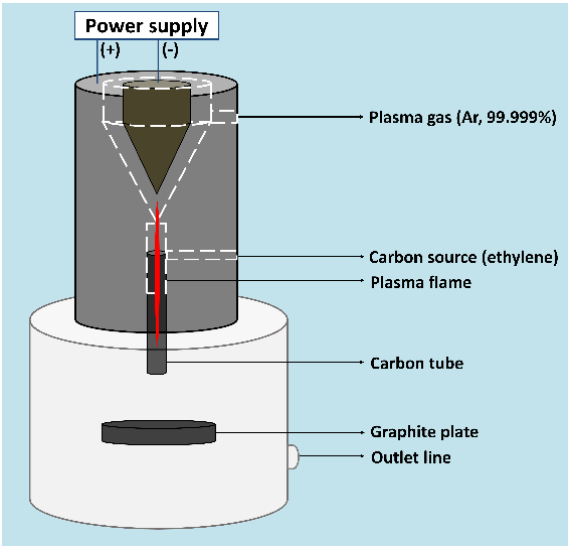

Figure 2. 4. Schematic image of the thermal plasma system for fabrication of graphene flakes.

2. 5. Fabrication of DSSCs

FTO (fluorine-doped thin oxide) glass is cleaned by sonication method in a detergent solution and ethanol for 10 min, respectively. A TiO_2 blocking layer is formed on washed FTO glass by spin-coating with 5 wt% of titanium di-isopropoxidebis(acetylacetonate) in butanol and annealed at 450 ℃ for 1 h. The TiO_2 photoactive layer is prepared from TiO_2 pastes (T/SP, solaronix) by the doctor blade technique with annealing in air at 450 ℃ for 1 h. A paste for the scattering layer (DSL 18NR-AO, Dyesol) is doctor bladed and then dried at 50 ℃ for 2 h. The resulting film is treated by titanium isopropoxide (TIP) solution (0.1 M in isopropyl alcohol) at 90 ℃ for 30 min, and followed by annealing at 450 ℃ for 30 min. The TiO_2 films are immersed into a N719 (solaronix) dye solution in ethanol under heating condition to 50 ℃ for 12 h. Pt-layered counter-electrodes are prepared by drop-coating H_2PtCl_6 solution (0.5 M in EtOH) onto FTO glass and then sintered at 400 ℃ for 30 min. The photoanode is further sandwiched by Pt-coated FTO glass, by using a 60 μm-thick surlyn. The composition of the electrolyte is as

follows: 0.7 M of 1 butyl −3−methyl imidazolium iodide (BMII), 0.03 M of I_2, 0.1 M of guanidium thiocyanate (GSCN), and 0.5 M of 4 tert−butyl pyridine (TBP) in a mixture of acetonitrile and valeronitrile (85: 15 v/v).[102−104]

2. 6. Characterization

2. 6. 1. EF-TEM

The structure and size of metal NPs are confirmed by an energy-filtering transmittance electron microscope (EF-TEM, Carl Zeiss, LIBRA 120).

2. 6. 2. HR-TEM

High-resolution transmission electron microscope (TEM; JEOL, JEM-3000F (300 kV)) is used to analyse for metal NPs and graphene flakes.

2. 6. 3. FE-SEM

The surface morphology of fabricated films is identified by a field emission scanning electron microscope (FE-SEM) (JSM-6330F, JEOL Inc.).

2. 6. 4. Solar simulator

Current density– voltage (J–V) characteristics of the DSSCs are measured using an electrometer (KEITHLEY 2400) under AM 1.5 illumination (100 mW/cm^2) provided by a solar simulator (1 kW xenon with AM 1.5 filter, PEC-L01, Peccel Technologies).

2. 6. 5. IPCE

The incident photon-to-current conversion efficiency (IPCE) is measured using a McScience model K3100 with reference to the calibrated diode. A 300 W xenon lamp is used as a light source for the generation of a monochromatic beam. The bias light is supplied by a 150 W halogen lamp.

2. 6. 6. EIS

Electrochemical impedance spectroscopy (EIS) is carried out with a potentiostat (Solartron 1287) equipped with a frequency response analyzer (Solartron 1260), with the frequency ranging from 10^{-1} to 10^{5} Hz. The applied bias voltage and ac amplitude are set at the open circuit voltage (V_{oc}) of the DSSCs and 10 mV, respectively. The impedance measurements are carried out at open-circuit potential under AM 1.5 one-sun light illumination. The EIS is analysed by Z-view software (Solartron Analytical) with appropriate equivalent circuit.

2. 6. 7. CV

Cyclic voltammetry (CV) measurements are carried out with CHI600E (CH Instruments) in an acetonitrile solution containing 0.1 M $LiClO_4$, 10 mM LiI, and 1 mM I_2 at room temperature under an inert atmosphere of argon, equipped with a platinum wire counter electrode and $Ag/AgNO_3$ (0.1 M) reference electrode.

2. 6. 8. Raman Spectroscopy

Raman measurements are carried out through a micro-Raman spectrometer equipped with a monochromator (SPEX 500M) and a liquid nitrogen cooled CCD camera (Roger Scientific 7346-001).

2. 6. 9. X-ray Photoelectron Spectroscopy (XPS)

X-ray photoelectron spectroscopy (XPS) analysis is performed using a PHI 5000 Versa Probe™ ULVAC system with an Al Ka X-ray source (hν ¼ 1486.6 eV), which obtained a 15 kV and 20 mA beam, and an HSA analyzer.

Chapter 3

Aggregation Effect of Silver Nanoparticles on the Energy Conversion Efficiency of the Surface Plasmon-Enhanced Dye-Sensitized Solar Cells

3. 1. Concept

We have fabricated Ag nanoplates that have two broad extinction bands in the visible region, which are well matched with two visible absorption bands of N719 dye.[103] The efficiency of the dye-sensitized solar cells (DSSCs) based on composite films consisting of TiO_2 nanoparticles (NPs) and Ag nanoplates (TiO_2/Ag films) was affected by the degree of the spectral overlap between these bands and the weight percent of Ag nanoplates to TiO_2 NPs. By optimizing the size and geometry of Ag nanoplates and the weight percent of Ag nanoplates to TiO_2 NPs, the energy conversion efficiency significantly improved from 8.7% to 10.3%. However, the efficiency increased up to 0.35 wt% of Ag nanoplates but then decreased when the weight percent was further increased. The cause of the efficiency decrease for a further increase of Ag weight percent was investigated. N719 dye has two strong absorption bands centered at 393 and 533 nm, while black dye centered at 410 and 610 nm. The in-plane mode of the localized surface plasmon of Ag nanoplates near 530 nm is red-shifted when they are aggregated. Therefore, an enhanced

absorption is expected at around the surface of the isolated Ag nanoplates for N719 dye, while aggregated ones for black dye. The extinction of the TiO_2/Ag films adsorbed N719 dye was the highest when Ag nanoplates was 0.35 wt%, while that adsorbed black dye increased with increasing up to 0.7 wt%. This means that aggregation of Ag nanoplates took place significantly when the weight percent was higher than 0.35. When Ag nanoplates was higher than 0.35 wt%, the efficiency of the plasmon enhanced absorption of N719 dye might be decreased by aggregation and consequently the energy conversion efficiency was decreased. Therefore, it suggested that to get a high efficiency of surface plasmon-enhanced DSSCs, the aggregation of metal NPs should be controlled in the fabrication of the composite films.

3. 2. Fabrication of plasmonic photoanode

The photoanodes incorporated with Ag nanoplates and TiO_2 NP paste (ratio of Ag nanoplates to TiO_2 NPs is from 0.15 to 0.7 wt%) were prepared with a modified procedure. Ag nanoplates were mixed with TiO_2 NP paste (T/SP, solaronix) in methyl alcohol, followed by stirring and sonication, and then the solvent was evaporated in vacuum. The TiO_2 NP/Ag nanoplates composite materials were treated onto the FTO glass by the doctor blade technique, and then heated gradually at 450 ℃ for 1 h. The scattering TiO_2 NP pastes (DSL 18NR-AO, Dyesol) were coated by doctor blade and then dried at 50 ℃ for 2 h. The resulting films were treated with titanium isopropoxide (TIP) solutions (0.1 M in isopropyl alcohol) at 90 ℃ for 30 min, and followed by annealing at 450 ℃ for 30 min. The TiO_2/Ag films were immersed into a N719 (solaronix) dye solution in ethanol under heating to 50 ℃ for 12 h.

3. 3. Result and discussion

3. 3. 1. Characterization of Ag nanoplates

3. 3. 1. 1 TEM images of Ag nanoplates

Figure 3. 1. shows the TEM images of Ag seeds (3. 1e) and Ag nanoplates fabricated by a one-step or two-step seed-mediated process (3. 1a-d). Ag seeds were spherical NPs with sizes from 7 to 12 nm. The average size of Ag nanoplates shown in Figures 1a-d is 20, 35, 45 and 50 nm, respectively. Ag nanoplates shown in Figure 3. 1a were fabricated by a one-step seed-mediated process, while those shown in Figure 3. 1b-d were fabricated by a two-step seed-mediated process. With increasing the average size, more nanoplates existed than spheres. Our Ag nanoplates were not uniform in shape. Some had sharp edge and corners. It is known that the sharp edge and corners of metal nanoparticles can generate a stronger surface plasmon resonance on the sharper parts, compared to the spherical shape.[151,152]

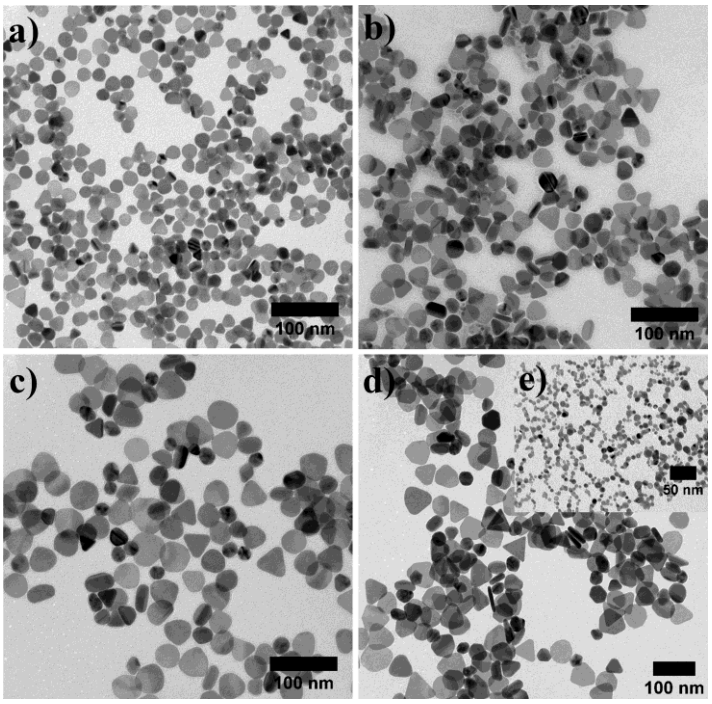

Figure 3. 1. TEM images of Ag nanoplates fabricated by a one-step (a) or two-step (b-d) seed-mediated process and silver seeds (e). Average sizes are (a) 20, (b) 35, (c) 45, (d) 50, and (e) 10 nm.

2. 3. 1. 2 UV-visible spectra of Ag nanoplates

The UV-vis extinction spectra of these Ag nanoplate solutions, except Ag seed solution, are shown in Figure 3. 2a. For comparison, the absorption spectrum of N719 dye dissolved in ethanol is also shown in Figure 3. 2b. The spectrum of Ag seed solution displayed a surface plasmon resonance peak at λ_{max} 390 nm. After the seeded growth into nanoplates, a remarkable change in extinction was observed.

Extinction spectra measured from the Ag nanoplate solutions showed double-peaked plasmon resonances, which extended even to the red region. With increasing average size of Ag nanoplates, the λ_{max} of the strong peak near 400 nm was red-shifted slightly, while that at longer wavelength was red-shifted greatly. A surface plasmon resonance peak located at a longer wavelength (490~680 nm) originates from in-plane dipolar plasmon resonances of hexagonal plates, while that located near 420 nm may be attributed to out-of-plane dipolar plasmon resonances.[153] A weak shoulder near 335 nm is due to the quadrupole plasmon resonances. In the dye spectrum, the two strong absorption bands centered at 393 and 533 nm are due to the metal-to-ligand charge transfer transitions of

ruthenium dye molecules. Two extinction bands of Ag nanoplates whose average size was about 35 nm were best matched with two visible absorption bands of N719.

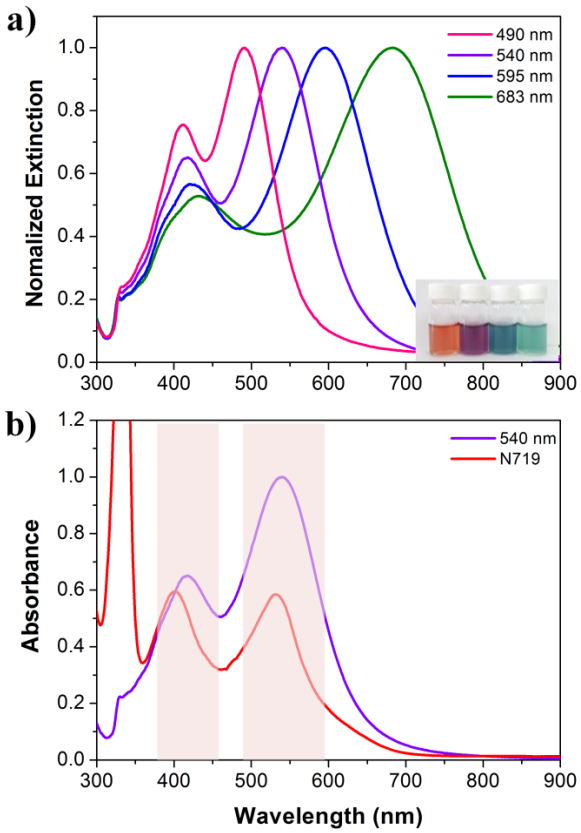

Figure 3. 2. (a) Normalized UV-vis extinction spectra of the colloidal Ag nanoplates solutions fabricated by a one-step or two-step seed-mediated process, whose average sizes of Ag nanoplates were 20, 35, 45 and 50 nm (from left to right). (b) Comparing the absorption spectrum of N719 dye dissolved in ethanol and the extinction spectrum whose λ_{max} is 540 nm. The legends, except N719, represent the values of the λ_{max} of the extinction spectra. Inset is a photograph picture of the colloidal Ag nanoplate solutions.

3. 3. 2. Photovoltaic properties of plasmonic DSSCs

Two different types of DSSCs were fabricated to investigate the effect of surface plasmon from Ag nanoplates on photovoltaic parameters of DSSCs. One is the conventional DSSC based on only TiO_2 NPs, and the other is the plasmon-enhanced DSSC based on a composite of TiO_2 and Ag nanoplates. In the case of DSSCs incorporated with Ag nanoplates, pre-treatment with TIP was required to prevent the direct corrosion of Ag nanoplates and photogenerated charge recombination by electrolytes. This method has been used by Jeong *et al.*[89] They have studied in detail the effect of treating Ag NPs with TIP and proved that this treatment is sufficient for preventing silver corrosion and electron leaking from Ag NPs. It should be mentioned that for making pairwise comparisons we also pre-treated the conventional DSSC based on only TiO_2 NPs with TIP. The thickness of the TiO_2 film including the scattering layer of ~8 μm was about 19 μm and that of Ag-TiO_2 films was 14 μm.

In Figure 3. 3a, the photocurrent density−voltage ($J-V$) curves measured in air mass 1.5 sunlight from the DSSC based on a film consisting of only TiO_2 NPs (TiO_2−only DSSC) and the DSSCs based on composite films consisting of TiO_2 and four different sizes of Ag nanoplates (TiO_2/Ag DSCCs) were compared. In each composite film, a 0.35 wt% of each kind of Ag nanoplates was included. It was the optimum weight percent of Ag nanoplates for the composite films (see Figure 3. 5). A significant increase in the photocurrent density was measured from each plasmon−enhanced DSSC. The photovoltaic parameters are listed in Table 3. 1. The short−circuit current density (J_{sc}) increased substantially from 16.0 ± 0.2 up to 18.5 ± 0.4 mA/cm^2, while the open−circuit voltage (V_{oc}) and the fill factor (ff) remained relatively unchanged. The highest energy conversion efficiency (η) was 10.3%, which was measured from the composite film of TiO_2 NPs and Ag nanoplates whose average size was about 35 nm. Two extinction bands of the Ag nanoplates were well matched with two visible absorption bands of N719 (see Figure 3. 2b). It should be mentioned that the efficiency of our surface plasmon−enhanced DSSCs based on Ag nanoplates is higher than any

reported ones based on Ag nanospheres.[105, 89]

The incident photon-to-current conversion efficiency (IPCE) spectra measured from the five DSSCs are shown in Figure 3. 3b. By incorporating Ag nanoplates, IPCE over the wavelength range from 400 to 700 nm was enhanced, exhibiting the maximum wavelength of 530 nm which was closely associated with ruthenium dye absorption. The relative intensity of IPCE spectra of TiO_2/Ag DSSCs was closely related to the degree of the spectral overlap between the extinction bands of Ag nanoplates included in fabrication of DSSCs and the absorption bands of N719 dye. It was highest for the DSSC included the Ag nanoplates whose λ_{max} of the in-plane dipolar plasmon resonance peak was 540 nm, while lowest for that included the Ag nanoplates whose λ_{max} was 683 nm. The degree of the spectral overlap was highest for the Ag nanoplates whose λ_{max} was 540 nm, while it was the lowest for the Ag nanoplates whose λ_{max} was 683 nm. For the DSSC included Ag nanoplates whose λ_{max} was 490 nm, the conversion efficiency was 9.8 ± 0.1%, which was the second highest. However, its IPCE intensity in the region of 600-750 nm was the lowest. Among four kinds of Ag nanoplates, the Ag nanoplates whose λ_{max} was 490 nm had the lowest

extinction intensity in the wavelength region of 600−750 nm.

It is clearly seen in the IPCE improvement factor spectra shown in Figure 3. 3c. The factor has been calculated by the following equation: $\Delta IPCE\ (\lambda) / IPCE\ (\lambda)\ \% = [(IPCE_{DSSC\ based\ on\ composite\ film\ (\lambda)} - IPCE_{DSSC\ based\ on\ TiO2\ only\ film\ (\lambda)}) / IPCE_{DSSC\ based\ on\ TiO2\ only\ film\ (\lambda)}] \times 100$. The intensity of IPCE in the wavelength region between 350 and 450 nm was also significantly enhanced. The out−of−plane dipolar plasmon resonance of Ag nanoplates takes place in this wavelength region and one of two visible absorption bands of N719 dye does also take place in this region. The increased IPCE from the DSSCs included Ag nanoplates could be primarily attributed to the enhanced dye absorption by surface plasmon, since the short−circuit current density increased substantially, while the open−circuit voltage and the fill factor remained relatively unchanged (see Table 3. 1). Therefore, it is concluded that the energy conversion efficiency of our TiO_2/Ag DSSCs is significantly enhanced by the enhanced dye absorption through an energy matching between absorptions of N719 dye and surface plasmon resonances of Ag nanoplates.

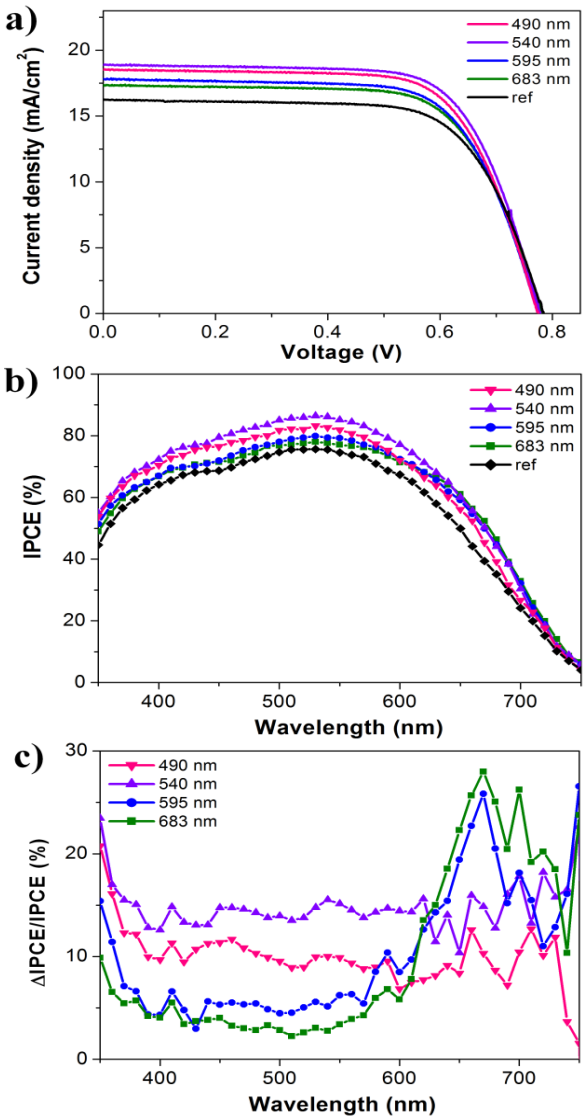

Figure 3. 3. (a) Photocurrent density−voltage ($J-V$) curves and (b) IPCE spectra measured from the TiO_2 DSSC and four TiO_2/Ag(0.35 wt%) DSSCs, and (c) the relative IPCE improvement factor [ΔIPCE (λ) / IPCE (λ) %] spectra. The legend represents the values of the λ_{max} of in−plane dipolar plasmon resonance peak of the Ag nanoplates that were included in the fabrication of each TiO_2/Ag DSSC.

Table 3. 1. Photovoltaic properties of the TiO_2 only (reference) and TiO_2/Ag(0.35 wt%) DSSCs.

λ_{max} of Ag nanoplate solutions	V_{oc} (V)	J_{sc} (mA/cm^2)	*ff*	η (%)
490 nm	0.78 ± 0.01	18.1 ± 0.2	0.70 ± 0.02	9.8 ± 0.1
540 nm	0.78 ± 0.01	18.5 ± 0.4	0.70 ± 0.02	10.1 ± 0.2
595 nm	0.78 ± 0.01	17.5 ± 0.4	0.69 ± 0.01	9.5 ± 0.1
683 nm	0.78 ± 0.01	17.2 ± 0.2	0.69 ± 0.01	9.2 ± 0.1
Reference	0.78 ± 0.01	16.0 ± 0.2	0.69 ± 0.01	8.6 ± 0.1

3. 3. 3. Plasmonic effect in DSSCs

To clarify the effect of surface plasmon arising from the Ag nanoplates on the absorption of dye molecules, the extinction spectra of TiO_2 film and TiO_2/Ag films were systematically monitored. The extinction spectra measured from the only TiO_2 NPs films and TiO_2/Ag films, before and after adsorption of N719 dye molecules, are shown in Figure 3. 4a. All the films were post-treated with TIP and the weight percent of Ag nanoplates was 0.35% for all the composite films. Without adsorption of dye molecules, the extinction intensity decreased smoothly with increasing wavelength (see two smooth lines in Figure 3. 4a). The intensity of the TiO_2/Ag film was significantly higher than that of the TiO_2 film in the visible light region except near 400 nm. However, there was no conspicuous band corresponding to the surface plasmon resonance peaks of Ag nanoplates, which were observed between 400 and 700 nm in Figure 3. 2a. With adsorption of dye molecules on these films, a broad band of N719 dye molecules centered near 530 nm was observed. The intensity of the TiO_2/Ag films was

significantly higher than that of the TiO_2 film. The λ_{max} of the composite films was slightly shifted from that of the TiO_2 film.

The intensity increase was clearly seen in the enhancement factor spectra (see Figure 3. 4b). The enhancement factor had been calculated by the following equation: $\Delta I(\lambda)/I(\lambda)\ \% = [(I_{\text{extin. of dye adsorbed composite film }(\lambda)} - I_{\text{extin. of dye adsorbed TiO2 only film }(\lambda)})/I_{\text{extin. of dye adsorbed TiO2 only film }(\lambda)}] \times 100$. Each spectrum had a broad band in the wavelength region from 400 to 600 nm. In the wavelength region beyond 600 nm, it was very noisy due to the weak intensity and very little intensity difference. The position and relative intensity were related to the overlap between the absorption bands of N719 dye and the surface plasmon resonance of Ag nanoplates. For example, the λ_{max} of the relatively large Ag nanoplates was in the longer wavelength region than the λ_{max} of dye (530 nm) (see Figure 3. 2a), and the overlap could take place dominantly in the longer wavelength region than 530 nm. Actually, the broad enhancement factor band measured from the composite film included Ag nanoplate whose λ_{max} was 595 or 683 nm was centered near 570 nm (see Figure 3. 4b). The relative intensity was stronger for the composite film included Ag nanoplates whose λ_{max} was

595 nm than 683 nm. This result agreed with the magnitude of the overlap between the absorption bands of N719 dye and the surface plasmon resonance of Ag nanoplates. The overlap could take place more greatly for the Ag nanoplates whose λ_{max} was 595 nm than 683 nm (see Figure 3. 2). Therefore, it was concluded that the absorption intensity improvement was due to the surface plasmon enhanced absorption of dye molecules on or near Ag nanoplates. The interaction between dye molecular dipole and enhanced electromagnetic field by the surface plasmon of Ag nanoplates appeared to contribute to the marked increase in dye absorption.[105] The intensity of the composite film including the Ag nanoplates whose λ_{max} was 540 nm was 1.16 times higher than that the film of TiO_2 NPs. However, it was not completely clear how the surface plasmon enhanced absorption could take place from the TiO_2/Ag films treated with TIP, in which no conspicuous surface plasmon resonance was observed. It should be studied in detail.

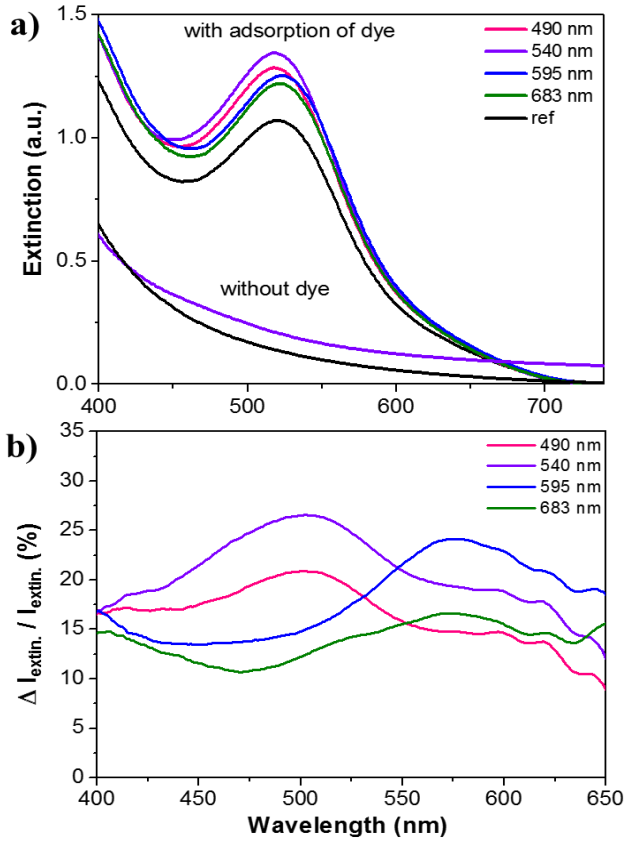

Figure 3. 4. (a) Extinction spectra of the film of only TiO_2 NPs (TiO_2 film; labelled as ref.) and films of TiO_2/Ag nanoplate composite (TiO_2/Ag films), before and after N719 dye adsorption. (b) The relative extinction improvement factor $[\Delta I_{extin.}(\lambda)/I_{extin.}(\lambda)\%]$ spectra. The weight percent of Ag nanoplates was 0.35%. The legend represents the values of the λ_{max} of in-plane dipolar plasmon resonance peak of the Ag nanoplates that were included in the fabrication of composite films.

2. 3. 4. Optimazation of plasmonic DSSCs

The dependence of η and J_{sc} of plasmon-enhanced DSSCs on Ag nanoplate weight percent was also investigated. Ag nanoplates whose average size was 35 nm were used in fabrication of TiO_2/Ag DSCCs. As shown in Figure 3. 5, as the weight percent of Ag nanoplates was raised up to 0.35 wt%, the η value was gradually increased from 8.6 ± 0.1% up to the maximum value, 10.1 ± 0.2%. Further increase in the weight percent of Ag nanoplates to 0.70% actually caused a decrease in the η values to 9.2 ± 0.1%. A trend observed from the change in the energy conversion efficiency was found to be in agreement with that from a change in the photocurrent density. The J_{sc} value was enhanced from 16.0 ± 0.2 to 18.5 ± 0.4 mA/cm^2 as the weight percent of Ag nanoplates approached 0.35%, and a further increase of Ag weight percent led to a decrease in J_{sc}.

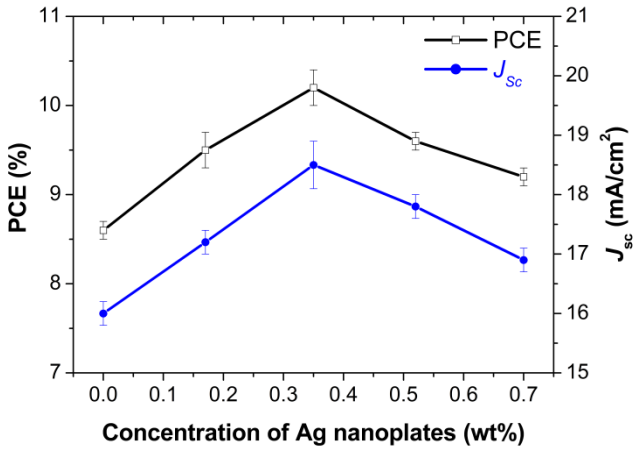

Figure 3. 5. Dependence of Ag nanoplate weight percent on η and J_{sc} values with error bar measured from TiO_2/Ag DSSCs. The average size of Ag nanoplates included in the fabrication of DSSCs was 35 nm.

2. 3. 5. Aggregation effect in DSSCs

With increasing the weight percent of Ag or Au NPs to TiO_2 NPs, the energy conversion efficiency of plasmon-enhanced DSSCs decreased after increasing up to a certain weight percent.[88,89,100,101,105] In Figure 3. 5, the energy conversion efficiency increased up to 0.35 wt% of Ag nanoplates but then decreased as the weight percent was increased further. Here, we have studied the cause of the efficiency decrease for a further increase of Ag weight percent by analysing the extinction spectra of TiO_2/Ag composite films adsorbed N719 and black dyes. Figure 3. 6 shows the extinction spectra of TiO_2/Ag composite films adsorbed N719 and black dyes, fabricated by varying the weight percent of Ag nanoplates, whose average size was 35 nm. The extinction of the TiO_2/Ag composite films adsorbed N719 dye was the highest when the weight percent of Ag nanoplates was 0.35%, while that adsorbed black dye increased with increasing the weight percent up to 0.7%, which was the highest weight percent included. Two extinction bands of the isolated Ag nanoplates, whose

average size was about 35 nm, were well matched to two visible absorption bands of N719 dye (see Figure 3. 2).

Therefore, an enhanced absorption of N719 dye molecules might take place on or near the isolated Ag nanoplates. With increasing relative weight percent of Ag nanoplates, the probability of aggregation between Ag nanoplates in the composite films would be increased. It is well known that when Ag NPs are aggregated, the resonance wavelength of the longitudinal mode is red-shifted.[152, 154] Therefore, no or a weak enhanced absorption of N719 dye molecules was expected on or near the surface of the aggregated Ag nanoplates. However, an enhanced absorption of black dye was expected on or near the surface of the aggregated Ag nanoplates, since black dye has a broad absorption near 600 nm. [In the visible region, N719 dye has two strong absorption bands centered at 393 and 533 nm, while black dye centered at 410 and 610 nm.] These expectations were well agreed with the data of Figure 3. 6. It means that aggregation of Ag nanoplates took place significantly as the weight percent was increased further. Therefore, it could be concluded that the decrease of the energy conversion efficiency for a further increase of Ag weight percent is due

to the aggregation of Ag nanoplates. Other possible causes have been suggested such as the increased trapping or quenching of photogenerated electrons by metal NPs and increased light absorption by metal NPs.[105,155]

It should be mentioned that spherical Ag NPs should be aggregated to match their plasmon absorption with the absorption of N719 dye. The plasmon absorption of isolated spherical Ag NPs takes place near 400 nm.[154] Therefore, the cluster of Ag spherical NPs like dimer or trimer should be formed to be matched to the 533 nm absorption band of N719 dye.[154] When the size of clusters becomes relatively large, the resonance wavelength is further red-shifted, and no or a weak enhanced absorption of N719 dye molecules will take place. Therefore, to get a high energy conversion efficiency of surface plasmon-enhanced DSSCs, the aggregation of metal NPs should be properly controlled in the fabrication of the composite films of TiO_2 and metal NPs.

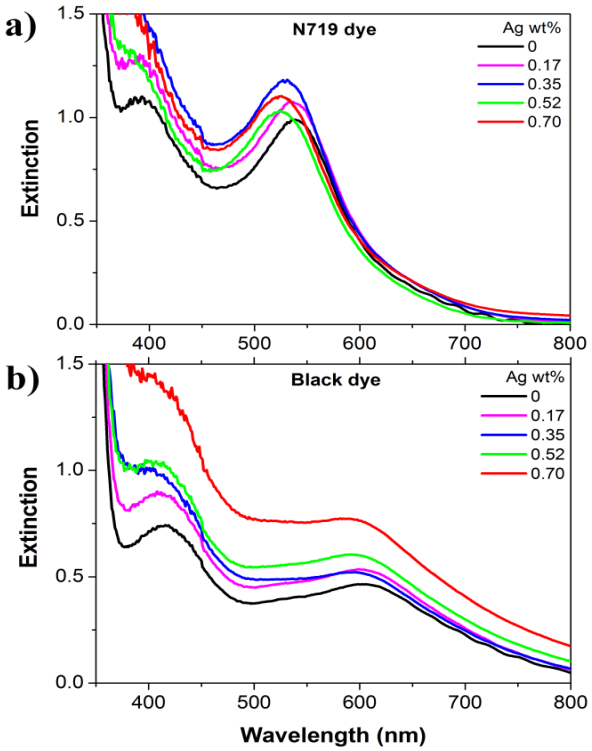

Figure 3. 6. Extinction spectra of the film of only TiO_2 NPs (TiO_2 film) and films of TiO_2/Ag nanoplate composite (TiO_2/Ag film): adsorbed (top) N719 and (bottom) black dye molecules. The legends represent the values of the weight percent of Ag nanoplates included. All films were post-treated with TIP.

2. 3. 6. EIS of plasmonic DSSCs

The characteristic electrochemical impedance spectra for DSSCs based on TiO_2 film and TiO_2/Ag nanoplate film are shown in Figure 3. 7. Each spectrum contains three semicircles. The hemisphere in the high-frequency region is assign to the parallel combination of the resistance and capacitance at the Pt-FTO/electrolyte and to the interface between FTO and TiO_2 layers, while those in the intermediate and low-frequency regions offer information on the resistance and capacitance at the TiO_2/electrolyte interface and the Nernst diffusion of the electrolyte, respectively.[156] No significant difference was observed between the two spectra. It might be represented that a relatively low weight percent of Ag nanoplates does not affect to the resistance and capacitance of the DSSCs.

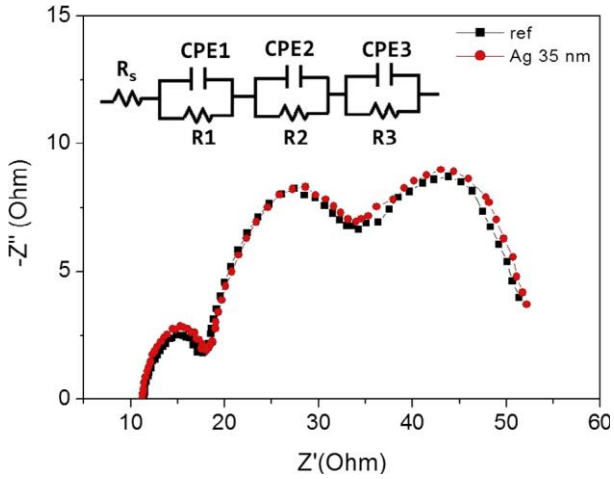

Figure 3. 7. Electrochemical impedance spectra of DSSCs based on TiO_2 film and TiO_2/35 nm Ag nanoplates.

3. 4. Conclusion

We have fabricated Ag nanoplates whose localized surface plasmon resonances match to two visible absorption bands of N719 dye. The energy conversion efficiency of the dye-sensitized solar cells (DSSCs) based on composite films consisting of TiO_2 and Ag nanoplates was affected by the degree of the spectral overlap between the extinction bands of Ag nanoplates and two visible absorption bands of N719 dye, centered at 393 and 533 nm. Also, it was affected by the weight percent of Ag nanoplates to TiO_2 NPs. By optimizing the overlap and weight percent of Ag nanoplates to TiO_2 NPs, the energy conversion efficiency was improved from 8.6 ± 0.1% to 10.1 ± 0.2%. The efficiency decreased for a further increase of Ag weight percent was due to the aggregation of Ag nanoplates. The localized surface plasmon resonances of the aggregated Ag nanoplates were mismatched to two visible absorption bands of N719 dye, and the efficiency of the plasmon enhanced absorption of the dye decreased by the aggregation. To get a high energy conversion efficiency of surface plasmon-enhanced DSSCs, the aggregation of metal

NPs should be controlled in the fabrication of the composite films of TiO_2 and metal NPs.

Chapter 4

Panchromatic Quasi-Monolayer of Ag NPs for High-Efficiency Dye-Sensitized Solar Cells

4. 1. Concept

We developed a panchromatic quasi-monolayer film of Ag nanoparticles (NPs) whose localized surface plasmon resonances take place in all the visible range and applied this technique to fabricate dye-sensitized solar cells (DSSCs). Three kinds of Ag NPs whose λ_{max} at 540, 620 and 470 nm were fabricated. We immobilized them on a photoactive film of TiO_2 NPs coated with poly(4-vinylpyridine) (P4VP), and then deposited a scattering layer. Most Ag NPs were immobilized individually without aggregation, and formed a quasi-monolayer. By constructing a panchromatic quasi-monolayer between the photoactive and scattering layers, the efficiency was enhanced from 8.9 ± 0.3 % to 11.0 ± 0.4%, mainly by enhancing the photocurrent density. The photocurrent density might increase by enhancement of light absorption and electron transfer yield. Absorption of dye molecules might be enhanced on or near the surface of Ag NPs by the localized surface plasmons. Since the quasi-monolayer of Ag NPs scattered light strongly, and therefore absorption of dye molecules that is not adsorbed on or near the surface could be enhanced by the scattered light.

Owing to the enhanced dye absorption, we could reduce greatly the thickness of the photoactive layer. The thickness was about 4.5 μm, corresponding to about one-half the optimum length for the DSSCs not included metal NPs. Our general method could be used in fabrication of other types of solar cells.

4. 2. Fabrication of panchromatic quasi-monolayer of DSSCs

A conventional photoanode based on TiO_2 NPs was fabricated by formation of a blocking layer on FTO glass, and then depositing a relatively thick layer of TiO_2 NPs, and scattering layer. We prepared quasi-monolayer of panchromatic photoanode by including three kinds of Ag NPs, whose λ_{max} was 540, 620 and 470 nm, at between the photoactive layer and the scattering layer. The schematics of the fabrication processes are shown in Figure 4. 1. At first, P4VP was coated on the surface of the TiO_2 NPs photoactive layer and then Ag NPs were immobilized on the prepared TiO_2 NPs photoactive layer coated with P4VP by dipping in Ag colloid solutions. After immobilizing, P4VP was coated again to prevent moving of Ag NPs, and then scattering layer was deposited by a doctor blade printing. Finally, prepared quasi-monolayer of panchromatic photoanode was sintered to remove P4VP. For a panchromatic quasi-monolayer of Ag NPs that takes place in a whole visible region, three kinds of Ag NPs whose λ_{max} was 540, 620 and 470 nm, were immobilized on the TiO_2 NPs photoactive layer in

sequence. In the immobilization of Ag NPs, the surface coverage increased depending on the immobilization time but not linearly. In other words, the immobilization rate of Ag NPs changed depending on saturation of Ag NPs on the surface. Due to this non-linearity, it was very hard to optimize a quasi-monolayer consisting of three kinds of Ag NPs. To simplify, we immobilized each kind of Ag NPs for an equal time. In this case, the efficiency was critically affected by the immobilization order of three kinds of Ag NPs.

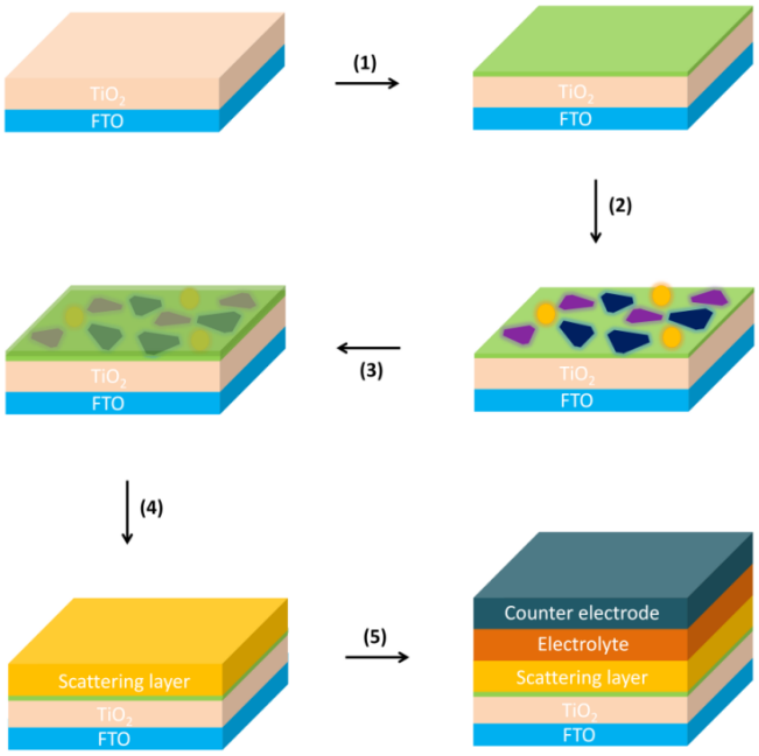

Figure 4. 1. Scheme for construction of the DSSC included a quasi-monolayer of Ag NPs between the layer of TiO_2 NPs and scattering layer: (i) coating P4VP, (ii) immobilization of Ag NPs, (iii) coating P4VP again, (iv) depositing a scattering layer, and fabrication of a DSSC.

4. 3. Result and discussion

4. 3. 1. Characterization of Ag NPs

4. 3. 1. 1. SEM images of panchromatic Ag NPs

Figure 4. 2. shows the scanning electron microscopy (SEM) images of three kinds of Ag NPs immobilized on the surface of cover glass coated with P4VP and schematic of Ag NPs immobilized on P4VP. Most Ag NPs were isolated. Ag NPs shown in Figure 4. 2a were more like spheres, while more like nanoplates in Figure 4. 2b and c. Ag NPs were immobilized on P4VP by an attractive interaction between the lone pair electrons on the nitrogen atom of the pyridine ring and Ag NPs (see Figure 4. 2d).

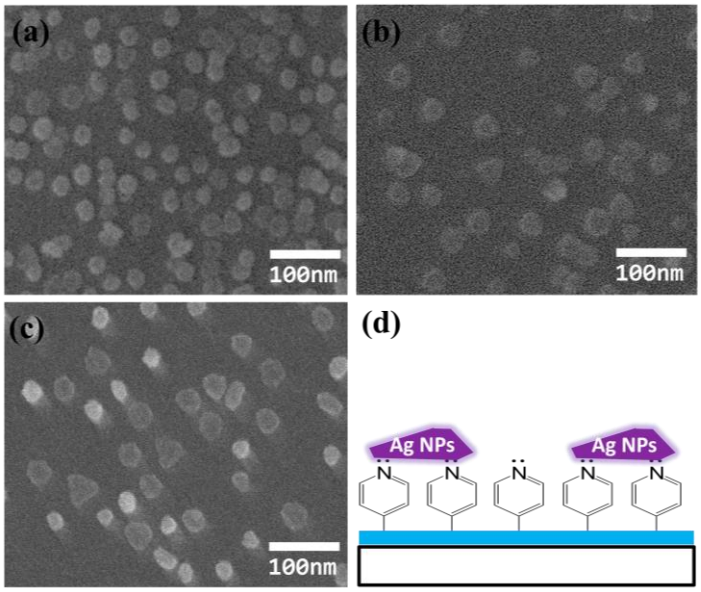

Figure 4. 2. SEM images of three kinds of Ag NPs immobilized on the surface of cover glass coated with P4VP and schematic image of Ag NPs immobilized on P4VP.

4. 3. 1. 2. TEM images of panchromatic Ag NPs

The TEM images of three kinds of Ag NPs are shown in Figure 4. 3. Their size was about 15 ± 4, 24 ± 3, and 30 ± 4 nm, respectively.

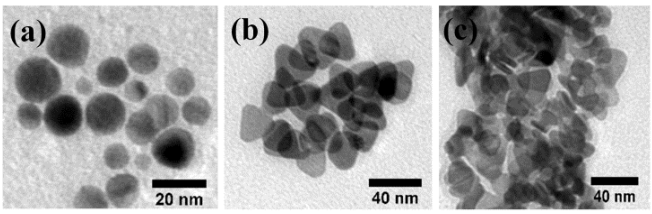

Figure 4. 3. (a-c) HR-TEM images of three kinds of Ag NPs. The size was about (a) 15 ± 4, (b) 24 ± 3, and (c) 30 ± 4 nm.

4. 3. 1. 3. UV-visible spectra of panchromatic Ag NPs

Figure 4. 4. shows the UV-visible extinction spectra of three kinds of Ag NPs, whose SEM images are shown in Figure 4. 2a-c, and those of their solutions. The extinction maximum of three kinds of Ag NPs immobilized was at 470, 540 and 620 nm, respectively. With increasing the size, the maximum wavelength was shifted to red and the extinction band became broad. The spectrum of each kind of Ag NPs immobilized was very similar to that measured in their solution. There was no significant shift in their extinction maximum wavelengths. Ag nanoplates fabricated by seed-mediated processes had two localized plasmon resonance peaks, due to the in-plane and out-of-plane resonances, near 520 and 400 nm, respectively.[153] The in-plane peak of Figure 4. 4a and b was much broader than that reported, while the out-of-plane peak was relatively much weaker and not distinct well. For a comparison, the absorption spectrum of N719 dye is shown in Figure 4. 4c. There were two visible bands at 398 and 538 nm. The absorption of N719 dye was relatively weak near 450 nm and longer wavelength region than 600 nm.

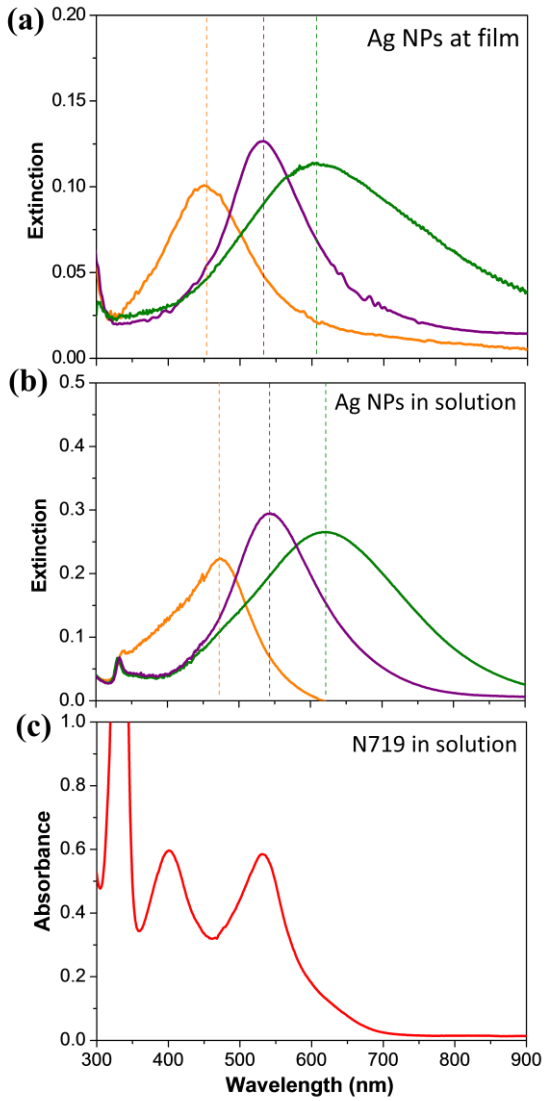

Figure 4. 4. UV-vis extinction spectra of three kinds of Ag NPs; (a) being immobilized on cover glass coated with P4VP, and (b) their solutions, and (c) UV-vis absorption spectrum of a N719 dye in ethanol solution.

4. 3. 2. Characterization of quasi-monolayer of Ag NPs

Figure 4. 5. shows the SEM images of the films immobilized with Ag NPs for 4, 8, and 12 h and UV-visible extinction spectra were measured by varying the immobilization time. Ag NPs were completely isolated when the immobilization time was relatively short. With increasing the immobilization time, the surface coverage of the films was increased. Although the extinction intensity was increased greatly with increasing the immobilization time, the extinction maximum wavelength was only slightly red shifted. It means that aggregation of Ag NPs does not take place greatly in the process of immobilization. It is expected that repulsion force of Ag NPs having the same surface charge prevented to Ag NPs on the film from aggregation.

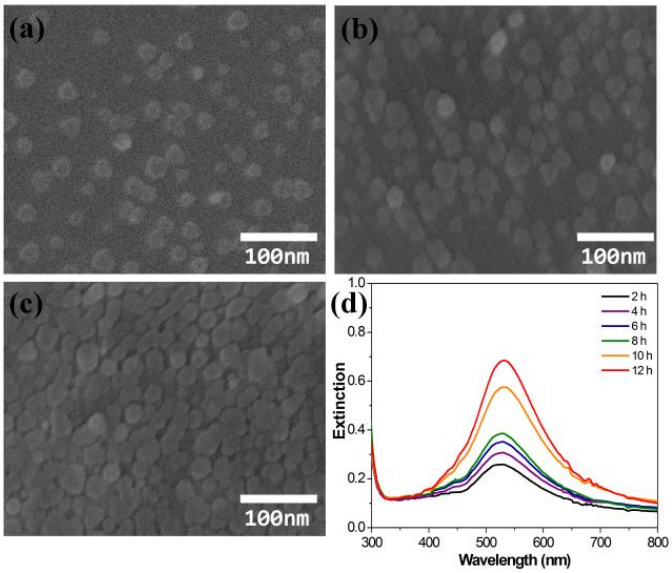

Figure 4. 5. SEM images of Ag NPs immobilized for 4, 8, and 12 h on the surface of cover glass coated with P4VP, and UV−vis extinction spectra measured by varying the immobilization time. The average size was about 24 ± 3 nm.

4. 3. 3. Characterization of panchromatic quasi-monolayer of Ag NPs

Figure 4. 6. shows the SEM images and extinction spectra of three kinds of Ag NPs immobilized on cover glass coated with P4VP in three steps. It should be mentioned that Ag NPs were not distinguished from TiO_2 NPs when they were immobilized on the film of TiO_2 NPs (see Figure 4. 7.). Therefore, we prepared the films immobilized with quasi-monolayer of panchromatic Ag NPs on the cover glass instead of FTO with TiO_2 NPs. When Ag NPs having λ_{max} of 540 nm in the solution phase were immobilized on the film for 4 h, the extinction maximum wavelength of the film was near 540 nm, which was almost the same as that of the Ag NPs in a solution phase (see the black colored spectrum of Figure 4. 6d). The surface coverage of the film was greater than 50%. When two kinds of Ag NPs having λ_{max} of 540 and 620 nm were immobilized on the film, in sequence, for 4 h each, the λ_{max} of the film was near 575 nm, and a shoulder on the low energy side was significantly increased (see the blue spectrum). When three kinds of Ag NPs having λ_{max} of 540, 620, and 470 nm were immobilized on the

film in sequence for 4 h each, the λ_{max} of the film was near 550 nm, and the shoulders on the high and low energy sides were significantly increased compared to the black spectrum (see the red spectrum).

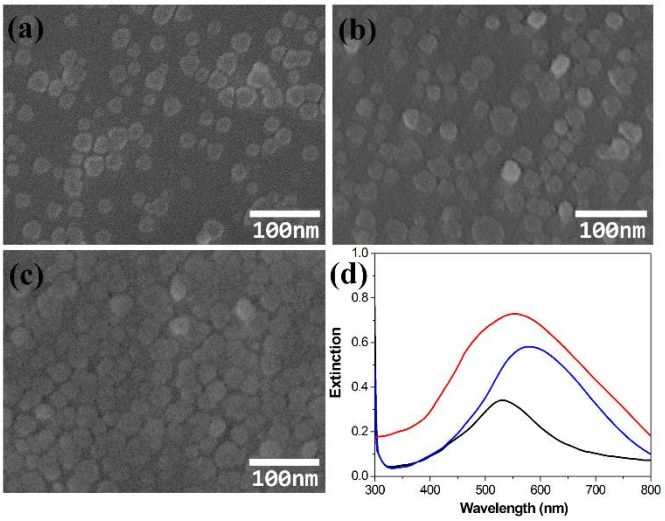

Figure 4. 6. The SEM images (a–c) and extinction spectra (d) of Ag NPs immobilized on cover glass coated with P4VP. (a) and black spectrum in (d) were referred to the film immobilized with Ag NPs having λ_{max} of 540 nm for 4 h. (b) and blue one in (d) were referred to the film immobilized with two kinds of Ag NPs having λ_{max} of 540 and 620 nm in sequence for 4 h each. (c) and red one in (d) were referred to the film immobilized with three kinds of Ag NPs having λ_{max} of 540, 620, and 470 nm in sequence for 4 h each.

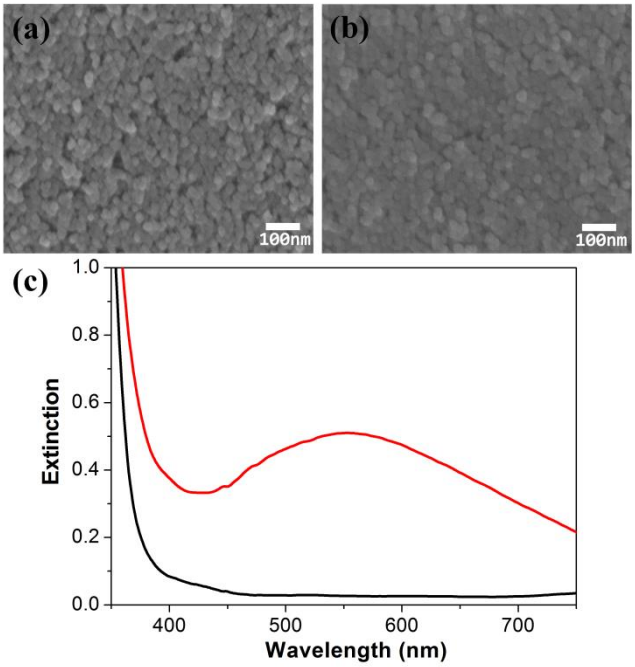

Figure 4. 7. SEM images of (a) the film of TiO_2 NPs and (b) panchromatic quasi-monolayer of Ag NPs deposited on the film of TiO_2 NPs, and (c) their extinction spectra. The black spectrum was measured from the sample for (a), while red one from the sample for (b).

4. 3. 4. Optimization of panchromatic quasi-monolayer of Ag NPs for DSSCs

Sequence of immobilization Ag NPs contributed to the efficiency of the DSSCs. The efficiency was highest when Ag NPs of 540 nm in λ_{max} was immobilized first, and then 620 nm, and finally 470 nm, than others (see Table 4. 1.). It could be related to the fact that the film immobilized with Ag NPs having λ_{max} of 540 nm first, 620 nm, and then 470 nm, showed the broadest extinction spectrum, and had the highest overlap with the spectrum of N719 dye among the films prepared by varying immobilization order of three kinds of Ag NPs (see Figure 4. 8.).

Table 4. 1. Dependence of the photovoltaic parameters of the DSSCs included a panchromatic quasi-monolayer of Ag NPs consisting of three kinds of Ag NPs, whose λ_{max} were 540, 620 and 470 nm, on the immobilization order of three kinds of Ag NPs. The immobilization time of each kind of Ag NPs was the same as 4 h.

Panchromatic Ag NPs	V_{oc} (V)	J_{sc} (mA/cm^2)	*ff*	η (%)
540-620-470	0.79 ± 0.03	19.27 ± 0.53	0.71 ± 0.03	11.0 ± 0.4
620-540-470	0.82 ± 0.01	18.68 ± 0.14	0.72± 0.02	10.9 ± 0.3
470-540-620	0.79 ± 0.01	18.34 ± 0.10	0.72± 0.02	10.4 ± 0.2

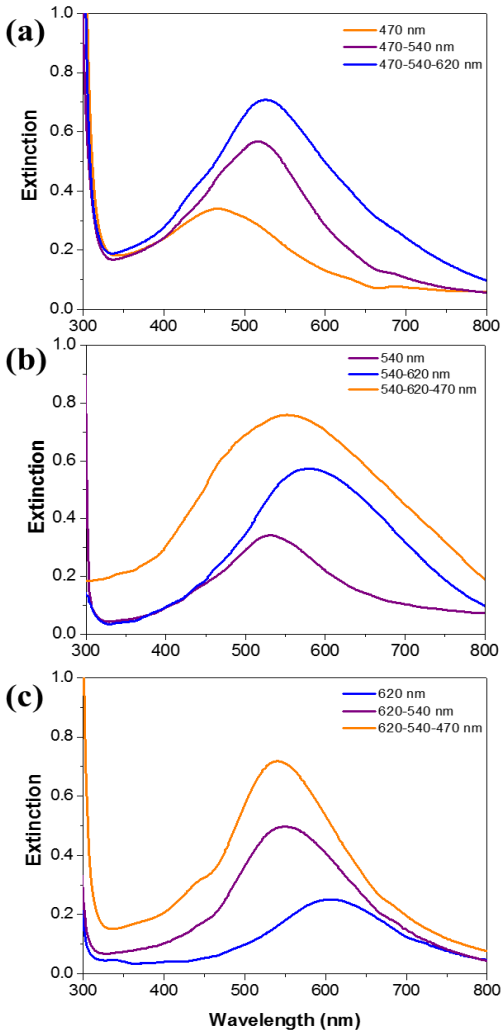

Figure 4. 8. Extinction spectra of Ag NPs immobilized on cover glass coated with P4VP. The legend represents the value of the λ_{max} of the plasmon resonance peak of the Ag NPs in the solution phase and the order of immobilization. For example, 470–540–620 nm means that Ag NPs immobilized Ag NPs having λ_{max} of 470 nm first, and then Ag NPs having λ_{max} of 540 nm, and then Ag NPs having λ_{max} of 620 nm.

The efficiency of the DSSCs included a quasi-monolayer consisting of three kinds of Ag NPs was highest when the immobilization time of each type of Ag NPs was 4 h (12 h in total) (see Table 4. 2.). Also, the efficiency was slightly affected by the coating times of P4VP before and after immobilization of Ag NPs (see Tables 4. 3-7). It was highest when the coating time of P4VP before and after immobilization of Ag NPs was 1.5 and 1 h, respectively.

Table 4. 2. Dependence of the photovoltaic parameters of the DSSCs included a panchromatic quasi-monolayer of Ag NPs consisting of three kinds of Ag NPs, whose λ_{max} were 540, 620 and 470 nm, on the immobilization time of Ag NPs. Ag NPs whose λ_{max} was 540 nm was immobilized first, and then those of 620 nm, and then those of 470 nm. The immobilization time of each kind of Ag NPs was the same.

Panchromatic Ag NPs	V_{oc} (V)	J_{sc} (mA/cm^2)	*ff*	η (%)
reference	0.78 ± 0.02	16.20 ± 0.41	0.70 ± 0.03	8.9 ± 0.3
3 h	0.78 ± 0.01	16.42 ± 0.11	0.70 ± 0.01	9.1 ± 0.2
6 h	0.77 ± 0.02	17.65 ± 0.31	0.69 ± 0.02	9.7 ± 0.2
9 h	0.79 ± 0.02	18.11 ± 0.22	0.70 ± 0.02	10.3 ± 0.3
12 h	0.79 ± 0.03	19.27 ± 0.53	0.71 ± 0.03	11.0 ± 0.4
15 h	0.79 ± 0.02	17.55 ± 0.32	0.70 ± 0.03	10.1 ± 0.2

Table 4. 3. Dependence of the photovoltaic parameters of the DSSCs included a quasi-monolayer of Ag NPs, whose λ_{max} was at 470 nm, on the coating time of P4VP. P4VP was coated on the surface of the TiO_2 film by dipping FTO glass deposited a blocking layer and TiO_2 film in a P4VP solution.

470 nm Ag NPs	V_{oc} (V)	J_{sc} (mA/cm^2)	*ff*	η (%)
reference	0.78 ± 0.02	16.20 ± 0.41	0.70 ± 0.03	8.9 ± 0.3
0.5 h	0.80 ± 0.02	16.11 ± 0.21	0.70 ± 0.02	9.0 ± 0.2
1 h	0.81 ± 0.02	16.53 ± 0.14	0.70 ± 0.01	9.4 ± 0.2
1.5 h	0.81 ± 0.03	17.10 ± 0.11	0.69 ± 0.01	9.6 ± 0.1
2 h	0.79 ± 0.02	17.01 ± 0.08	0.70 ± 0.02	9.4 ± 0.1
3 h	0.81 ± 0.03	15.96 ± 0.33	0.71 ± 0.02	9.2 ± 0.3

Table 4. 4. Dependence of the photovoltaic parameters of the DSSCs included a quasi-monolayer of Ag NPs, whose λ_{max} was at 540 nm, on the coating time of P4VP.

540 nm Ag NPs	V_{oc} (V)	J_{sc} (mA/cm^2)	*ff*	(%)
reference	0.78 ± 0.02	16.20 ± 0.41	0.70 ± 0.03	8.9 ± 0.3
0.5 h	0.80 ± 0.01	17.00 ± 0.18	0.69 ± 0.02	9.4 ± 0.1
1 h	0.79 ± 0.02	17.47 ± 0.14	0.71 ± 0.01	9.8 ± 0.2
1.5 h	0.80 ± 0.01	18.68 ± 0.32	0.72 ± 0.01	10.7 ± 0.1
2 h	0.81 ± 0.01	18.11 ± 0.20	0.71 ± 0.01	10.4 ± 0.2
3 h	0.81 ± 0.02	16.27 ± 0.13	0.70 ± 0.01	9.2 ± 0.2

Table 4. 5. Dependence of the photovoltaic parameters of the DSSCs included a quasi-monolayer of Ag NPs, whose λ_{max} was at 620 nm, on the coating time of P4VP.

620 nm Ag NPs	V_{oc} (V)	J_{sc} (mA/cm^2)	*ff*	η (%)
reference	0.78 ± 0.02	16.20 ± 0.41	0.70 ± 0.03	8.9 ± 0.3
0.5 h	0.79 ± 0.02	16.58 ± 0.11	0.72 ± 0.02	9.4 ± 0.1
1 h	0.79 ± 0.02	17.21 ± 0.24	0.71 ± 0.01	9.6 ± 0.1
1.5 h	0.80 ± 0.01	17.34 ± 0.43	0.70 ± 0.01	9.7 ± 0.2
2 h	0.79 ± 0.01	18.59 ± 0.12	0.70 ± 0.02	10.2 ± 0.2
3 h	0.79 ± 0.01	17.30 ± 0.33	0.68 ± 0.03	9.2 ± 0.2

Table 4. 6. Dependence of the photovoltaic parameters of the DSSCs included a panchromatic quasi-monolayer of Ag NPs consisting of three kinds of Ag NPs, whose λ_{max} were 540, 620 and 470 nm, on the first coating time of P4VP. The second coting time was the same as 1 h.

Panchromatic Ag NPs	V_{oc} (V)	J_{sc} (mA/cm^2)	*ff*	η (%)
reference	0.78 ± 0.02	16.20 ± 0.41	0.70 ± 0.03	8.9 ± 0.3
0.5 h	0.79 ± 0.03	16.42 ± 0.42	0.71 ± 0.02	9.3 ± 0.3
1 h	0.79 ± 0.02	17.59 ± 0.23	0.70 ± 0.02	9.7 ± 0.2
1.5 h	0.81 ± 0.02	18.99 ± 0.30	0.72 ± 0.02	10.9 ± 0.3
2 h	0.80 ± 0.02	18.38 ± 0.11	0.72 ± 0.01	10.6 ± 0.2
3 h	0.80 ± 0.02	17.82 ± 0.33	0.71 ± 0.01	10.1 ± 0.2

Table 4. 7. Dependence of the photovoltaic parameters of the DSSCs included a panchromatic quasi-monolayer of Ag NPs consisting of three kinds of Ag NPs, whose λ_{max} were 540, 620 and 470 nm, on the second coating time of P4VP. The first coating time of P4VP was the same as 1.5 h for all the samples.

Panchromatic Ag NPs	V_{oc} (V)	J_{sc} (mA/cm^2)	*ff*	η (%)
reference	0.78 ± 0.02	16.20 ± 0.41	0.70 ± 0.03	8.9 ± 0.3
0.5 h	0.80 ± 0.01	18.95 ± 0.33	0.71 ± 0.01	10.8 ± 0.1
1 h	0.79 ± 0.03	19.27 ± 0.53	0.71 ± 0.03	11.0 ± 0.4
1.5 h	0.81 ± 0.02	19.00 ± 0.11	0.72 ± 0.02	11.0 ± 0.1
2 h	0.80 ± 0.03	18.95 ± 0.23	0.70 ± 0.02	10.6 ± 0.3
3 h	0.82 ± 0.01	18.63 ± 0.12	0.70 ± 0.02	10.7 ± 0.2

4. 3. 5. Photovoltaic properties of panchromatic DSSCs

To prevent corrosion of Ag NPs, TIP was treated. TIP treatment is known to be an efficient method to prevent silver corrosion and electron leaking from Ag NPs. Jeong *et al.* have studied the effect of treating Ag NPs with TIP in detail and proved that TIP treatment sufficiently can prevent silver corrosion and electron leaking from metal NPs.[89]

The thickness of the photoactive TiO_2 film itself was about 4.5 μm in the DSSCs included a quasi-monolayer of Ag NPs, while 9 μm in the conventional DSSCs. With including the scattering layer, the thickness of the photoactive TiO_2 film was about 13 μm for the DSSCs included a quasi-monolayer of Ag NPs, while 17 μm for the conventional DSSCs. It should be mentioned that the morphology of Ag nanoplates could be modified by sintering at 450 °C. When Ag nanoplates are sintered at a relatively high temperature, they will be changed ultimately to spherical silver to minimize their surface area. It is known that the LSPR band of spherical Ag NPs centers at near 400 nm.[154] Therefore, a blue shift of the LSPR band of our Ag

nanoplates could take place when the morphology was modified by sintering. However, Ag nanoplates included in our DSSCs existed between the photoactive and scattering layers. It means that Ag nanoplates were surrounded with a large amount of TiO_2 NPs. Also, the surface of Ag nanoplates was coated with TiO_2 to prevent corrosion. Therefore, the morphology change of Ag nanoplates by sintering could be reduced greatly under our conditions. We tried to observe the blue shift of Ag nanoplates surrounded by TiO_2 NPs by sintering. However, we could not observe the LSPR band of Ag nanoplates itself due to a strong background of TiO_2.

In Figure 4. 9a, the photocurrent density-voltage ($J-V$) curves from the DSSCs based on films of TiO_2 NPs, with and without being constructed a quasi-monolayer of Ag NPs were measured in air mass 1.5 sunlight. The photovoltaic parameters are summarized in Table 4. 8. The total immobilization time of single kind or three kinds of Ag NPs was the same as 12 h. For a panchromatic quasi-monolayer, Ag NPs with λ_{max} at 540 nm was immobilized first, and then those at 620 nm, and then those at 470 nm. For the DSSC not included a monolayer of Ag NPs, the short-circuit current density (J_{sc}), open- circuit voltage (V_{oc}), fill factor (ff), and overall conversion efficiency (η)

were 16.23 ± 0.42 mA/cm^2, 0.80 ± 0.02 V, 0.69 ± 0.01, and 8.9 ± 0.3%, respectively. Among the DSSCs included single-type Ag NPs as a quasi-monolayer, one included Ag NPs whose λ_{max} was 540 nm shows the highest efficiency. The photovoltaic parameters were 18.11 ± 0.55 mA/cm^2, 0.79 ± 0.01 V, 0.70 ± 0.02, and 10.5 ± 0.3%, respectively. For the DSSC included a quasi-monolayer consisting of three kinds of Ag NPs, the photovoltaic parameters were 19.27 ± 0.53 mA/cm^2, 0.79 ± 0.03 V, 0.71 ± 0.03, and 11.0 ± 0.4%, respectively. It was concluded that the DSSCs included a quasi-monolayer of three kinds of Ag NPs were more effective for light harvesting than the DSSCs included that of single kind of Ag NPs or conventional DSSCs. The open-circuit voltages and fill factor were not changed significantly. The efficiency enhancement by inclusion a quasi-monolayer of Ag NPs was caused mainly by the increase in photocurrent density. The efficiency of 11.4% achieved here is the highest published so far for plasmonic DSSCs.[101, 157]

The incident photon-to-current conversion efficiency (IPCE) spectra measured from the five DSSCs are shown in Figure 4. 9b. By construction of a quasi-monolayer of Ag NPs, IPCE over the wavelength range 400 to 700 nm was enhanced,

exhibiting the maximum wavelength of near 550 nm which is closely associated with N719 dye absorption. The DSSC included a quasi-monolayer of three kinds of Ag NPs showed highest intensity over the whole range of wavelengths (400 - 700 nm). The relative intensity of IPCE spectra of the DSSCs included a quasi-monolayer of Ag NPs was closely related to the degree of the spectral overlap between the extinction bands of Ag NPs included in fabrication of DSSCs and the absorption bands of N719 dye. It was clearly proved in the IPCE improvement factor spectra shown in Figure 4. 9c. The factor was calculated by the following equation: $\Delta IPCE(\lambda)/IPCE(\lambda)\% = [(IPCE_{DSSC\ included\ a\ Ag\ NPs'\ layer(\lambda)} - IPCE_{DSSC\ not\ included\ a\ Ag\ NPs'\ layer(\lambda)}) /IPCE_{DSSC\ not\ included\ a\ Ag\ NPs'\ layer(\lambda)}] \times 100$. In the IPCE improvement factor spectra, the intensity of the DSSC included a quasi-monolayer of Ag NPs whose λ_{max} is 620 nm is stronger in the low energy region but weaker in high energy region than that of the DSSC included a quasi-monolayer of Ag NPs whose λ_{max} is 470 nm.

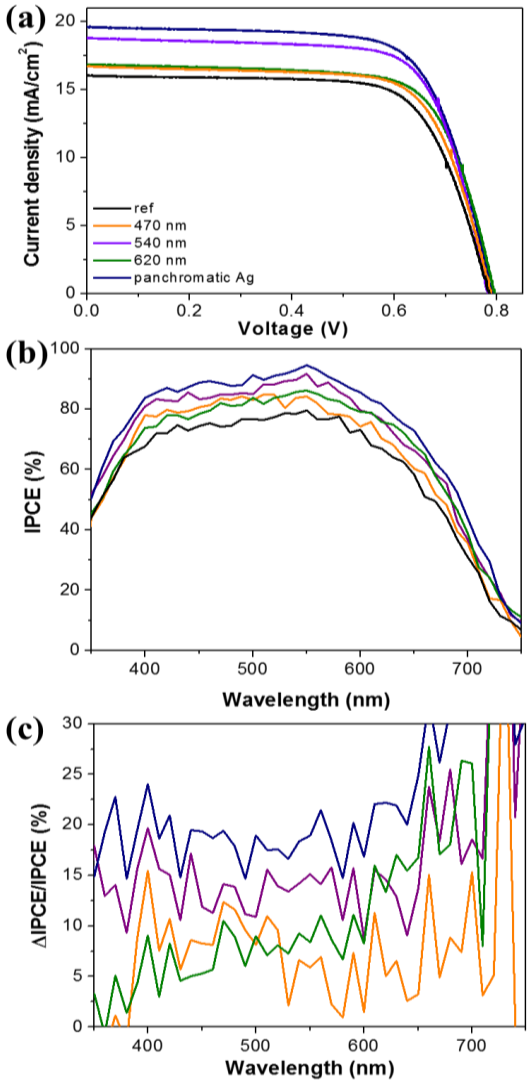

Figure 4. 9. (a) Photocurrent density–voltage ($J-V$) curves and (b) IPCE spectra measured from the DSSCs based on films of TiO_2 NPs, with and without being constructed a quasi-monolayer of Ag NPs between the layer of TiO_2 NPs and the scattering layer, and (c) the relative IPCE improvement factor [ΔIPCE(λ)/IPCE(λ)%] spectra.

Table 4. 8. Photovoltaic parameters measured from the DSSCs based on films of TiO_2 NPs, with and without being constructed a quasi-monolayer of Ag NPs between the layer of TiO_2 NPs and the scattering layer.

	V_{oc} (V)	J_{sc} (mA/cm^2)	*ff* (%)	η (%)
470 nm	0.80 ± 0.02	16.23 ± 0.42	0.69 ± 0.01	9.3 ± 0.2
540 nm	0.79 ± 0.01	18.11 ± 0.55	0.70 ± 0.02	10.5 ± 0.3
620 nm	0.78 ± 0.01	16.98 ± 0.48	0.71 ± 0.02	9.7 ± 0.2
panchromatic	0.79 ± 0.03	19.27 ± 0.53	0.71 ± 0.03	11.0 ± 0.4
reference	0.78 ± 0.02	16.20 ± 0.41	0.70 ± 0.03	8.9 ± 0.3

4. 3. 6. EIS of panchromatic DSSCs

Figure 4. 10. shows the characteristic electrochemical impedance spectra (EIS) for the DSSCs based on TiO_2 film and TiO_2/Ag nanoplate film. They were recorded in the frequency range of 0.1 Hz to 100 KHz. Each spectrum contains well-defined three semicircles. The hemisphere in the high-frequency region is assign to the parallel combination of the resistance and capacitance at the Pt-FTO/electrolyte and to the interface between FTO and TiO_2 layers, while those in the intermediate and low-frequency regions offer information on the resistance and capacitance at the TiO_2/electrolyte interface and the Nernst diffusion of the electrolyte, respectively.[156]

Two spectra were almost the same on the Nyquist plot, while they showed a little difference at low and high frequency region on the Bode plot. In both spectra, the position of the middle frequency (f_{mid}) peak was the same as 21.23 Hz. The value of the middle frequency (f_{mid}) is related to the inverse of the electron lifetime (τ) as follows: $\tau_{eff} = 1/(2\pi f_{mid})$.[84,158] The calculated electron lifetime was 7.49 ms for the DSSCs based on the photoactive film of TiO_2 NPs with and without including a

panchromatic quasi-monolayer of Ag NPs between the layer of TiO_2 NPs and the scattering layer, respectively. Also, the electron lifetime is related to the effective carrier diffusion length (L_n) as follows: $L_n^2 = D_{eff} \times \tau$, where D_{eff} is the effective electron diffusion coefficient and τ is the electron lifetime. Based on the Bisquert model,[159] D_{eff} is described as $D_{eff} = (R_k/R_w)L^2k_{eff}$.[84,158] Where R_w, R_k, L, and k_{eff} represent the resistance of electron transport in the photoanode, the resistance of charge transfer related to recombination, the thickness of the photoanode, and the constant of effective rate for recombination, respectively.

The values of these parameters are obtained from the semicircle of middle frequency in Nyquist and Bode plots. R_w is estimated from diameter of the middle semicircle in the Nyquist plot shown in Figure 4. 10a, and R_k is determined from the diameter of the middle semicircle in the Nyquist plot obtained under dark conditions (Figure 4. 11.). k_{eff} is obtained from the maximum peak frequency obtained from the Bode plot in Figure 4. 10b.[84] The calculated values are summarized in Table 4. 9. The calculated value of L_n for the DSSCs based on the photoactive film of TiO_2 NPs with and without including a panchromatic quasi-monolayer of Ag NPs was 7.10 and 7.98

μm, respectively. The results indicate that there is no significant difference in both the electron lifetime (τ) and effective carrier diffusion length (L_n).

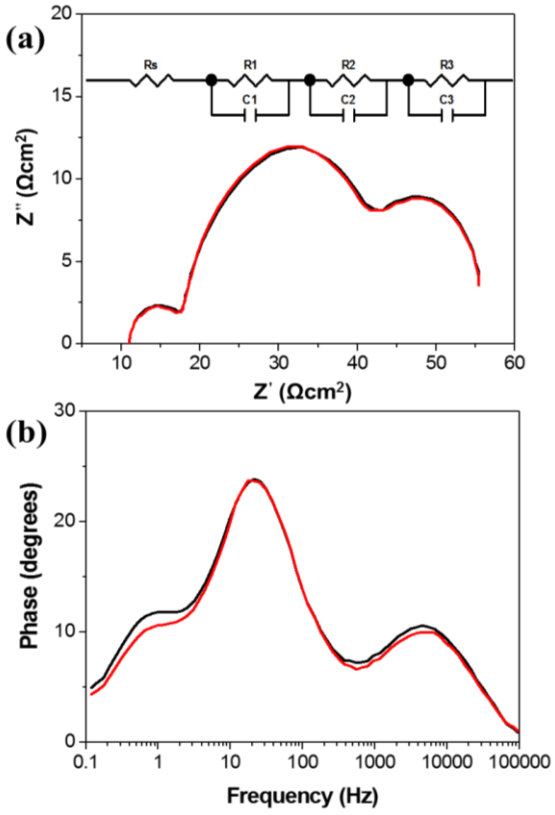

Figure 4. 10. Electrochemical impedance spectra of the DSSCs based on the photoactive film of TiO_2 NPs with (red) and without (black) including a panchromatic quasi-monolayer of Ag NPs between the layer of TiO_2 NPs and the scattering layer; (a) Nyquist plot and (b) Bode plot. The thickness of both photoactive films of TiO_2 NPs was the same as 4.5 μm.

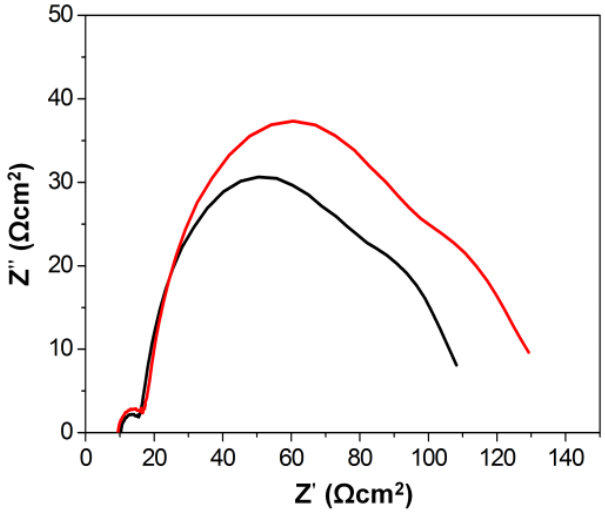

Figure 4. 11. Nyquist plot of the electrochemical impedance spectra, measured under dark conditions, of the DSSCs based on the photoactive film of TiO_2 NPs with (red) and without (black) including a panchromatic quasi-monolayer of Ag NPs between the layer of TiO_2 NPs and the scattering layer.

Table 4. 9. Parameters determined by EIS.

DSSCs based on TiO_2 NPs	R_k (Ωcm^2)	R_w (Ωcm^2)	R_k/R_w (Ωcm^2)	τ_{eff} (ms)	K_{eff} (s^{-1})	D_{eff} ($cm^2 s^{-1}$)	L (μm)	L_n (μm)
without	61.14	24.54	2.49	7.49	21.23	1.07×10^{-5}	4.5	7.10
With including a panchromatic layer of Ag NPs	76.14	24.11	3.15	7.49	21.23	1.35×10^{-5}	4.5	7.98

By construction of a panchromatic quasi-monolayer of Ag NPs between the photoactive and scattering layers and reducing the thickness of the photoactive layer, the power conversion efficiency has been enhanced up to 11.4%, mainly by increasing the photocurrent density. The efficiency of 11.4% achieved here is the highest published so far for plasmonic DSSCs.[101] The photocurrent density might be increased by enhancement of light absorption and electron transfer yield to the electrode.

Enhancement of light absorption could came from taking place on or near surface of metal NPs by LSPRs. The LSPRs decay either radiatively or into (quasi) particles such as electron-hole (e-h) pairs.[160] The former decay path gives rise to the dramatic electromagnetic field enhancements, for instance, as in surface-enhanced Raman spectroscopy. By the latter decay path, the light absorption of dye molecules adsorbed on or near Ag NPs is enhanced.[161] Absorption of dye that is not adsorbed on or near the surface of Ag NPs on the photoactive layer could be enhanced by the scattered light, since the quasi-monolayer of Ag NPs scattered light strongly.

Normally, absorption of photoactive layer will be also enhanced with increasing thickness of TiO_2 NPs layer where dye molecules are adsorbed, because of increasing the number

of dye molecules. In case of plasmonic DSSCs, the plasmon enhanced absorption takes place only to the molecules adsorbed on or near the surface of Ag NPs, and therefore it is not affected directly by the thickness of the photoactive layer. However, in our DSSCs constructed a panchromatic quasi-monolayer, the plasmon enhanced absorption may be critically affected by the location of quasi-monolayer of Ag NPs. The intensity of light reached to the quasi-monolayer of Ag NPs might be decreased with increasing the thickness of the photoactive layer.

Increasing thickness of the photoactive layer affected to the absorption of the scattered light as two opposite factors in the DSSCs constructed a panchromatic quasi-monolayer. As negative factor, the intensity of light reached to the quasi-monolayer decreases with increasing the thickness of the photoactive layer, and intensity of scattered light also decreases. However, as the positive factor, the number of dye molecules, which could absorb the scattered light, is increased with increasing the thickness of the photoactive layer. Consequently, the dye absorption could be affected by the thickness of the photoactive layer existing in front of a panchromatic quasi-monolayer.

Actually, the efficiency of the DSSCs constructed a panchromatic quasi-monolayer was affected by the thickness of the photoactive layer. When the thickness of the photoactive layer was 3.0, 4.5, and 9.0 μm, the efficiency was 9.99, 11.4, and 10.7%, respectively. A more precise optimization of the thickness should be studied in detail. At least, a high efficiency was achieved by construction of a panchromatic quasi-monolayer of Ag NPs on the surface of photoactive layer whose thickness was 4.5 μm. This thickness is much thinner than the optimum length (about 9 μm) for the DSSCs based only TiO_2 NPs.[1] Therefore, the high efficiency might be contributed partially by the reduced thickness of the photoactive film.

It is not a difficult process to construct a quasi-monolayer of Ag NPs between the photoactive layer and the scattering layer. The optical property of the quasi-monolayer of Ag NPs is not critically affected by the fabrication technique, since most Ag NPs are immobilized without aggregation because of repulsion of Ag NPs having same surface charge. Also, the panchromatic property is uniformly appeared on the whole area of a quasi-monolayer. This general method to construct a quasi-monolayer of Ag NPs could be used in fabrication of other types of solar cells.

4. 4. Conclusion

We have developed a quasi-monolayer of Ag NPs, without aggregation, whose extinction takes place in all the visible range and applied this technique to construct dye-sensitized solar cells (DSSCs). Three kinds of Ag NPs, whose λ_{max} were at 540, 620 and 470 nm, were immobilized, in sequence, on a photoactive film of TiO_2 NPs coated with P4VP, and then coated P4VP again, and then deposited a scattering layer. The efficiency of the DSSCs included a quasi-monolayer of Ag NPs between the layer of TiO_2 NPs and the scattering layer was enhanced up to 11.4%. The efficiency of 11.4% achieved here is the highest published so far for plasmonic DSSCs. A high efficiency was affected by the increased light absorption and electron transfer yield. Our general and simple method could be used in fabrication of other types of solar cells.

Chapter 5

Nanostructure-Based Graphene Flake Counter Electrode for Dye-Sensitized Solar Cells

5. 1. Concept

A nanostructure-based graphene flake counter electrode for dye-sensitized solar cells (DSSCs) was fabricated by immobilization of gold nanoparticles (NPs) on fluorine-doped tin oxide (FTO) glass and the deposition of a thin layer of graphene flakes. The graphene flakes, fabricated using a thermal plasma jet system, were very thin and pure and had good crystallinity. Although, their average size was larger than 100 nm, they were well dispersed in some solvents by sonication. Their relatively large size and good crystallinity resulted in good conductivity, and their good dispersibility allowed us to fabricate relatively uniform films. The efficiency of the DSSC with a graphene flake/Au NP/FTO counter electrode was as much as 9.71%, which is higher than that with a conventional Pt/FTO (9.02%) or graphene flake/FTO (8.91%) counter electrode. Using cyclic voltammograms and electrochemical impedance spectroscopy and by measuring the incident photo-conversion efficiency, we proved that by the localized surface plasmon resonance effect of the Au NPs included between the graphene flakes and FTO, the catalytic

activity of the graphene flakes improved and the charge-transfer resistance at the electrode/electrolyte interface decreased.

5. 2. Fabrication of hybrid counter electrodes

5. 2. 1. Immobilization of Au NPs

The Au NPs were immobilized on the FTO glass following a previously reported method.[104,154] The FTO glass with a predrilled hole was cleaned and then dipped into a poly(4-vinylpyridine) (P4VP) solution (0.3 g of P4VP was dissolved in 100 mL of ethanol) for 10 s to coat it with P4VP. After coating, the glass was washed thoroughly with deionized water and ethanol and then put in a vial containing 2 mL of the Au NP solution for 3 h to immobilize the Au NPs onto the surface of the P4VP-coated glass. The glass was washed again and then sintered at 350 ℃ for 1 h in air to remove P4VP.

5. 2. 2. Preparation of counter electrodes

Graphene flakes were deposited onto clean FTO glass or on the arrays of Au NPs immobilized on FTO glass using assembling and transferring techniques.[162,163] 0.5 mL of the graphene flake suspension was mixed with 40 mL of water, and then 4 mL of ethyl acetate (EA) was poured onto the surface of the mixture solution. In this case, self-assembled graphene films formed on the surface within a few minutes. The self-assembled graphene film was transferred onto arrays of Au NPs immobilized on FTO glass or clean FTO glass and then dried at 100 °C for 10 min to remove any residual solvent. The transferring and drying were repeated approximately six times, and then the films were annealed at 350 °C for 1 h. The conventional Pt counter electrode was prepared by dropping the Pt solution onto the FTO glass and then sintering. Figure 5. 1 shows photographic images of the hybrid, graphene flake, and conventional Pt counter electrodes. A schematic of the fabrication of a hybrid counter electrode is shown in Figure 5. 2.

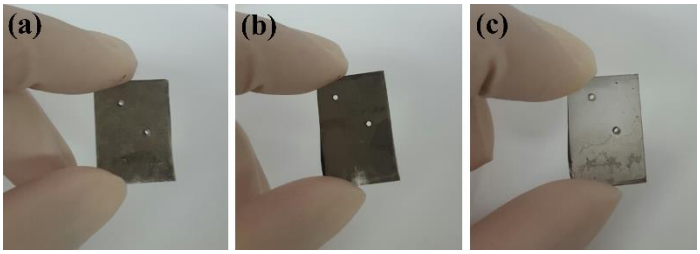

Figure 5. 1. Photographic images of (a) hybrid, (b) graphene flakes and (c) conventional Pt counter electrodes.

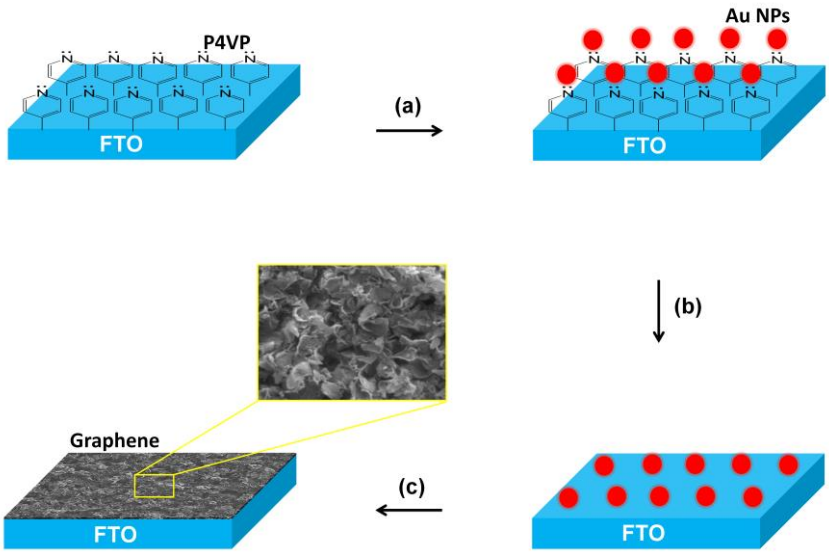

Figure 5. 2. Scheme for construction of a nanostructure-based graphene flake counter electrode: (a) immobilization of Au NPs on FTO coated with P4VP, (b) sintering at 350 °C to remove P4VP, and (c) deposition of graphene flakes.

5. 3. Results and discussion

5. 3. 1. Characterization of graphene flakes

5. 3. 1. 1. SEM images of graphene flakes

Figure 5. 3 shows low- and high-magnification SEM images of raw carbon soot, without any treatment, produced using the thermal plasma jet system.[149,163] Ethylene gas (500 sccm) was injected as a carbon source. Carbon soot is very pure, consisting of small graphene flakes whose average size is larger than 100 nm. Graphene flakes are very thin, and each graphene flake is transparent. When the injection rate of ethylene gas was 500 sccm, the production rate based on the amount of graphene flakes collected in the chamber was approximately 1.5 g/h. The carbon soot was well dispersed by sonication in organic solvents such as ethanol, cyclohexane, and DMF, whereas only a very small portion of the graphene flakes was dispersed in water, even by sonication. The dispersed solutions were very stable for several months.

During the fabrication of the graphene flakes, high-purity

ethylene and argon gases were injected into the system as a carbon source and plasma gas, respectively. Therefore, no oxygen was included in the fabrication process. Actually, in the EDS spectrum of the graphene flakes that were not exposed to air, no oxygen peak was observed (see Figure 5. 4a). This means that our pristine graphene flakes contained no oxygen. However, an oxygen peak was observed for the graphene flakes exposed to air (see Figure 5. 4b). This means that the graphene flakes contained oxygen when exposed to air or oxygen.

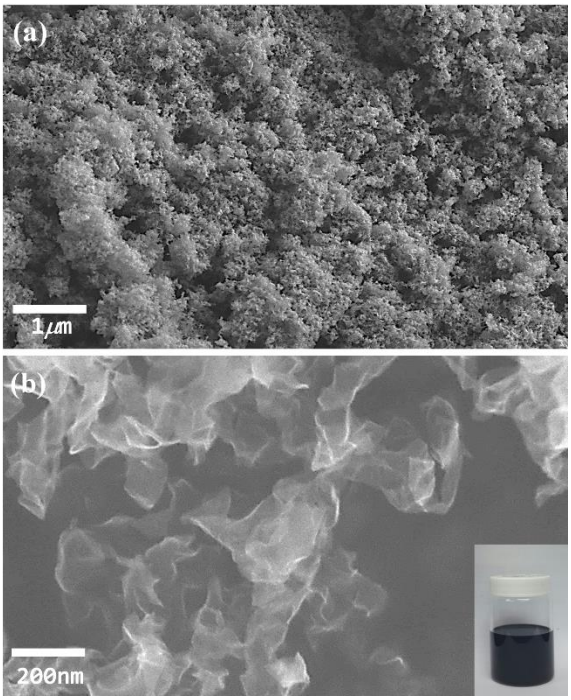

Figure 5. 3. Low- and high-magnification SEM images of pristine graphene flakes. The inset shows a photograph of the dispersed graphene flakes in DMF.

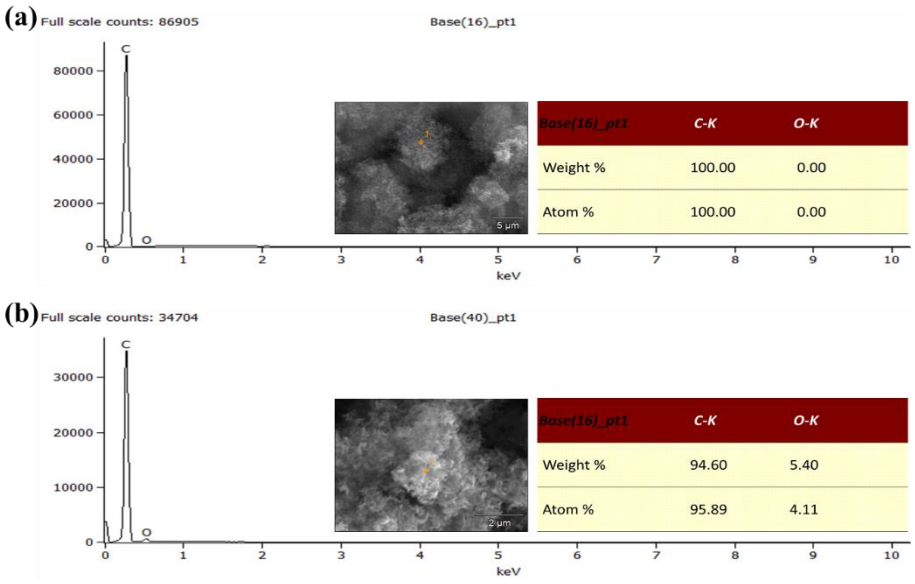

Figure 5. 4. The EDS spectrum and SEM image of graphene flakes that (a) were not exposed to air and (b) were exposed to air.

5. 3. 1. 2. XPS of graphene flakes

Figure 5. 5 shows the XPS C1s and Raman spectra of the graphene flakes used in the fabrication of the counter electrodes. The XPS C1s spectrum could be deconvoluted into four components, corresponding to sp^2 (C=C) at a binding energy of 284.8 eV, sp^3 (C–C and C–H) at 285.9 eV, C–OH at 286.5 eV, and O=C–OH at 288.5 eV. The predominant peak at 284.8 eV indicates that the graphene flakes consisted of mostly sp^2−bonded carbons. Although their intensities are relatively weak, observation of the peaks derived from the C–OH and O=C–OH groups means that the XPS sample contained oxygen. A small percent of oxygen might have been included in the preparation or loading process of the XPS sample because our pristine graphene flakes contained no oxygen. In the preparation of the XPS sample, graphene flakes were dispersed in ethanol by sonication under atmosphere. Also, the XPS sample was briefly exposed to air during loading into the XPS chamber.

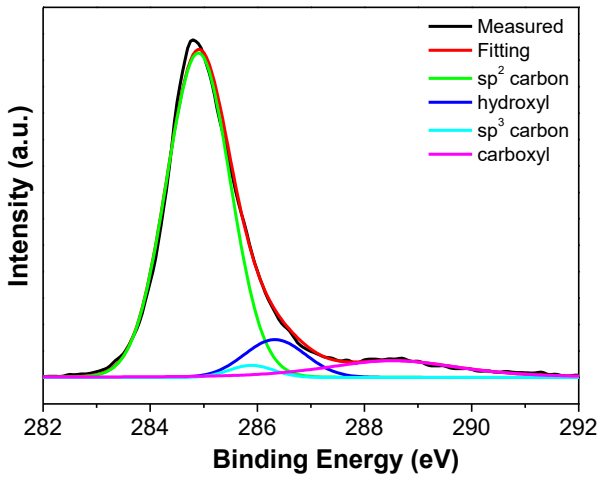

Figure 5. 5. XRD of graphene flakes used in the fabrication of counter electrodes.

5. 3. 1. 3. Raman spectrum of graphene flakes

In the Raman spectrum shown in Figure 5. 6, there are three typical graphene peaks: the D peak near 1360 cm^{-1}, the G peak near 1594 cm^{-1}, and the 2D peak near 2703 cm^{-1}. The G peak has E_{2g} symmetry that is involved in the in-plane bond-stretching motion of pairs of C sp^2 atoms, and the 2D peak is a second-order two-phonon mode. The D peak is the breathing mode of A_{1g} symmetry that is known to be due to the presence of structural disorders in graphene sheets.[164] The D peak is not Raman-active for pristine graphene or highly oriented pyrolytic graphite (HOPG), but it can be observed where symmetry is broken by edges or in samples with high defect densities.[149,163,164]

Generally, the D/G intensity ratio can be used to determine the crystallinity of graphene; the lower the ratio, the better the crystallinity. In the Raman spectrum, the intensity of the D peak is approximately one-third the intensity of the G peak. However, the intensity ratio does not simply represent the crystallinity of the graphene flakes because the edges of graphene sheets are always seen as defects. Although the size of the graphene flakes was larger than 100 nm, the ratio of

edges was still very large as compared to that of large-size graphene. Nevertheless, the predominantly strong peak derived from sp^2 carbons in the XPS spectrum may indicate that the graphene flakes had good crystallinity. The graphene flakes were too large to have a quantum confinement effect,[165] and degradation of their electrical conductivity was minimal. Therefore, it is concluded that the graphene flakes had good conductivity.

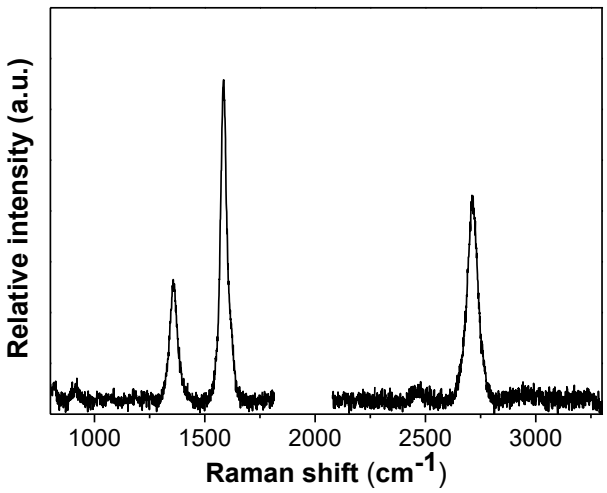

Figure 5. 6. Raman spectra of graphene flakes used in the fabrication of counter electrodes.

5. 3. 2. Morphologies of hybrid counter electrode

Figure 5. 7 shows SEM images of Au NPs immobilized on FTO glass coated with P4VP and the surfaces of the three types of counter electrodes. It is well known that metal NPs are immobilized on P4VP by an attractive interaction between the lone pair of electrons on the nitrogen atom of the pyridine ring and the metal NPs.[154] Most Au NPs are isolated but some are aggregated. Aggregation might have occurred by sintering because before sintering almost all the Au NPs were immobilized individually on the surface of P4VP due to repulsion between Au NPs having the same charge (see Figure 5. 8). Since P4VP is an insulator, it should be removed from the surface of the electrode.

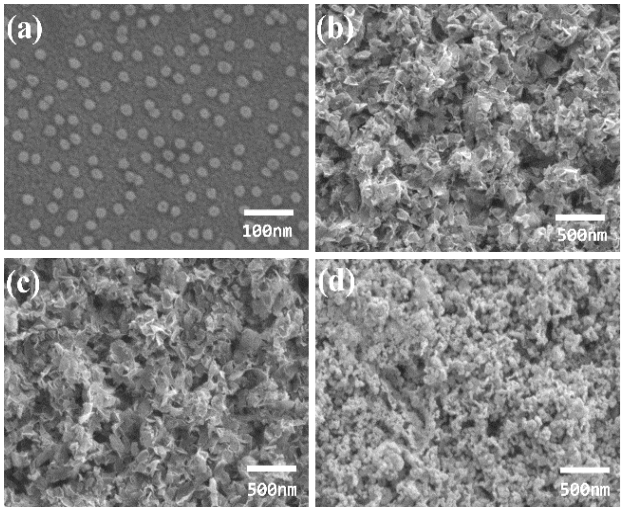

Figure 5. 7. SEM images of (a) Au NPs immobilized on FTO glass after sintering and the surfaces of (b) the hybrid, (c) graphene flake and (d) conventional Pt counter electrodes.

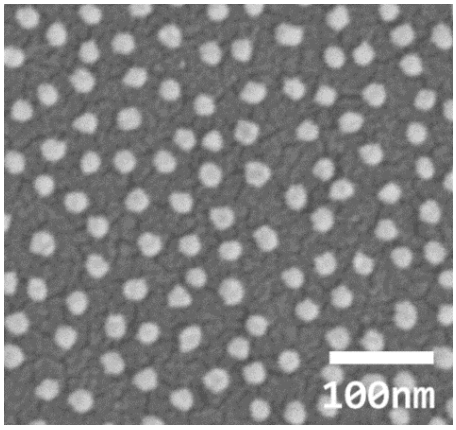

Figure 5. 8. SEM image of Au NPs immobilized on FTO glass before sintering.

The average size of the Au NPs was approximately 17 nm (see Figure 5. 9.). The surfaces of all three types of counter electrodes were very rough, indicating that they had high surface areas. The graphene flake and hybrid counter electrodes showed a similar surface morphology. For the hybrid electrode, graphene flakes covered the surface completely, and no Au NPs were seen (see Figure 5. 7b), which indicates that the film was thick enough to completely cover the immobilized Au NPs. The average size of flakes was larger than 100 nm, whereas that of the Au NPs was approximately 17 nm. If we consider the relative size of the graphene flakes as compared to that of the Au NPs and the thickness of the graphene flake film deposited on the arrays of Au NPs, the surface morphology of the hybrid electrode should not be affected significantly by the immobilized Au NPs. Therefore, the graphene flake and hybrid counter electrodes might have similar surface morphologies. Also, the Au NPs were covered completely with the deposited graphene flake film, and thus they could not come into direct contact with I_3^- ions in the reduction process of the DSSC. The Au NPs might be also protected from corrosion by the graphene flake film.

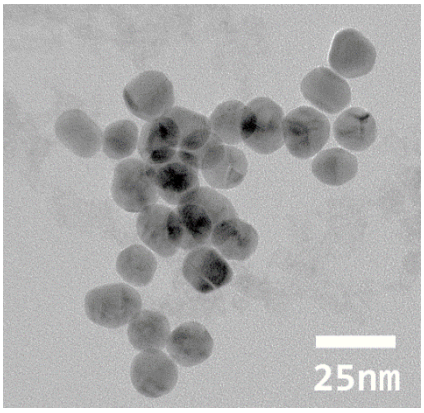

Figure 5. 9. TEM image of colloidal Au NPs. The size of colloidal Au NPs is about 17 ± 4 nm.

5. 3. 3. Photovoltaic properties of DSSCs with hybrid counter electrode

Figure 5. 10a shows the *J*–*V* curves of the DSSCs fabricated with a conventional Pt, graphene flake, and hybrid counter electrodes measured in air mass 1.5 sunlight. The thickness of the active layer was 8.2 μm and that of the scattering layer was 8 μm. The photovoltaic parameters are summarized in Table 5. 1. For the DSSC with a Pt counter electrode, the short-circuit current density (J_{sc}), open-circuit voltage (V_{oc}), fill factor (*ff*), and overall conversion efficiency (η) were 16.28 mA/cm^2, 0.77 V, 0.72, and 9.02%, respectively. For the DSSC with a graphene flake electrode, the photovoltaic parameters were 16.51 mA/cm^2, 0.78 V, 0.69, and 8.91%, respectively. The DSSC with a hybrid electrode showed the best electrochemical performance, with photovoltaic parameters of 0.78 V, 17.54 mA/cm^2, 0.71, and 9.71%, respectively.

By including Au NPs between the layers of FTO and graphene flakes, all the photovoltaic parameters such as short-circuit current density, open-circuit voltage, and fill factor were improved, and consequently the conversion efficiency was

improved significantly. Therefore, there is no doubt that the included Au NPs had an important role in enhancing the solar efficiency. It is also supported by the IPCE data (see Figure 5. 10b). For the DSSC with a hybrid counter electrode, the IPCE spectrum was enhanced over a broad wavelength range from 450 to 700 nm. Particularly, the relative intensity near 530 nm was enhanced significantly. Au NPs have a strong extinction peak centered at 530 nm.

Table 5. 1. Photovoltaic properties of DSSCs with a Pt, graphene flake and hybrid counter electrodes.

Counter electrodes	V_{oc} (V)	J_{sc} (mA/cm^2)	*ff*	η (%)
Pt	0.77	16.28	0.72	9.02
Graphene flake	0.78	16.51	0.69	8.91
Hybrid	0.78	17.54	0.71	9.71

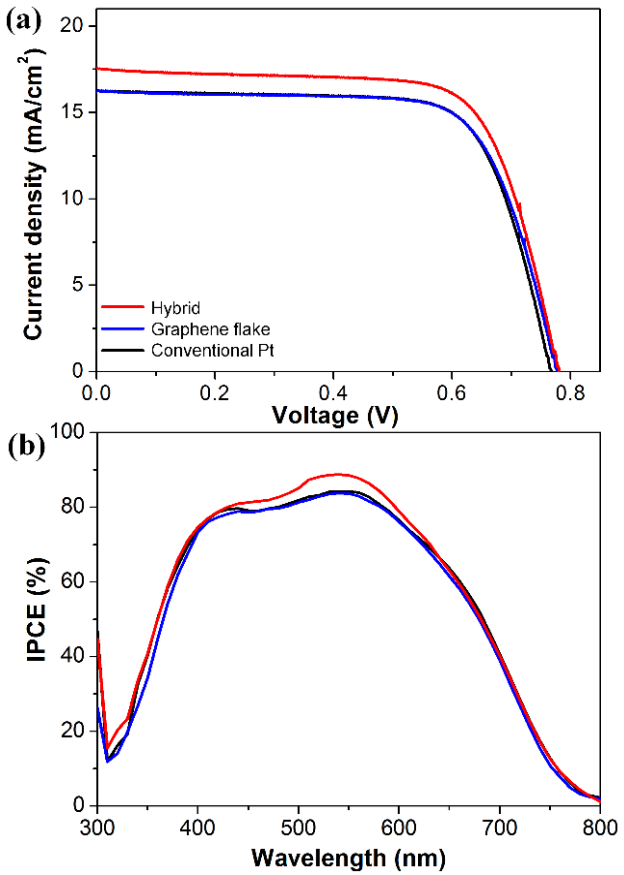

Figure 5. 10. (a) J–V curves and (b) IPCE spectra measured from DSSCs with hybrid (red), graphene flake (blue), and conventional Pt (black) counter electrodes .

The typical red color of Au NPs is due to their localized surface plasmon resonances (LSPRs).[100, 111] LSPR is excited when the frequency of light photons matches the natural frequency of the collective oscillation of conduction electrons in metal NPs. LSPRs create sharp spectral scattering and absorption peaks, as well as strong electromagnetic near-field enhancements. Although Au NPs were included in the counter electrode, the scattered light from the Au NPs could affect the absorption of dye molecules existing at the active layer. Therefore, it is necessary to consider the effect of the Au NPs on the active layer, in addition to their effect on the counter electrode.

N719 dye, which was used in the fabrication of our DSSCs, has two strong absorption bands centered at 393 and 533 nm. The solar intensity is much stronger at 533 nm than at 393 nm, and the band centered at 533 nm can absorb more solar light than that centered at 393 nm. The LSPR of the Au NPs was well matched with the absorption band centered at 533 nm. Au NPs were included in the counter electrode, whereas the N719 dye was adsorbed at the surface of the TiO_2 NPs that formed the active layer. Therefore, they were physically separated. However, the scattered light from the Au NPs included in the hybrid counter electrode could increase the absorption of the

N719 dye.

We therefore studied the effect of the Au NPs on the absorption of the N719 dye by varying the thickness of the active layer with and without the scattering layer. The efficiency difference between the DSSC with the hybrid electrode and that with the graphene flake electrode increased with decreasing thickness of the active layer (Table 5. 2). Also, the efficiency difference was larger for the DSSCs fabricated without a scattering layer than for those fabricated with a scattering layer (see Table 5. 3). There is no doubt that without a scattering layer, more light would reach the Au NPs included in the counter electrode and more light would be reflected from them. Therefore, by including Au NPs in the counter electrode, the photo-conversion efficiency was enhanced somewhat through increasing the absorption of dye molecules by the reflected light from the Au NPs. However, it is very difficult to determine the contribution quantitatively because the effect of the Au NPs on the counter electrode itself might also increase with increasing light intensity reaching the counter electrode.

Table 5. 2. Photovoltaic properties of the DSSCs with conventional Pt, graphene flakes and hybrid counter electrodes for different thickness of TiO_2 active layer with scattering layer.

	V_{oc} (V)	J_{sc} (mA/cm^2)	*ff* (%)	η (%)
Pt 8.2 μm	0.77	16.28	0.72	9.02
Graphene flakes 3.5 μm	0.79	14.81	0.70	8.15
Graphene flakes 5.1 μm	0.79	15.55	0.69	8.54
Graphene flakes 6.9 μm	0.78	16.50	0.69	8.78
Graphene flakes 8.2 μm	0.78	16.51	0.69	8.91
Graphene flakes 10.2 μm	0.77	16.54	0.68	8.75
Hybrid 3.5 μm	0.80	16.02	0.71	9.17
Hybrid 5.1 μm	0.79	17.06	0.71	9.39
Hybrid 6.9 μm	0.78	17.62	0.70	9.62
Hybrid 8.2 μm	0.78	17.54	0.71	9.71
Hybrid 10.2 μm	0.77	17.15	0.70	9.25

Table 5. 3. Photovoltaic properties of the DSSCs with conventional Pt, graphene flakes and hybrid counter electrodes for different thickness of TiO_2 active layer without scattering layer.

	V_{oc} (V)	J_{sc} (mA/cm^2)	*ff* (%)	η (%)
Graphene flakes 3.5 μm	0.82	7.53	0.66	4.05
Graphene flakes 5.1 μm	0.81	9.90	0.65	5.25
Graphene flakes 6.9 μm	0.80	10.56	0.65	5.47
Graphene flakes 8.2 μm	0.79	10.78	0.65	5.59
Graphene flakes 10.2 μm	0.78	12.48	0.65	6.35
Hybrid 3.5 μm	0.83	10.05	0.65	5.40
Hybrid 5.1 μm	0.82	12.04	0.66	6.49
Hybrid 6.9 μm	0.81	12.66	0.65	6.66
Hybrid 8.2 μm	0.81	12.80	0.65	6.75
Hybrid 10.2 μm	0.80	13.18	0.66	6.85
Pt 8.2 μm	0.85	9.76	0.69	5.70

5. 3. 4. Electrochemical properties of DSSCs with hybrid counter electrode

To understand the effect of Au NPs on the counter electrode itself, we carried out cyclic voltammetry (CV) and electrochemical impedance spectroscopy (EIS) analyses. The cyclic voltammogram (CV) curves for the three types of counter electrodes are shown in Figure 5. 11a. There are two typical pairs of oxidation-reduction peaks as results of two reactions: $I_3^- + 2e^- \leftrightarrow 3\ I^-$ (i_{ox}/i_{red}) and $3\ I_2 + 2e^- \leftrightarrow 2\ I_3^-$ (ii_{ox}/ii_{red}). The first pair is related to the oxidation and reduction of I^-/I_3^- (i_{ox}/i_{red}), and the second pair is related to the oxidation and reduction of I_2/I_3^- (ii_{ox}/ii_{red}). Because the reduction of I_3^- to I^- occurs on the counter electrode of DSSCs, the redox potential of the first pair (i_{ox}/i_{red}) is important in this study.

The peak current intensity of i_{red} and the peak-to-peak separation (E_{pp}) between i_{ox} and i_{red} are important parameters for characterizing the catalytic activities of the counter electrode. The high absolute intensity of i_{red} reveals a faster reduction velocity, which means the counter electrode is

better able to reduce the I_3^- species to I^-.[111,143] The peak current intensity (i_{red}) of the hybrid electrode was −1.79 mA, which is much higher in absolute value than those of the graphene flake (−1.17 mA) or Pt (−0.97 mA) electrodes. This means that the hybrid electrode had a much higher catalytic rate for I^- regeneration than the others. The values of E_{pp} for the hybrid, graphene flake, and Pt counter electrodes were 0.37, 0.42, and 0.47 V, respectively. It is known that the value of E_{pp} is inversely proportional to the charge transfer rate.[143,167] This means that the catalytic activity is improved with decreasing E_{pp}. Therefore, the hybrid electrode had better catalytic activity than the other two electrodes.

Figure 5. 11b shows Nyquist plots of the EIS spectra for all three DSSCs. They were recorded in the frequency range of 100 kHz and 0.1 Hz. The equivalent circuit is shown in the inset. The parameter values obtained from fitting are reported in Table 5. 4. R_s, which corresponds to the value on the x−axis where the first semicircle begins on the left−hand side, is assigned to the ohmic serial resistance from the conductive substrates. The hemisphere in the high−frequency region is assigned to the parallel combination of the resistance (R_{ct}) and capacitance at the electrode/electrolyte interface and to the

interface between the FTO and TiO_2 layers. The hemisphere in the intermediate and low-frequency regions offer information on the resistance (R_w) and capacitance at the TiO_2/electrolyte interface, while those on the resistance (R_n) and capacitance due to the Nernst diffusion of I_3^- within the electrolyte, respectively.[156,168]

The R_{ct} value for the DSSC with a hybrid electrode was 10.54 Ω, which was the lowest value (see Table 5. 4). Because the same electrolyte solution was used and the interface between the FTO and TiO_2 layers was the same for all three DSSCs, the difference in the R_{ct} values might be due to the difference in the charge-transfer resistance between the electrode and the electrolyte. The charge-transfer resistance is related to the inverse of the current density (J) as follows: $R_{ct} = RT/nFJ$,[29] where R, T, n, and F are the gas constant, temperature, the number of electrons transferred in the elementary electrode reaction (n = 2), and Faraday's constant, respectively. Because a lower charge-transfer resistance gives a higher current density, the DSSC with a hybrid counter electrode had the highest current density of 17.54 mA/cm^2 (see Table 5. 1). These results show that the hybrid electrode had better catalytic activity and lower charge transfer resistance than the

other two electrodes. Consequently, the DSSC with a hybrid electrode had the highest photo-conversion efficiency. In the Bode plot (see Figure 5. 12.), the position of the middle frequency (f_{mid}) peak for all three DSSCs was the same, 14.36 Hz. Thus, for all three DSSCs, the electron lifetime (τ_{eff}) was calculated to be 11.09 ms from the relation $\tau_{eff} = 1/(2\pi f_{mid})$.[84,158] Thus, the electron lifetime was not affected by the type of counter electrode.

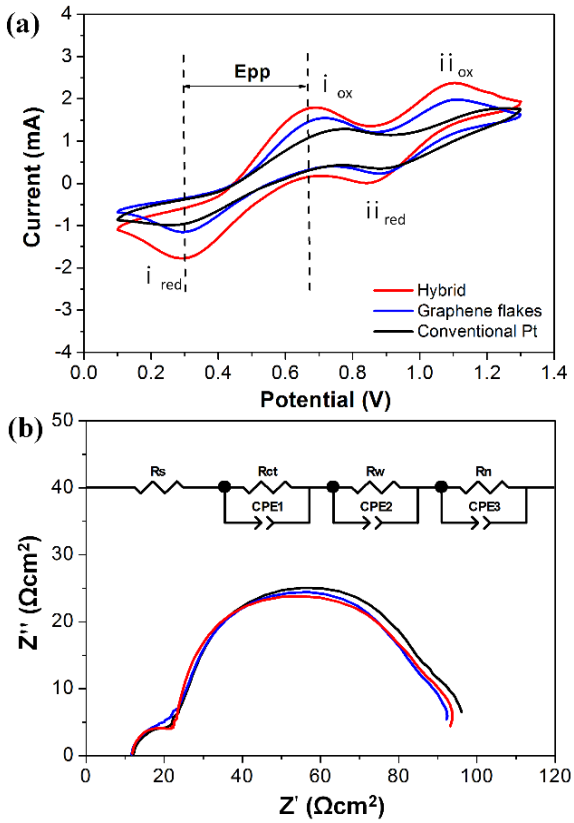

Figure 5. 11. Cyclic voltammograms of hybrid, graphene flake, and conventional Pt counter electrodes at a scan rate of 50 mV/s in a CH_3CN solution containing 0.1 M $LiClO_4$, 10 mM LiI, and 1 mM I_2. The reference electrode was Ag/Ag^+. (b) Nyquist plots of the DSSCs with hybrid, graphene flake, and conventional Pt counter electrodes. Measurements were performed at 0.7 V under illumination conditions.

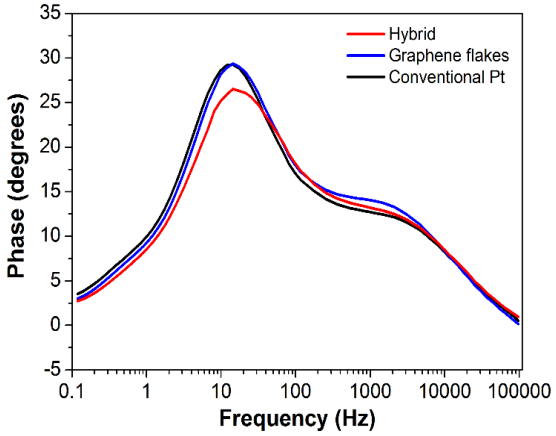

Figure 5. 12. Bode plot of the DSSCs based on conventional Pt, graphene flakes, and hybrid counter electrode under illumination condition.

Table 5. 4. Electrochemical Parameters of the DSSCs with conventional Pt, graphene flake and hybrid counter electrodes.

	R_s (Ωcm^2)	R_{ct} (Ωcm^2)	R_w (Ωcm^2)	R_n (Ωcm^2)	τ_{eff} (ms)
Hybrid	11.84	10.54	53.02	290	11.09
Graphene flakes	11.67	11.78	52.12	265	11.09
Pt	11.98	10.89	57.88	312	11.09

By including Au NPs between the FTO layer and graphene flakes, the catalytic activity was improved and the charge-transfer resistance was decreased. It is known that LSPRs decay either radiatively or into (quasi) particles such as electron-hole (e-h) pairs.[160] The former decay path gives rise to dramatic electromagnetic field enhancements, such as in surface-enhanced Raman spectroscopy. It is known that by the latter decay path, the light absorption of dye molecules adsorbed on or near metal NPs is enhanced[161] and also that the efficiency of a nanostructured Pt counter electrode for DSSCs is improved.[169] In our hybrid electrode, graphene flakes are on the arrays of Au NPs. When the conduction electrons of Au NPs are excited by light, the excited energetic electrons can be transferred to the graphene flakes and used to reduce I_3^- ions. In this case, the catalytic activity of the graphene flakes could be improved and the charge-transfer resistance at the electrode/electrolyte interface could be decreased. These effects could take place only when light reaches the hybrid electrode.

We carried out similar experiments for all three DSSCs, each with an added panchromatic layer[104] of Ag nanoplates between the active layer and the scattering layer. The photo-conversion

efficiency of the DSSC with the hybrid counter electrode was lower than that with the graphene flake counter electrode (see Table 5. 5). This result may be because the panchromatic layer could reflect light like a mirror, and thus almost no light could reach the counter electrode. Without light, the conduction electrons of the Au NPs could not be excited. Thus, the Au NPs could quench the electrons and interrupt the electron transfer from FTO to the graphene flakes instead of helping.

Table 5. 5. Photovoltaic properties of the DSSCs included a panchromatic layer of Ag nanoplates between the active layer and scattering layer, with three kinds counter electrodes. Thickness of active layer is 8.2 μm and scattering layer is 8 μm.

	V_{oc} (V)	J_{sc} (mA/cm^2)	ff (%)	η (%)
Pt	0.80	18.89	0.72	10.96
Graphene flakes	0.80	15.73	0.69	8.71
Hybrid	0.80	15.41	0.70	8.63

5. 4. Conclusion

We succeeded in fabricating a nanostructure-based graphene flake counter electrode for DSSCs by immobilization of Au NPs on FTO glass and deposition of a thin graphene flake film. Graphene flakes fabricated using thermal plasma jet were well dispersed by sonication, and films of graphene flake could be fabricated easily. The efficiency of the DSSC with a graphene flake/Au NP/FTO counter electrode was as high as 9.71%, which is higher than that of DSSCs with a conventional Pt/FTO counter electrode (9.02%) or a graphene flake/FTO counter electrode (8.91%). The relatively high efficiency was due to the plasmonic effect of the Au NPs included in the counter electrode. Although the Au NPs were included in the counter electrode, the absorption of dye molecules at the active layer was increased somewhat by the scattered light from the Au NPs. When the conduction electrons of Au NPs were excited by light reaching the electrode, they were involved in the electron transfer from FTO to the graphene flakes. Consequently, the catalytic activity of graphene flakes was improved and the charge-transfer resistance at the electrode/electrolyte

interface decreased.

Reference

(1) A. Hagfeldt, G. Boschloo, L. Sun, L. Kloo and H. Pettersson, *Chem. Rev.*, 2010, **110**, 6595-6663.

(2) B. O' Regan, and M. Grätzel, *Nature*, 1991, **353**, 737-740.

(3) M. K. Nazeeruddin, A. Kay, I. Rodicio, R. Humphry-Baker, E. Mueller, P. Liska, N. Vlachopoulos, and M. Grätzel, *J. Am. Chem. Soc.* 1993, **115**, 6382-6390.

(4) A. Shah, P. Torres, R. Tscharner, N. Wyrsch, and H. Keppner, *Science*, 1999, **285**, 692-698.

(5) M. Grätzel, *Nature*, 2001, **414**, 338-344.

(6) M. Grätzel, *J. Photochem. Photobiol. C*, 2003, **4**, 145-153.

(7) M. Grätzel, *J. Photochem. Photobiol. A*, 2004, **164**, 3-14.

(8) G. E.Tulloch, *J. Photochem. Photobiol. A*, 2004, **164**, 209-219.

(9) M. Ye, X. Wen, M. Wang, J. Iocozzia, N. Zhang, C. Lin, and Z. Lin, *Mater. Today*, 2015, **18** ,155-162.

(10) L. E. Chaar, L. A. lamont, and N. E. Zein, *Renew. Sustain. Energy Rev.,* 2011, **15**, 2165-2175.

(11) M. Grätzel, *Prog. Photovolt. Res. Appl.*, 2006, **14**, 429-442.

(12) C.-Y. Chen, M. Wang, J.-Y. And Li, N. Pootrakulchote, L. Alibabaei, C.-h. Ngoc-le, J.-D. Decoppet, J.-H. Tsai, C. Grätzel, and C.-G. Wu, *ACS Nano*, 2009, **3**, 3103-3109.

(13) J. Gong, J. Liang, and K. Sumathy, *Renew. Sustain. Energy Rev.*, 2012, **16**, 5848-5860.

(14) M. K. Nazeeruddin, E. Baranoff, and M. Grätzel, *Solar Energy*, 2011, **85**, 1172-1178.

(15) B. E. Hardin, H. J. Snaith, and M.D. McGehee, *Nature photonics*, 2012, **6**, 162-169.

(16) M. I. Khan, *A Study on the Optimization of Dye-Sensitized Solar Cells*, Graduate Theses and Dissertations, University of South Florida, USA, **2013**.

(17) J. Maçaira, L. Andrade, and A. Mendes, *Renew. Sustain. Energy Rev.*, 2013, **27**, 334-349.

(18) C. J. Barbé, F. Arendse, P. Comte, M. Jirousek, F. Lenzmann, V. Shklover, and M. Grätzel, *J. Am. Ceram. Soc.*, 1997, **80**, 3157-3171.

(19) M. K. Nazeeruddin, F. D. Angelis , S. Fantacci, A. Selloni, G. Viscardi, P. Liska, S. Ito, B. Takeru, and M. Grätzel, *J. Am. Chem. Soc.*, 2005, **127**, 16835-16847.

(20) J. Wu, Z. Lan, J. Lin, M. Huang, Y. Huang, L. Fan, and G. Luo, *Chem. Rev.*, 2015, **115**, 2136-2173.

(21) J. Wu, Z. Lan, S. Hao, P. Li, J. Lin, M. Huang, L. Fang, and Y. Huang, *Pure Appl. Chem.,* 2008, **80**, 2241-2258.

(22) Z. Yu, N. Vlachopoulos, M. Gorlov, and L. Kloo, *Dalton Trans.*, 2011, **40**, 10289-10303.

(23) S. Huang, G. Schlichthorl, A. Nozik, M. Grätzel, and A. Frank, *J. Phys. Chem. B.,* 1997, **101**, 2576-2582.

(24) G. Boschloo, L. Haggman, and A. Hagfeldt, *J. Phys. Chem. B.*, 2006, **110**, 13144-13150.

(25) N. Kopidakis, N. R. Neale, and A. J. Frank, *J. Phys. Chem. B.*, 2006, **110**, 12485-12489.

(26) L. Zeng, S. Dai, K. Wang, X. Pan, C. Shi, and L. Guo, *Chinese Physics Letters*, 2004, **21**, 1835-1837.

(27) Y.-S. Yen, H.-H. Chou, Y.-C. Chen, C.-Y. Hsu and J. T. Lin, *J. Mater. Chem.*, 2012, **22**, 8734-8747.

(28) M. Wu, and T. Ma, *J. Phys. Chem. C.*, **2014**, *118*, 16727-16742.

(29) S. Thomas, T. G. Deepak, G. S. Anjusree, T. A. Arun, S. V. Nair and A. S. Nair, *J. Mater. Chem. A.*, 2014, **2**, 4474-4490.

(30) B. Qi and J. Wang, *J. Mater. Chem.*, 2012, **22**, 24315-24325.

(31) N. K. Elumalai and A. Uddin, *Energy Environ. Sci.*, 2016, **9**, 391-410.

(32) Qi. Zhang, T. P. Chou, B. Russo, S. A. Jenekhe, and G. Cao, *Adv. Funct. Mater.*, 2008, **18**, 1654-1660.

(33) M. Belarbi, A. Benyoucef, and B. Benyoucef, *Adv. Energy. Inter. J.*, 2014, **1**, 2-1-8.

(34) M. Wolf, and H. Rauschenbacht, *Adv. Energy. Con.,* 1963,

3, 455–479.

(35) D. Bartesaghi, I. D C. Perez, J. Kniepert, S. Roland, M. Turbiez, D. Neher and L. J. A. Koster, *Nature Comm.*, 2015, **6**, 7083–1–10.

(36) A. Hagfeldt, M. Grätzel, *Chem. Rev.*, 1995, **95**, 49–68.

(37) Y. Chen and H. Ming, *Photonic Sensors,* 2012, **2**, 37-49.

(38) R. P. V. Duyne, *Science*, 2004, **306**, 985-986.

(39) A. J. Haes, C. L. Haynes, A. D. McFarland, S. Zou, G. C. Schatz, and R. P. V. Duyne, *MRS Bull.* 2005, **30**, 368-375.

(40) X. Zhang, M. A. Young, O. Lyandres, and R. P. V. Duyne, *J. Am. Chem. Soc.*, 2005, **127**, 4484-4489.

(41) K. L. Kelly, E. Coronado, L. Zhao, and G. C. Schatz, *J. Phys. Chem. B.*, 2003,**107**, 668-677.

(42) K. A. Willets and R. P. V. Duyne, *Annu. Rev. Phys. Chem.* 2007. **58**, 267-297.

(43) J. J. Mock, M. Barbic, D. R. Smith, D. A. Schultz, and S. Schultz, *J. Chem. Phys.*, 2002, **116**, 6755-6759.

(44) C. L. Haynes, A. D. McFarland, M. T. Smith, J. C. Hulteen, and R. P. V. Duyne, *J. Phys. Chem. B.*, 2002, **106**, 1898-1902.

(45) M. M. Miller, and A. A. Lazarides, *J. Phys. Chem. B.*, 2005, **109**, 21556-21565.

(46) M. M. Alvarez, J. T. Khoury, T. G. Schaaff, M. N. Shafigullin, I. Vezmar, and R. L. Whetten, *J. Phys. Chem. B.*,

1997, **101**, 3706-3712.

(47) J. P.-Juste, I. P.-Santos, L. M. L.-Marzan, and P. Mulvaney, *Coord. Chem. Rev.*, 2005, **249**, 1870-1901.

(48) J. M. Luther, P. K. Jain, T. Ewers and A. P. Alivisatos, *Nat. Mater.*, 2011, **10**, 361-366.

(49) E. Petryayeva, and U. J. Krull, *Anal. Chim. Acta*, 2011, **706**, 8-24.

(50) X. Lu, M. Rycenga, S. E. Skrabalak, B. Wiley, and Y. Xia, *Annu. Rev. Phys. Chem.*, 2009, **60**, 167-192.

(51) L. M. Liz-Marzan, *Langmuir*, 2006, 22, 32-41.

(52) H.-D. Yu, M. D. Regulacio, E. Ye and M.-Y. Han, *Chem. Soc. Rev.*, 2013, **42**, 6006-6018.

(53) A. Biswas, I. S. Bayer, A. S. Biris, T. Wang, E. Dervishi and F. Faupel, *Adv. Colloid Interface Sci.*, 2012, **170**, 2-27.

(54) P. Maury, D. N. Reinhoudt and J. Huskens, *Unconventional Nanopatterning Techniques and Applications*, ed. J. A. Rogers and H. H. Lee, John Wiley & Sons, Inc., New Jersey, **2009**, pp. 379-406.

(55) T. Ito and S. Okazaki, *Nature*, 2000, **406**, 1027-1031.

(56) D. Qin and B. Riggs, *Encyclopedia of Supramolecular Chemistry*, ed. J. L. Atwood, J. W. Steed and K. J. Wallace, Taylor & Francis, New York, **2012**, 10.1081/E-ESMC-120047104.

(57) D. Mailly, *Eur. Phys. J. Spec. Top.*, 2009, **172**, 333-342.

(58) J. E. E. Baglin, *Appl. Surf. Sci.*, 2012, **258**, 4103-4111.

(59) Y. Qiao, D. Wang and J. M. Buriak, *Nano Lett.*, 2007, **7**,464-469.

(60) T. Fujita, H. Okada, K. Koyama, K. Watanabe, S. Maekawa and M. W. Chen, *Phys. Rev. Lett.*, 2008, **101**, 166601-1-4.

(61) H. D. Yu, D. Yang, D. Wang and M. Y. Han, *Adv. Mater.*, 2010, **22**, 3181-3184.

(62) H. D. Yu, D. Wang and M. Y. Han, *J. Am. Chem. Soc.*, 2007, **129**, 2333-2337.

(63) S. M. George, *Chem. Rev.*, 2010, **110**, 111-131.

(64) M. Knez, K. Nielsch, and L. Niinistö, Adv. Mater. 2007, 19, 3425-3458.

(65) M. Leskelä, M. Kemell, K. Kukli, V. Pore, E. Santala, M. Ritala, and J. Lu, *Mater. Sci. Eng. C.*, 2007, **27**, 1504.

(66) M. Knez, A. Kadri, C. Wege, U. Goesele, H. Jeske, and K. Nielsch, Nano Lett., 2006, **6**, 1172-1177.

(67) E. Dervishi, Z. Li, F. Watanabe, Y. Xu, V. Saini, A. R. Biris, and A. S. Biris, *J. Mater. Chem.* 2009, **19**, 3004-3012.

(68) A. R. Birisa, A. S. Birisb, D. Lupua, S. Trigwellc, E. Dervishid, Z. Rahmane, and P. Marginean, *Chem. Phys. Lett.* 2006, **429**, 204-208.

(69) A. R. Biris, D. Lupu, A. Grüneis, P. Ayala, M. H. Rümmeli, T. Pichler, Z. Li, Y. Xu, I. Misan, E. Dervishi and A. S. Biris.

Chem. Mater., 2008, **20**, 3466-3472.

(70) L. C. Palmer, and S. I. Stupp, *Acc. Chem. Res.*, 2008, 41, 1674-1684.

(71) S. A. DiBenedetto, A. Facchetti, M. A. Ratner, and T. J. Marks, *Adv. Mater.*, 2009, **21**, 1407-1433.

(72) B. Sepulveda, P. C. Angelome, L. M. Lechuga, and L. M. Liz-Marzan, *Nano Today*, 2009, **4**, 244-251.

(73) M. Grzelczak, J. P.-Juste, P. Mulvaney, L. M. L.-Marzan, *Chem. Soc. Rev.*, 2008, **37**, 1783-1791.

(74) J. Zeng, X. H. Xia, M. Rycenga, P. Henneghan, Q. G. Li, and Y. N. Xia, *Angew. Chem. Int. Ed.*, 2011, **50**, 244-249.

(75) S. H. Chen, and D. L. Carroll, *Nano Lett.*, 2002, **2**, 1003-1007.

(76) W. Niu and G. Xu, *Nano Today*, 2011, **6**, 265-285.

(77) J. Turkevich, P. C. Stevenson and J. Hillier, *Discuss. Faraday Soc.*, 1951, **11**, 55-75.

(78) H. Bonnemann, W. Brijoux, R. Brinkmann, E. Dinjus, R. Fretzen, T. JoulSen and B. Korall, *Jour. Mol. Catal.*, 1992, **74**, 323-333.

(79) B. L. Cushing, V. L. Kolesnichenko, and C. J. O'Connor, *Chem. Rev*. 2004, **104**, 3893-3946.

(80) M. Ihara, K. Tanaka, K. Sakaki, I. Honma and K. Yamada, *J. Phys. Chem. B*, 1997, **101**, 5153-5157.

(81) S. D. Standridge, G. C. Schatz and J. T. Hupp, *Langmuir*,

2009, **25**, 2596-2600.

(82) A. Baba, K. Wakatsuki, K. Shinbo, K. Kato and F. Kaneko, *J. Mater. Chem.*, 2011, **21**, 16436-16441.

(83) Y. Wang, J. Zhai and Y. Song, *Phys. Chem. Chem. Phys.*, 2015,**17**, 5051-5056.

(84) Y. Wang, J. Zhai and Y. Song, *RSC Adv.*, 2015, **5**, 210-214.

(85) J.-L. Wu, F.-C. Chen, Y.-S. Hsiao, F.-C. Chien, P. Chen,C.-H. Kuo, M. H. Huang and C.-S. Hsu, *ACS Nano*, 2011, **5**, 959-967.

(86) W. Jiang, H. Liu, L. Yin and Y. Yin, *J. Mater. Chem. A*, 2013, **1**, 6433-6440.

(87) S. D. Standridge, G. C. Schatz and J. T. Hupp, *J. Am. Chem. Soc.*, 2009, **131**, 8407-8409.

(88) M. D. Brown, T. Suteewong, R. S. S. Kumar, V. D' Innocenzo, A. Petrozza, M. M. Lee, U. Wiesner and H. J. Snaith, *Nano Lett.*, 2011, **11**, 438-445.

(89) N. C. Jeong, C. Prasittichai and J. T. Hupp, *Langmuir*, 2011, **27**, 14609-14614.

(90) Y.-C. Yen, P.-H. Chen, J.-Z. Chen, J.-A. Chen and K.-J. Lin, *ACS Appl. Mater. Interfaces*, 2015, **7**, 1892-1898.

(91) T. Kawawaki, Y. Takahashi and T. Tatsuma, *J. Phys. Chem. C*, 2013, **117**, 5901-5907.

(92) S. W. Sheehan, H. Noh, G. W. Brudvig, H. Cao and C. A. Schmuttenmaer, *J. Phys. Chem. C*, 2013, **117**, 927-934.

(93) J. T. Park, W. S. Chi, H. Jeon and J. H. Kim, *Nanoscale*, 2014, **6**, 2718-2729.

(94) J. Yun, S. H. Hwang and J. Jang, *ACS Appl. Mater. Interfaces*, 2015, **7**, 2055-2063.

(95) Y. H. Jang, Y. J. Jang, S. T. Kochuveedu, M. Byun, Z. Lin and D. H. Kim, *Nanoscale*, 2014, **6**, 1823-1832.

(96) M. K. Gangishetty, R. W. J. Scott and T. L. Kelly, *Langmuir*, 2014, **30**, 14352-14359.

(97) H. Jung, B. Koo, J.-Y. Kim, T. Kim, H. J. Son, B. S. Kim, J. Y. Kim, D.-K. Lee, H. Kim, J. Cho and M. J. Ko, *ACS Appl. Mater. Interfaces*, 2014, **6**, 19191-19200.

(98) H. F. Zarick, O. Hurd, J. A. Webb, C. Hungerford, W. R. Erwin and R. Bardhan, *ACS Photonics*, 2014, **1**, 806-811.

(99) M. K. Gangishetty, K. E. Lee, R. W. J. Scott and T. L. Kelly, *ACS Appl. Mater. Interfaces*, 2013, **5**, 11044-11051.

(100) H. Choi, W. T. Chen and P. V. Kamat, *ACS Nano*, 2012, **6**, 4418-4427.

(101) X. Dang, J. Qi, M. T. Klug, P.-Y. Chen, D. S. Yun, N. X. Fang,P. T. Hammond and A. M. Belcher, *Nano Lett.*, 2013, **13**, 637-642.

(102) H.-Y. Kim, D. H. Song, H. Yoon and J. S. Suh, *RSC Adv.*, 2015, **5**, 27464-27469.

(103) H.-Y. Kim, W.-Y. Rho, H. Y. Lee, Y. S. Park and J. S. Suh, *Sol. Energy*, 2014, **109**, 61-69.

(104) H.-Y. Kim, and J. S. Suh, *RSC Adv.*, 2015, **5**, 59895-59902.

(105) J. Qi, X. Dang, P. T. Hammond, and A. M. Belcher, *ACS Nano*, 2011, **5**, 7108-7116.

(106) C.-H. Chou and F.-C. Chen, *Nanoscale*, 2014, **6**, 8444-8458.

(107) E. Stratakis, and E. Kymakis, *Materials Today*, 2013, **16**, 133-146.

(108) H. A. Atwater, A. Polman, *Nat. Mater.* 2010, **9**, 205-213.

(109) D. M. Schaadt, B. Feng, and E. T. Yu, *Appl. Phys. Lett.*, 2005, **86**, 063106-1-3.

(110) D. Derkacs, S. H. Lim, P. Matheu, W. Mar, and E. T. Yu, *Appl. Phys. Lett.*, 2006, 89, 093103-1-3.

(111) W. L. Liu, F. C. Lin, Y. C. Yang, C. H. Huang, S. Gwo, M. H. Huang and J. S. Huang, *Nanoscale*, 2013, **5**, 7953-7962.

(112) S. P. Lim, A. Pandikumar, N. M. Huang, H. N. Lim, Gu. Gud and T. Li Ma, *RSC Adv.*, 2014, **4**, 48236-48244.

(113) A. K. Geim and K. S. Novoselov, *Nature Mat.*, 2007, **6**, 183-191.

(114) K. S. Novoselov, A. K. Geim, S. V. Morozov, D. Jiang, Y. Zhang, S. V. Dubonos, I. V. Grigorieva, A. A. Firsov. *Science*, 2004, **306**, 666-669.

(115) Y. Zhang, Y. -W. Tan, H. L. Stormer, P. Kim, *Nature*, 2005, **438**, 201-204.

(116) M. Yi and Z. Shen, *J. Mater. Chem. A*, 2015, **3**, 11700-11715.

(117) Y. Zhang, J. P. Small W. V. Pontius, and P. Kim, *Appl. Phys. Lett.*, 2005, **86**, 073104-1-3.

(118) W. Norimatsu and M. Kusunoki, *Phys. Chem. Chem. Phys.*, 2014, **16**, 3501-3511.

(119) D. V. Badami, *Carbon*, 1965, **3**, 53-54.

(120) C. Berger, Z. Song, T. Li, X. Li, A., Y. Ogbazghi, R. Feng, Z. Dai, A. N. Marchenkov, E. H. Conrad, P. N. First and and W. A. de Heer, *J. Phys. Chem.*, 2004, **108**, 19912-19916.

(121) K. V. Emtsev, A. Bostwick, K. Horn, J. Jobst, G. L. Kellogg, L. Ley, J. L. McChesney, T Ohta, S. A. Reshanov, J. Röhrl, E. Rotenberg, A. K. Schmid, D. Waldmann, H. B.Weber and T. Seyller, *Nature Mat.*, 2009, **8**, 203-207.

(122) C. Mattevi, H. Kima and M. Chhowalla, *J. Mater. Chem.,* 2011, **21**, 3324-3334.

(123) Q. Zheng, J. -K. Kim, *Graphene for Tansparent Conductors*, Springer, NY, USA, **2015**, pp 29-94.

(124) S. Horiuchi, T. Gotou, M. Fujiwara, T. Asaka, T. Yokosawa, and Y. Matsui, *Appl. Phys. Lett.*, 2004. **84**, 2403-1-4.

(125) S. Stankovich, R. D. Piner, S. T. Nguyen, and R. S. Ruoff, *Carbon*, 2006, 44, 3342-3347.

(126) X. Li, G. Zhang, X. Bai, X. Sun, X. Wang, E. Wang and H.

Dai, *Nat. nanotech.*, 2008, **3**, 538-542.

(127) J. Kim, L. Cote, F. Kim, and J. Huang, *J. Am. Chem. Soc.,* 2010, **132**, 260-267.

(128) C. Soldano, A. Mahmood, and E. Dujardin, *Carbon*, 2010, **48**, 2127-2150.

(129) P. Avouris and C. Dimitrakopoulos, *Materials Today*, 2012, 15, 86-97.

(130) H. Wang and Y. H. Hu, *Energy Environ. Sci.*, 2012, **5**, 8182-8188.

(131) N. Papageorgiou, W. F. Maiera and M. Grätzel, *J. Electrochem. Soc.*, 1997, **144**, 876-884.

(132) S. S. Kim, Y. C. Nah, Y. Y. Noh, J. Jo and D. Y. Kim, *Electrochim. Acta*, 2006, 51, 3814-3819.

(133) X. Fang, T. Ma, G. Guan, M. Akiyama, T. Kida and E. Abe, *J. Electroanal. Chem.*, 2004, **570**, 257-263.

(134) A. Kaniyoor and S. Ramaprabhu, *J. Appl. Phys.*, 2011, **109**, 124308-1-7.

(135) D. W. Zhang, X. D. Li, H. B. Li, S. Chen, Z. Sun, X. J. Yin and S. M. Huang, *Carbon*, 2011, **49**, 5382-5388.

(136) L. Kavan, J. Yum and M. Grätzel, *ACS Nano*, 2011, **5**, 165-172.

(137) J. D. Roy-Mayhew, D. J. Bozym, C. Punckt and I. A. Aksay, *ACS Nano*, 2010, **4**, 6203-6211.

(138) S. Stankovich, D. A. Dikin, G. H. B. Dommett, K. M. Kohlhaas, E. J. Zimney, E. A. Stach, R. D. Piner, S. T. Nguyen and R. S. Ruoff, *Nature*, 2006, **442**, 282-286.

(139) W. Hong, Y. Xu, G. Lu, C. Li and G. Shi, *Electrochem. Commun.*, 2008, **10**, 1555-1558.

(140) G. Wang, S. Zhuo and W. Xing, *Mater. Lett.*, 2012, **69**, 27-29.

(141) K. S. Lee, Y. Lee, J. Y. Lee, J. H. Ahn and J. H. Park, *ChemSusChem*, 2012, **5**, 379-382.

(142) F. Gong, H. Wang and Z.-S. Wang, *Phys. Chem. Chem. Phys.*, 2011, **13**, 17676-17682.

(143) R. Bajai, S. Roy, P. Kumar, P. Bajpai, N. Kulshrestha, J. Rafiee, N. Koratkar and D. S. Misra, *ACS Appl. Mater. Interfaces*, 2011, **3**, 3884-3889.

(144) Y. Y. Dou, G. R. Li, J. Song and X. P. Gao, *Phys. Chem. Chem. Phys.*, 2012, **14**, 1339-1342.

(145) P. K. Shen, S. Yin, Z. Li and C. Chen, *Electrochim. Acta*, 2010, **55**, 7969-7974.

(146) B. Munkhbayar, M. J. Nine, J. Jeoun, M. Ji, H. Jeong and H. Chung, *J. Power Sources*, 2013, **230**, 207-217.

(147) H. Choi, H. Kim, S. Hwang, W. Choi and M. Jeon, *Sol. Energy Mater. Sol. Cells*, 2011, **95,** 323-325.

(148) T. Battumur, S. H. Mujawar, Q. T. Truong, S. B. Ambade, D. S. Lee, W. Lee, S. H. Han and S. H. Lee, *Curr. Appl. Phys.*, 2012, **12**, e49-e53.

(149) J. Kim, S. B. Heo, G. H. Gu, and J. S. Suh, *Nanotechnology*, 2010, **21**, 095601-1-6.

(150) H. Y. Kim, M. W. Lee, H. J. Yoon, D. H. Song, J. S. Suh, *Chemphyschem*, 2016, Summitted.

(151) M. Rycenga, C. M. Cobley, J. Zeng, W. Li, C. H. Moran, Q. Zhang, D. Qin, Y. Xia, *Chem. Rev.*, 2011, **111**, 3669-3712.

(152) M. Rycenga, M. R. Langille, M. L. Personick, T. Ozel and C. A. Mirkin, *Nano Lett.*, 2012, **12**, 6218-6222.

(153) S. T. Gentry and M. W. J. Bezpalko, *J. Phys. Chem. C.*, 2010, **114**, 6989-6993.

(154) S. Lee, G. H. Gu, J. S. Suh, *Chem. Phys. Lett.*, 2011, **511**, 121-125.

(155) Q. Xu, F. Liu, Y. Liu, W. Meng, K. Cui, X. Feng, W. Zhang, Y. Huang, *Opt. Express*, 2014, **22**, A301-A310.

(156) Y. J. Kim, M. H. Lee, H. J. Kim, G. Lim, Y. S. Choi, N. G. Park, K. Kim, W. I. Lee, *Adv. Mater.*, 2009, **21**, 3668-3673.

(157) S. Mathew, A. Yella, P. Gao, R. Humphry-Baker, B. F. E. Curchod, N. Ashari-Astani, I. Tavernelli, U. Rothlisberger, M. K. Nazeeruddin and M. Grätzel, *Nat. Chem.*, 2014, **6**, 242-247.

(158) J. Song, Z. Yin, Z. Yang, P. Amaladass, S. Wu, J. Ye, Y. Zhao, W.-Q. Deng, H. Zhang and X.-W. Liu, *Chem.-Eur. J.*, 2011, **17**, 10832-10837.

(159) J. Bisquert, *J. Phys. Chem. B*, 2002, **106**, 325-333.

(160) U. Kreibig and M. Vollmer, Optical Properties of Metal Clusters, Springer Series in Materials Science, Springer, NY, USA, 1995.

(161) C. Langhammer, B. Kasemo and I. Zorić, *J. Chem. Phys.*, 2007, **126**, 194702-1-12.

(162) L. J. Cote, F. Kim, and J. Huang, *J. Am. Chem. Soc.,* 2009, **131**, 1043-1049.

(163) M. W. Lee, H. Y. Kim, H. J. Yoon, and J. S. Suh, *Carbon*, 2016, **106**, 48-55.

(164) J. Kim, and J. S. Suh, *ACS Nano*, 2014, **8**, 4190-4196.

(165) A. C. Ferrari and J. Robertson, *Physical review B*, 2000, **61**, 14095-14107.

(166) D. Lee, J. Seo, X. Zhu, J. Lee, H.-J. Shin, J. M. Cole, T. Shin, J. Lee, H. Lee and H. Su, *Sci. Rep.*, 2013, **3**, 2250-1-5.

(167) M. Wu, X. Lin, Y. Wang, L. Wang, W. Guo, D. Qi, X. Peng, A. Hagfeldt, M. Grätzel, and T. Ma, *J. Am. Chem. Soc.*, 2012, **134**, 3419-3428.

(168) F. Malara, M. Manca, L. D. Marco, P. Pareo, and G. Gigli, *ACS Appl. Mater. Interfaces*, 2011, **3**, 3625-3632.

(169) H. Donga, Z. Wua, Y. Gao, A. El-Shafei, B. Jiao, Y. Dai, and X. Hou, *Organic Electronics*, 2014, **15**, 1641-1649.

국문 초록

염료감응 태양전지는 무한한 태양 빛을 에너지원으로 하는 환경 친화적인 기술로써 전 세계적으로 각광받고 있는 신재생 에너지 연구 분야 중 하나이다. 염료감응 태양전지는 식물의 광합성 원리를 이용하는 것으로 반도체 접합 태양전지에서는 찾아 볼 수 없는 독특한 성질을 가지고 있다. 이에 많은 과학자들이 오랫동안 연구하고 있지만, 여전히 낮은 효율과 불안한 안정성을 해결하지 못하고 있다.

따라서 본 연구에서는 두 가지 접근 방법을 통하여 염료감응 태양전지의 효율을 향상시키고자 하였다. 첫 번째로, 국부적 표면 플라즈마 현상을 나타내는 은 나노입자를 광전극층에 도입하여 플라즈모닉 염료감응 태양전지를 개발하고 이를 통해 효율을 극대화 시키고자 하였다. 두 번째로, 그래핀-금 나노입자를 이용하여 높은 촉매 활성도와 낮은 전하이동 저항을 갖는 상대전극을 개발하고, 기존의 백금 상대전극을 이용한 염료감응 태양전지 보다 높은 효율을 갖는 염료감응 태양전지를 제작하고자 하였다.

첫 번째 연구에서는 은 나노입자의 형태와 크기를 조절하고 이를 이산화티탄 광전극 층에 도입함으로써, 플라즈모닉 염료감응 태양전지를 제작하였다. 은 나노입자는 구 형태가 아닌 판 형태로 제조하여 은 나노판의 플라즈모닉 흡수 밴드와 염료 N719의 두 가시광선 흡수 밴드(λ_{max}=383, 533 nm)의 중첩 정도를 높이고자 하였다. 실제 실험적으로도 플라즈모닉 흡수 밴드와 염료 N719의 흡수 밴드의 중첩 정도가 플라즈모닉 염료감응 태양전지의 효율에 영향을 주는 것으로 관측되었다. 또한, 이산화티탄에 대한 은 나노판의 중량비 역시 플라즈모닉 염료감응 태양전지의 효율에 영향을 미치는 것을 확인하였다. 즉, 제조한 은 나노판이 이산화티탄에 도입 될 때, 중량비가 0.35wt% 일 때까지는 중량비의 증가에 따라 플라즈모닉 염료감응 태양전지의 효율도 함께 증가하였지만, 0.35wt% 이

상의 중량비에서는 오히려 효율이 감소하는 경향을 보였다. 이는 중량비가 증가 할수록 이산화티탄 내에서의 은 나노판간의 응집현상이 일어나게 되고, 이러한 응집현상이 플라즈모닉 염료감응 태양전지의 효율에 부정적인 영향을 미치기 때문임을 실험적으로 밝힐 수 있었다. 은 나노판이 응집되게 되면, 은 나노판의 플라즈몬 흡수 밴드는 장파장으로 이동하여 염료 N719의 흡수 스펙트럼 밴드와 중첩 정도가 감소하게 되고, 이로 인해 플라즈모닉 염료감응 태양전지의 효율이 감소하게 된다. 따라서 플라즈모닉 염료감응 태양전지의 효율을 향상시키기 위해서는 금속 나노입자를 광전극층에 도입 시 금속 간의 응집현상을 방지하고 금속 나노입자가 고유의 플라즈몬 흡수를 유지할 수 있도록 해야 한다.

이 후, 보다 높은 효율을 갖는 플라즈모닉 염료감응 태양전지 제작을 위하여 전 파장 영역의 빛을 흡수 할 수 있는 세 종류 (λ_{max} = 470, 540, 620 nm)의 은 나노판을 이산화티탄 광전극 층에 준-단층으로 도입하였다. 이 때, poly(4-vinylpyridine)(P4VP)를 이용하여 최대 흡수 파장이 540, 620, 470 nm인 은 나노판을 광전극층에 순서대로 흡착-고정 시켰으며, 은 나노판 사이의 응집을 방지하고 준-단층 형태로 도입 할 수 있었다. 전 파장 영역의 빛을 흡수 할 수 있는 은 나노판을 기반으로 제작한 플라즈모닉 염료감응 태양전지는 최적화 조건에서 8.9±0.3% 에서 11.0±0.4% 로 효율이 상당히 향상 되었으며, 특히 광전류의 향상이 두드러졌다. 광전류의 향상 원인으로 빛 흡수의 향상과 전자 전달 효율의 향상이 있을 수 있다. 준 단층 형태의 은 나노판이 강하게 빛을 산란시키면, 그로 인해 유발된 국부적 표면 플라즈몬 공명에 의해 은 나노판의 표면이나 표면 근처에 존재하던 염료 N719 분자가 빛을 보다 많이 흡수할 수 있게 된다. 실제 연구 결과에서도 증가된 염료의 빛 흡수로 인하여 광전극층의 두께를 기존 두께의 절반인 4.5 μm로 줄일 수 있었다. 또한 광전극층에서의 전자 전달 효율의 향상은 감소된 전자 전달 길이를 통해서 간접적으로 증명 할 수 있었다.

염료감응 태양전지의 효율 향상을 위한 두 번째 방법으로, 플루오린이 도핑된 산화주석 유리기판(FTO)위에 금 나노입자와 그래핀을 이용하여 염료감응 태양전지의 상대전극을 개발하였다. 그래핀은 열 플라즈마 시스템을 이용하여 제조하였으며, 얇고, 순수하며 높은 결정성을 지니고 있었다. 그래핀의 크기는 100nm 이상이였으며, 음파처리를 이용하여 용매에 잘 분산 시킬 수 있었다. 상대적으로 큰 크기와 높은 결정성을 지니는 그래핀은 우수한 전도성과 분산력을 가지고 있어 상당히 균일한 필름을 제조하는데 적합하였다. 금 나노입자와 그래핀을 이용하여 개발한 상대전극으로 염료감응 태양전지를 제작하였을 때 최적화 조건에서 약 9.71%의 효율을 보였으며, 이는 그래핀 상대전극 및 기존의 백금 상대전극을 이용하여 제작한 염료감응 태양전지의 효율과 비교하여 다소 향상된 수치였다. 금 나노입자와 그래핀을 이용하여 개발한 상대전극은 금 나노입자의 국부적 표면 플라즈몬 효과를 기대 할 수 있었으며, 그래핀의 우수한 촉매 활성도로 인하여 상대전극과 전해질의 계면에서 발생하는 전하 이동 저항을 줄일 수 있었다. 이러한 현상은 입사 광전변환효율, 순환전압전류, 그리고 전기화학적 임피던스 측정을 통하여 증명 할 수 있었다.

중심어 : 염료감응 태양전지, 국부적 표면 플라즈몬 공명, 은 나노입자, 금 나노입자, 그래핀 상대전극